# Model-free analysis of quadruply imaged gravitationally lensed systems.

A DISSERTATION

SUBMITTED TO THE FACULTY OF THE GRADUATE SCHOOL

OF THE UNIVERSITY OF MINNESOTA

BY

Addishiwot Girma Woldesenbet

IN PARTIAL FULFILLMENT OF THE REQUIREMENTS

FOR THE DEGREE OF

Doctor of Philosophy

Prof. Liliya Williams

April, 2015

# Acknowledgements

This has been a long journey and it is the support and love of many that made it possible. I would like to use this opportunity to express my gratitude for those who helped me achieve my goal in graduate school.

Prof. Yuichi Kubota, thank you very much for giving me the opportunity to join the department; It all started with you. And I thank you and your wife Susan Armington for always having my back in happiness and sadness.

My defense committee members: Prof. Vuk Mandic, Prof. Lawrence Rudnick, Prof. Yong-Zhong Qian, and Prof. Liliya Williams I am very grateful to you all for taking the time out of your busy schedule to be part of this and for your invaluable feedback. Prof. Qian, I will pursue the idea you shared with me on how to further my research. Prof. Rudnick thank you for reviewing my thesis and your constructive input. I also appreciate the initiative you took to discuss my future plan in addition to providing me with information about available resources. Special thanks to Prof. Mandic for going above and beyond in reviewing every word of my thesis. I was in awe to see your detailed feedback and I hope to pay it forward.

For my mentor Prof. Liliya Williams, none of these would have been possible without your patience with me. Your dedication to me as your student was astounding. You treated me as a mentee when I needed guidance and brainstorming, and you shared the workload of our research as if I was your colleague. And never once have you said that you don't have time for me. Thank you very much for your guidance, understanding, friendliness, always having your door open, and repeatedly proofreading my thesis. I hope that as I move forward and build my career I become as professional and supportive for others as you are.

My dearest family and friends, words always fail me to expresses the profound impact you have in who I am. I will just say that I am blessed!

# Dedication

**Abuliyae, this and every good thing to come is for you.**

## Abstract

Gravitational lensing has proven to be a very valuable tool as a probe to better understand our universe. Parametric modeling of one multiple image gravitational lens system at a time is a common practice in the field of lensing. Instead of individual lens modeling, an alternative approach is to use symmetries in different spaces to make conclusions about families of lenses. The latter method is the focus of this thesis. Three types of lenses are defined based on whether they do or do not obey two-fold and double mirror symmetries. The analysis concentrates on quadruply imaged systems, or quads, and uses only the relative polar angles of quads around the center of the lens. The analysis is statistical in nature, and model-free because its conclusions relate to whole classes of models, instead of specific models.

The work done here is twofold. Firstly, exploratory analysis is done to check for possible existence of degeneracies. Type I lenses which obey both symmetries mentioned above are found to form a nearly invariant surface in the 3D space of relative image angles. In the same space, lenses that break the double mirror symmetry, grouped as Type II, form two distinct surfaces. In addition, degeneracy in this class of lenses is discovered. A preliminary study of the last group of lenses, Type III, that break both symmetries, is done.

Secondly, quad distributions in the 3D space from each of the three families were compared to observed galaxy-lens quads. Three quarters of observed

quads were inconsistent with the distribution of quads of Type I lenses. Type II lenses reproduce most individual lens systems but fail to reproduce the population properties of observed quads. Preliminary exploration of Type III lenses shows a very promising agreement with observations. Examples of Type IIIs are lenses with substructure (with clump masses larger than those responsible for flux ratio anomalies in quads), and lenses with luminous or dark nearby perturber galaxies, or line of sight structures.

# Contents

# List of Tables

# List of Figures

# Chapter 1

# Introduction

Even though we do not yet know the particle nature of dark matter, its existence, as required by the current model of the Universe, Lambda-CDM, is supported by a wide range of observational evidence. Of the different approaches used to better understand dark matter through the study of its spatial distribution, gravitational lensing (GL) plays an important role. Mass modeling of galaxies and clusters of galaxies using the images of lensed background sources is one of the central practices of GL. This thesis concentrates on obtaining useful information about the lensing objects without mass modeling, so it is complimentary to the standard techniques.

Chapter 2 provides a summary of the concordance model of the universe, The Standard Model of Cosmology (SMC). For how complex the universe is, currently, it is very successfully described using few parameters. These parameters are discussed here. In addition implications of, evidence for and shortcoming of SMC are also discussed. The theoretical formulation and the observational

successes of Gravitational Lensing (GL) is also part of this chapter. Finally, summary of evidence for the existence of Dark Matter (DM) and the commonly studied candidates are presented.

Chapter 3, published in MNRAS Woldesenbet and Williams [2] , is an extension of a previous work by Williams et al. (2008, ApJ 685, 725) which uses 'quads', four-image lens configurations. A novel approach analyzes, in a statistical way, the polar angular distribution of images around the galaxy lens center. Three groups of lens families are defined. For Type I, lenses whose caustics obey double mirror and two fold symmetries, lensing potentials with varied radial density profiles are explored. It is shown that quads from all sources lensed by galaxy potentials with twofold symmetries (symmetric about two orthogonal axes) lie on a near-invariant surface in the 3D space of the relative image angles. Finally, the discrepancy in the population property of quads of Type I lenses and observed ones is discussed.

Chapter 4, submitted to MNRAS for publication, first redefines the symmetry used to group lenses. Then, it widens the range of galaxy models considered above by breaking some of the symmetries. For example, Type II lenses have only two fold symmetry. Again different radial density profiles are explored so that model free conclusions can be made. Furthermore, preliminary work of Type III lenses, all other lenses, is presented. The model-free statistical analysis of quad samples in the 3D space of relative image angles can differentiate between smooth mass models often used in standard analysis, and clumpy, or substructured models.

For Each Chapter 3 and Chapter 4 individual summaries and conclusions are provided.

Chapter 5 briefly summarizes the thesis and provides future research directions.

# Chapter 2

# Background

## 2.1 The Standard Model of Cosmology (SMC)

The standard model of cosmology (henceforth SMC), also referred as ΛCDM model for reasons discussed later and informally as the Big Band theory, is considered as the concordance model describing the origin and evolution of our Universe. In a nutshell, at its current state, SMC states that our universe started from singularity, went through a brief (for $\sim 10^{-34}$s) but extreme expansion, and slowed down but has been expanding ever since.

It has been less than a century since cosmology has developed into an active field of study, and only in the last few decades has it grown due to increasing precision of large scale observations. In his seminal work [3], Edwin Hubble combined his measurements of the distance of galaxies with their speed from previous measurement by Vesto Slipher [4] to show that the Universe is expanding. This discovery planted the seed for our current understanding of the Universe.

### 2.1.1 Parameterizing the Universe

When studying complex systems, for the most part, physicists do no attempt to describe the behavior of each and every element that makes up the system. Rather, we make reasonable and intuitive assumptions and define macroscopic quantities that describe the system as a whole and investigate the relationship between these quantities. This is called parametric modeling. Since the universe is as complex ( in terms of quantity of its constituents ) as it gets, we do the same and parametrize it.

When parameterizing the Universe the intuitive assumption made was what is commonly known as Cosmological Principles (CP). CP states that the Universe is homogeneous (at large scale one sees the same thing from every point in the universe ) and isotropic ( the universe looks the same in every direction). These principles were mere assumptions before recent observational evidence such as the uniformity of the temperature of the relic radiation confirming them (Figure 2.1).

#### Newtonian Cosmology

An observer at any point in space that sees the universe as isotropic is called a fundamental observer. If we have two such observers separated by $a(t)$ looking at an event E at a given time t, then Newtonian kinematics and dynamics can be used to model a universe that satisfy the CP. Using the relative position of the two observers and imposing CP so that the two observers have the same picture of the universe, one can show that [5]

$$\mathbf{v}(\mathbf{r} - \mathbf{r_1}) = \mathbf{v}(\mathbf{r}) - \mathbf{v}(\mathbf{r_1}) \tag{2.1}$$

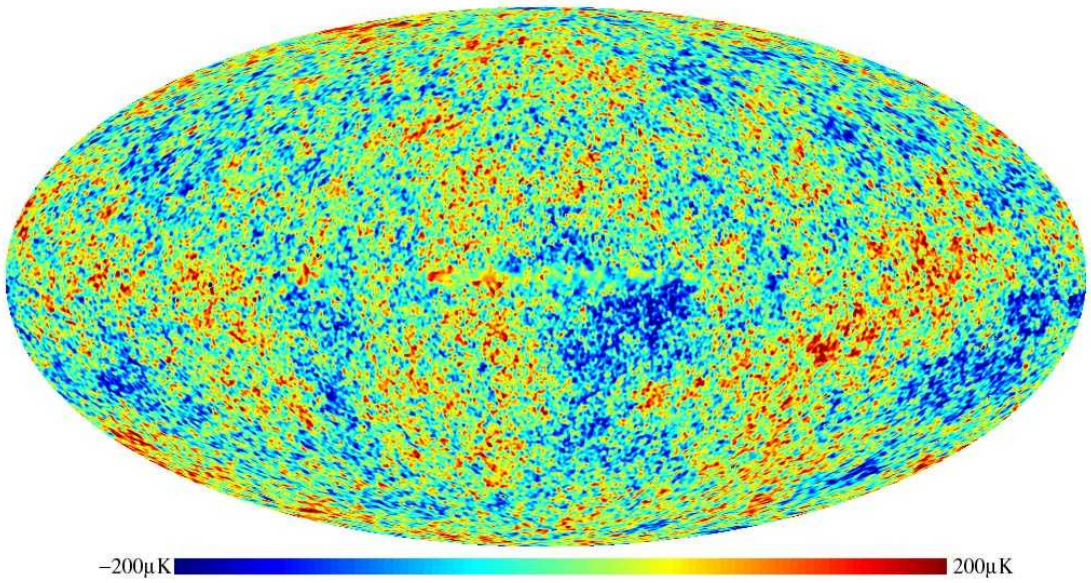


Figure 2.1: WMAP source: WMAP Science Team / NASA.

where $v$ is the velocity, $\mathbf{r}$ is the position of the event from, say, the first observer, and $\mathbf{r_1}$ is the position of the second observer relative to the first. This equation shows that the velocity is a linear function of r and for isotropic universe, it has a general solution of

$$\mathbf{v} = H(t)\mathbf{r} \tag{2.2}$$

This is the Hubble relation of an expanding universe. Therefore, Newtonian kinematics is enough to show that a homogeneous and isotropic universe implies an expanding or contracting universe. Integrating Equation 2.2 above would give

$$H(t) = \frac{\dot{a}}{a} \qquad \text{where } \mathbf{r} = \frac{a(t)}{a_o}\mathbf{r_o}, \quad a_o = \mathbf{a}(t_o) \tag{2.3}$$

Since a(t) scales distance it is called a scale factor. Now to study the dynamical

state, we assume the universe is filled with pressure-less matter. Notice that this assumption doesn't apply for any other state such as radiation dominated universe. The continuity equation of fluid dynamics would then imply,

$$\rho \propto a(t)^{-3} \tag{2.4}$$

If we now assume the Universe as a sphere of uniform matter density, a thin shell at radius r would experience force only from the matter within the shell. This relation can not be extended for a shell at infinity within Newtonian dynamics, but using general relativity it can be shown that such an extension is valid ( Birkhoff's theorem). By recalling the form of gravitational acceleration, Newton's second law of motion can be written as

$$m\ddot{\mathbf{r}} = -\frac{4\pi G m \rho}{3}\mathbf{r} \tag{2.5}$$

Using Equations 2.4 and 2.3, solving for the velocity of the scale factor yields,

$$\dot{a}^2 = \frac{8\pi G \rho_o}{3a} a_o^3 - kc^2, \tag{2.6}$$

where $\rho_o$ is the density at time $t_o$ and k is a constant parameter. Positive k implies a universe with finite kinetic energy in the limit of a(t) approaching infinity, while a zero k results in a universe that comes to rest for such limit of a(t). A negative k represents a universe that never stops expanding [6].

**General Relativistic Cosmology**

Newtonian theory of motion breaks down when studying light and particles moving near the speed of light. Newton's relativistic motion equation implies the speed of light is dependent on its source but this was experimentally shown not to be the case by Michelson and Morley [7]. Their experiment led to the formulation of special relativity by Albert Einstein in 1905. The theory of relativity is founded on a special consideration of the space-time different from Newton's. Instead of treating time and space as two separate coordinates, Einstein defined an event to be identified by four coordinates, the usual three spatial coordinates along with a new time coordinate. A line element is then defined as an invariant "distance" in space-time given as,

$$ds^2 = dt^2 - \frac{1}{c^2}\mathbf{dr}^2, \qquad \text{where } \mathbf{dr} \text{ is a 3D spatial coordinate.} \tag{2.7}$$

This equation applies when the different observers are moving at a constant speed relative to each other. If an object is accelerating with respect to an inertial frame then its path deviates from a free motion according to Newton's second Law. Therefore, one can infer about the existence of external forces, inertial forces, by studying the trajectory of objects. But there is ambiguity with gravitational force since all objects accelerate at the same rate under its influence. Einstein thought experiment is a simple example to understand that gravitational force becomes a non-inertial force, ie. there is a preferred coordinate system where it can vanish. A person confined in a small closed space can not study the trajectories of objects to decide the presence of gravitational field. The path of an accelerating object in

zero gravitational field is indistinguishable from that of an object accelerating at the same rate due to an external gravitational field. These two indistinguishable scenarios makes up what we call the *equivalence principle*. Therefore, in a situation where the gravitational field is uniform, local frame, Equation 2.7 still holds. In non-local frame, we should incorporate the spatial variation of gravitational field by defining a more general line element with each differential term of the right hand side of Equation 2.7 to have coefficient dependent on both time and spatial position. This is what we call *General Relativity*.

For a homogeneous and isotropic universe the most generic line element is given by what is commonly known as the Friedmann-Rebertson-Walker (FRW) metric,

$$\mathrm{d}s^2 = c^2\mathrm{d}t^2 - a^2(t)\left(\frac{\mathrm{d}r^2}{1-kr^2} + r^2\mathrm{d}\theta^2 + r^2\sin^2\theta\mathrm{d}\phi^2\right) \tag{2.8}$$

where $a(t)$ is a scale factor, $k$ is the curvature constant with possible values $+1$, 0, $-1$ for spatially positive (closed), flat, or negative (hyperbolic or open) universe, respectively. $g_{\mu\nu}$ is the metric formed from the the coefficients of the $\mu$ and $\nu$ elements which are t, r, $\theta$, and $\phi$.

To solve for the scale factor a(t) as in Equation 2.6, we need to solve the general relativistic field equation which is the equivalent of solving Poisson equation for a non-relativistic motion. The external driving force comes from matter and radiation in the form of the energy momentum tensor given by

$$T_{\mu\nu} = (P+\rho)u_\mu v_\nu - \rho g_{\mu\nu} \tag{2.9}$$

and Einstein's general relativity equation of motion is given

$$R_{\mu\nu} - \frac{1}{2}g_{\mu\nu}R = 8\pi G T_{\mu\nu} + \Lambda g_{\mu\nu}, \tag{2.10}$$

where $\Lambda$ is called the Cosmological constant.

For the CP abiding FRW metric (2.8) the tt component of the solution for the above equation takes the form

$$\left(\frac{\dot{a}}{a}\right)^2 + c^2\frac{k}{a^2} = \frac{8\pi G}{3}\rho_{total}, \tag{2.11}$$

where $\rho_{total} = \rho_m + \rho_{rad} + \rho_{vac}$ and $\rho_m$, $\rho_{rad}$, $\rho_{vac}$ are the energy density of matter, radiation and vacuum respectively. The other components of the Einstein equation (2.10) give the solution

$$\frac{2\ddot{a}}{a} + \left(\frac{\dot{a}}{a}\right)^2 + c^2\frac{k}{a^2} = -8\pi G P, \tag{2.12}$$

where $P$ is the pressure of the universe.

These equations along with conservation of energy and momentum $T^{\mu\nu}_{;\mu} = 0$ reduces to the form

$$\dot{\rho} + 3H(P + \rho) = 0 \tag{2.13}$$

where the **Hubble parameter** H is defined to be $\frac{\dot{a}}{a}$. Furthermore, combining the two equations (2.11) and (2.12) yields,

$$\frac{\ddot{a}}{a} = -\frac{4\pi G}{3}(\rho + 3P). \tag{2.14}$$

Equations 2.13 and 2.14 are the two reduced form of general relativistic field equations for FRW cosmology.

In order to solve for the scale factor a(t) as a function of time and to see how the energy density $\rho$ scales with a(t) we can use the equation of state that relates energy density $\rho$ and pressure $P$ which is given as

$$P = \alpha\rho \tag{2.15}$$

where $\alpha = 0, 1/3, -1$ for non-relativistic matter, radiation, and cosmological constant $\Lambda$ respectively. Using (2.15) and one of the cosmological equation (2.13) we get,

$$\rho \sim \begin{cases} a^{-4} & \text{radiation dominated era;} \\ a^{-3} & \text{matter dominated era;} \\ \text{constant} & \text{vacuum energy dominated era.} \end{cases} \tag{2.16}$$

And using (2.15) in the second cosmological equation (2.14) we get,

$$a(t) \sim \begin{cases} t^{\frac{1}{2}} & \text{for radiation dominated era;} \\ t^{\frac{2}{3}} & \text{for matter dominated era;} \\ \mathrm{e}^{Ht} & \text{for vacuum dominated era.} \end{cases} \tag{2.17}$$

Using the Hubble parameter, equation (2.11) can be rewritten as

$$\frac{c^2 k}{H^2 a^2} + 1 = \frac{\rho_{total}}{\left(\frac{3H^2}{8\pi G}\right)}. \tag{2.18}$$

Notice that this equation, for $\rho_{total}$ entirely made out of non-relativistic matter, is exactly what we obtained using Newtonian dynamics in Equation 2.6. But unlike the Newtonian cosmology, general relativistic cosmology is applicable to any form of energy density hence it can describe the early hot radiation dominated era of our universe. In addition, we needed the help of general relativistic implication in the form of Birkhoff's theorem to complete our derivation of Newtonian cosmology. And k here is a geometric parameter describing the spatial curvature.

If we define a critical density at any given time t as $\rho_c \equiv \frac{3H^2}{8\pi G}$, then we can express the energy density of the universe (matter, radiation or vacuum energy)

as a dimensionless parameter which describes the energy density as a fraction of $\rho_c$

$$\Omega_i = \frac{\rho_i}{\rho_c} \tag{2.19}$$

This is called the **density parameter**. In terms of the critical density $\rho_c$, if we look back to (2.19) we see that a negative $k$ (open universe) means the total energy density is less than the critical and vice versa with a spatially flat universe, i.e $k = 0$, resulting from the total energy density being equal to the critical density.

Another commonly used parameter known as the **deceleration parameter** is defined as

$$q_o \equiv -\frac{\ddot{a}}{aH_o^2}, \tag{2.20}$$

where the subscript "o" is used to denote that the parameter refers to that of the present epoch. Using (2.14) $q_0$ can be expressed in terms of $\Omega_{0i}$ as

$$q_0 = \sum_i \frac{\Omega_{0i}}{2}\left(1 + \frac{3P_i}{\rho_i}\right) = \frac{1}{2}\sum_i \Omega_{0i}\left(1 - \alpha_i\right). \tag{2.21}$$

### 2.1.2 Implications and observational evidence for SMC

In the previous section, we came up with very few parameters, the **Hubble parameter**, the **the density parameter** , and the **deceleration parameter**, to describe the states of our vast universe at any given time t. In the process we have touched on some of the implications of the SMC and in this section we will summarize some of the most prominent observable quantities.

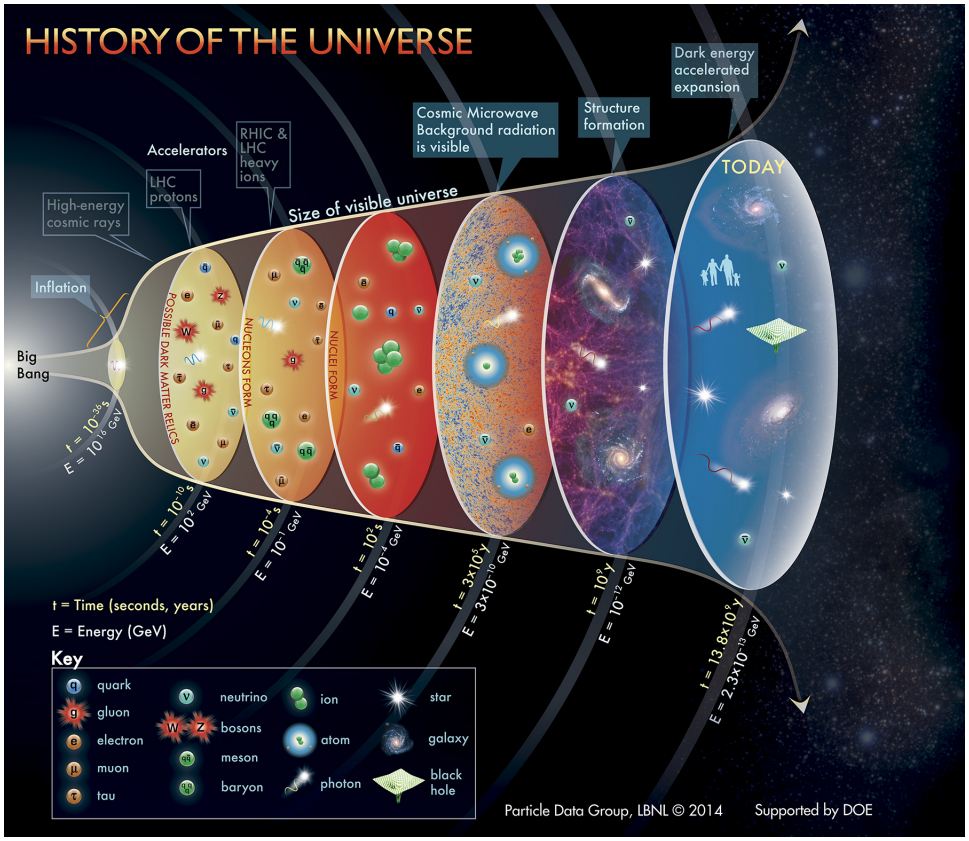


Figure 2.2: A schematics of the history of the Universe. Source: Particle Data Group at Lawrence Berkeley National Lab.

### Cosmological redshift and the expanding universe

The FRW metric in 2.8 for light traveling freely in space-time reduces to the form,

$$\frac{c\,\mathrm{d}t}{a(t)} = -\frac{\mathrm{d}r}{\sqrt{1-kr^2}} \tag{2.22}$$

If we integrate the above equation and study what happens to successive light wave crests (small time intervals) emanating from a distant source (labeled by 1)

as observed in our current position (labeled by o) , we get the following relation

$$\frac{\lambda_o}{\lambda_1} = \frac{a(t_o)}{a(t_1)}, \qquad \text{where}\lambda \text{ is the wavelength } c\ \Delta(t) \tag{2.23}$$

The ratio $\frac{\lambda_o}{\lambda_1}$ is related to the redshift as $1 + z$ which describes the fraction of change in the wavelength of light as it propagates in space and time. In addition, the observation by Hubble shows that the observed wavelength from distant galaxies are longer (red-shifted) than what is typically emitted by galaxies implying $a(t_o) > a(t_1)$, i.e an expanding universe. The rate of expansion given by the Hubble parameter is currently constrained to be $73.8 \pm 2.4$ km s$^{-1}$Mpc$^{-1}$ [8]

**Horizons**

At any given epoch, the particles we can observe in the universe is limited. Therefore, there is a maximum distance an observer can see and the "horizon" which divides the particles that can be seen from those which can't is called a particle Horizon. The existence of such horizon can be obtained by integrating eqn. 2.22 from a source to an observer and finding the maximum proper distance. And there is a finite solution to this maximum distance dependent on the curvature parameter k and the deceleration parameter $q_o$. This implies that the observable universe is finite and as time goes on we see more and more of it.

**Space-time singularity**

Probably one of the most dramatic predictions of the SMC is the origin of the Universe being a space time singularity. If we look at Equation 2.17, we see that

tracing back the evolution of the universe leads to a spatial singularity. Theoretically speaking this prediction doesn't sit well with the need for continuity and differentiability of the field equation.

### ΛCDM cosmology and the CMB

Starting from the current state of the universe we can extrapolate backwards to study its state at different epochs. Equation 2.16 shows that in its earlier stages our universe was radiation dominated and smaller in size hence at very high temperature. Therefore, unlike what we see now, the universe was a hot soup where every element is ionized and coupled together in thermal equilibrium which means the radiation has a Planck blackbody spectrum. Due to expansion the universe cools down and radiation is separated from matter with the blackbody radiation spectrum at lower temperature. This background relic radiation, known as Cosmic Microwave Background (CMB), was first accidentally discovered by Penzias and Wilson [9]. Since then the black body radiation spectrum has been measured with high level of precision [10].

Using the present value the Hubble parameter, we can calculate the energy density contribution of the relic radiation, CMB, as predicted by SMC with its present temperature value of $T = 2.73°\text{K}$. The result is

$$\Omega_{0\gamma} = \frac{\rho_\gamma}{\rho_c} = \frac{(\pi^2/15)T_0^4}{3H_0^2/8\pi G} \approx 7.89 \times 10^{-5},$$

which is negligible. And as discussed later in Section 2.3, most of the matter is in the form of a collisionless and non-relativistic matter which is commonly

referred to as Cold Dark Matter (CDM). Therefore, SMC is also called ΛCDM model. Hence considering the present universe to be dominated only by matter and vacuum energy $q_0$ from Equation 2.21 reduces to,

$$q_0 = \Omega_{0\Lambda} + \frac{\Omega_{0M}}{2}.$$

This relation along with Equation 2.20 imply that since the expansion of the universe is accelerated when $q_0 < 0$ a negative value of $\Omega_{0\Lambda}$ is possible. Such scenario imply that $\Lambda$ can act as a driving force of expansion.

**The Big Bang Nucleosynthesis (BBN)**

As the temperature of the Universe cools down and dips below what is required to break the binding interaction of different ions, more stable and heavy elements are produced. The process by which a new atomic nucleon is formed from existing nucleons is called Nucleosynthesis. Thermodynamics as applied to the SMC predicts the relative abundances of light elements and we call this process the Big Bang Nucleosynthesis (BBN), which happened a couple of minutes after the big bang. The prediction of BBN for the abundance of Deuterium (D) or heavy H atom in an excellent agreement with the prediction from quasar absorption systems [11]. In addition, there is a great agreement between BBN and WMAP (which is the blue print of photon at decoupling around 380000 years after the big bang) in the abundance of He and D. But there is a discrepancy in their prediction of the abundance of Li.

**Gravitational lensing**

One of the consequence of general relativity is the precise prediction of the bending of light by mass. Since light is a relativistic particle, its motion through space in the presence of mass can be mapped by solving for its trajectory by setting $ds^2$ to zero for the appropriate metric through which the light is traveling. Such bending of light does not require the SMC or the fulfillment of the cosmological principles. It is more of a direct outcome of GR. But since SMC in its fullest form is a general relativistic model, bending of light can naturally be described by the former.

The first observation evidence of the bending of light from a straight line path achieved by Dyson et al. [12] in 1919 during the eclipse of the sun. The are other very interesting consequences of the gravitational lensing and to name a few: time delay in radar signals as reflected from planets, distorted images of distant objects, multiple images of a background as lensed by a foreground mass, magnification and demagnification of background objects, etc. We shall delve into the theoretical framework of GL in more detail in Section 2.2

### 2.1.3 Shortcomings of SMC

The main shortcomings of the SMC is in small scales. The number of low-mass galaxies discovered by Sloan Digital Sky Survey is lower than predicted by SMC. The amount of substructure in galaxies as predicted by Numerical Simulations are also not in full agreement with those observed through milli-lensing. As mentioned above, there is also some inconsistency between the BBN prediction of Li

abundance and that from WMAP. One more commonly mentioned challenge is the interpretation of the singularity of the Universe as it came to existence.

Despite these and other challenges the SMC is the most self consistent and observationally tested model of our universe.

## 2.2 Gravitational Lensing (GL)

Figure 2.3: *Left:* The castle on the Mall in Washington, DC. *right:* The castle after being lensed by a black hole with a mass of Saturn placed in the middle of the mall. Source:https://www.cfa.harvard.edu/ bmcleod/castle.html

### 2.2.1 History and Implications of GL

The term Gravitaional Lensing (GL) refers to the bending of light by mass acting like a lens. Sir Issac Newton is credited for the first attempt made to understand some behaviors of light such as reflection and refraction by modeling it as a stream of particles. In his book *Opticks* he explored these properties of light and he also posed the question what the interaction of light with mass would be

without addressing it much further. The first published calculation of the angle of deflection of light ray from a straight path coming from infinity as it goes by the Sun was made by Soldner J. (1804) using Newton's law of kinematics. For light rays grazing over the sun's surface this deflection angle was calculated to be 0.84 arcseconds. This result given below was reproduced by Albert Einstein using time dilation of special relativity.

$$\alpha = \frac{2GM_{\odot}}{c^2 R_{\odot}} \tag{2.24}$$

After the invention of general Relativity (GR) by Einstein, he recalculated this deflection putting the effect of space-time curvature on the path of light. This new calculation, [13], showed that the deflection angle at a closest approach distance R from a point mass M is a factor of two more than the above value.

$$\alpha = \frac{4GM}{c^2 R} \tag{2.25}$$

A solar eclipse expedition by Dyson et al. [12] provided the first observational evidence in support of lensing as calculated by GR by measuring the angle of deflection within 30%. Deflection angles of light path as predicted by GR are now measured within 1% [14]. Theoretical implications of the bending of light were further investigated as discussed below, but it was not until 1979 another successful direct observation of Lensing was made [15]. Now there are databases of observed gravitational lenses such as CASTLES Survey [16].

So what does bending of light by mass imply? If light from a background source is gravitationally lensed by a foreground mass on its way to an observer,

then there are multiple paths that it can take. Existence of different paths taken by light means formation of multiple images of the background source as seen by an observer as long as appropriate conditions are satisfied as discussed later.

One path could be longer than the other as light travels in space-time implying there is delay in the arrival time between the two images.The lens system can be modeled as the lensing mass perturbing the standard FRW metric. Using such metric and calculating the time it takes light on each path yields two terms; one a geometric time delay while the other is due to the perturbing lensing potential [17].

If we study lensing of a circular object, we can see that the image formed is distorted. Such distortion is a result of the light from different parts of source being bent at different angle since the deflection angles are functions of the closest distance of approach to the lens. One consequence of this image distortion is the difference between relative magnification of images of a given source. Magnification is defined as ratio of the flux of an image to that of the source. The solid angles of two images of the same source are in general different. But since the surface brightness (luminosity) of the source and both images are the same, the relative flux between the two images is different due to the difference is the solid angles.

The mathematical derivations of these qualitative implications of lensing discussed above are briefly shown in the next sections.

### 2.2.2 Lens Mapping

With the assumption that our universe is well described by the Standard Model of Cosmology, the FRW metric can be used to describe its geometry. The gravitational potential of lenses can then be incorporated to the metric as local perturbation. The typical source-to-lens and lens-to-observer distances is about three orders of magnitude larger than the thickness of a typical cluster lens [18] . Therefore we take the projected mass of lenses on a plane (the lens plane). This is called thin lens approximation. In addition, the Newtonian gravitational field of lenses even as big as clusters of galaxies, are about four orders of magnitude less than $c^2$ and the motion of their constituent is non-relativistic. These conditions reduce the perturbed FRW metric near the lens to be simply a flat space metric perturbed by Newtonian gravitational fields of the lens. Then, the deflection angle at closest approach distance r is a linear function of the deflector mass as given in Equation 2.25. To find the total deflection we add up (integrate) the contributions from infinitesimally small masses on the lens plane which each act like a point mass. Therefore, for a lens with a surface mass density, $\Sigma(\boldsymbol{\xi})$, the total deflection angle $\hat{\boldsymbol{\alpha}}(\boldsymbol{\xi})$ is given by the following integration over the entire extent of the lens,

$$\hat{\boldsymbol{\alpha}}(\boldsymbol{\xi}) = \frac{4\pi G}{c^2} \int d^2\xi' \; \Sigma(\boldsymbol{\xi'}) \; \frac{\boldsymbol{\xi} - \boldsymbol{\xi'}}{|\boldsymbol{\xi} - \boldsymbol{\xi'}|^2} \tag{2.26}$$

Figure 2.4, shows a ray tracing of light from a source passing by a lens on its way to an observer. Using the variables defined in the figure, geometrically, angles $\boldsymbol{\theta}$, $\boldsymbol{\beta}$, and $\boldsymbol{\alpha}(\boldsymbol{\theta})$, where the reduced angular deflection $\boldsymbol{\alpha}(\boldsymbol{\theta}) = \frac{D_{ds}}{D_s} \; \hat{\boldsymbol{\alpha}}(\boldsymbol{\theta})$, are related by :

$$\boldsymbol{\beta} = \boldsymbol{\theta} - \boldsymbol{\alpha}(\boldsymbol{\theta}) \tag{2.27}$$

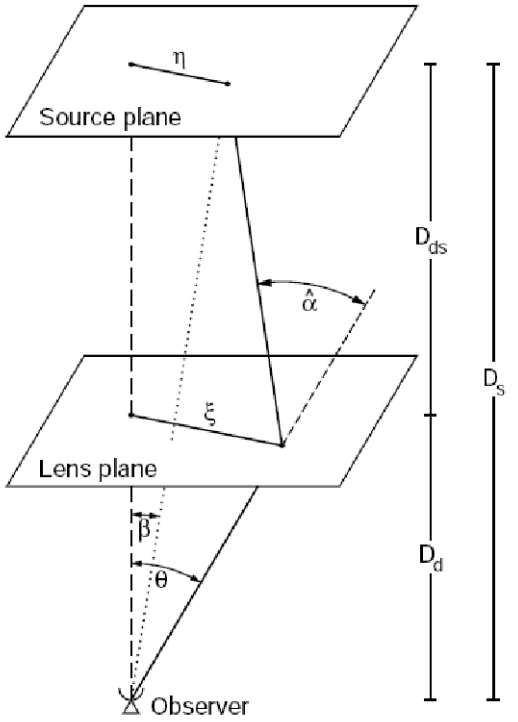


Figure 2.4: Schematics of gravitational lensing system. Source: Bartelman & Schneider 2001. $D_i$s are angular diameter distances. The subscript d refers to the deflector(lens)

Equation 2.27 is called lens equation. The lens equation maps the source plane to the lens plane. Notice that for a given source position $\beta$, the equation can yield **multiple solutions, i.e multiple image positions**.

The reduced angular deflection vector $\boldsymbol{\alpha}(\boldsymbol{\theta})$ can be written as a gradient of a scalar potential $\psi(\boldsymbol{\theta})$. Then the lens equation can be re-written as,

$$\boldsymbol{\nabla}\left(\frac{|\boldsymbol{\beta}-\boldsymbol{\theta}|^2}{2}-\psi(\boldsymbol{\theta})\right)=0 \tag{2.28}$$

The quantity inside the parenthesis is called Fermat potential $\phi$. And this form of

the lens equation is Fermat's principle of propagation of light in general relativity. Actually the light travel time is the Fermat potential scaled by a factor of $\frac{D_d D_s}{D_{ds}} \frac{(1+Z_d)}{c}$ where $Z_d$ is the redshift of the deflector [17]. Then using 2.28, we can see that for a multiple image lens system, the arrival time of each image is in general different. The relative arrival time between two images is called **time delay**. The two terms of this equation also clearly show the separate contribution of geometry (the first term) and potential (the second term) to the arrival time.

Light rays from very small but extended source are deflected differently by the lens. For infinitesimally small variation in the source position, there is a corresponding change over the body of the image as dictated by the lens equation. The resulting difference in solid angle of the infinitesimal regions of the source and image is then a function the ratio of the variations. Since the propagation of light through a medium conserves the photon number, the change in solid angle results in the change in flux which is written as,

$$\mu = |\det(\ \frac{\partial \boldsymbol{\beta}}{\partial \boldsymbol{\theta}}\ )|^{-1} \tag{2.29}$$

This expression for flux implies that there could be points on the source plane that are infinitely magnified since the determinant of the relative variation could be zero. This set of point on the source plane is called *caustic*. The corresponding set of points on the lens plane where the images are formed is called *critical curve*. As a source for a given lens system moves towards the caustic, the images formed move closer to the critical line in pair and become very bright. Once the source moves across a caustic the images that approach the critical line disappear.

Let's now solve the lens equation for a specific example; a lens with axially symmetric mass distribution. Writing Equation 2.26 in terms of the angular distances, the lens equation for such lens reduces to

$$\beta = \theta - \frac{4\pi G D_{ds} M(\theta)}{D_d D_s c^2 \theta} \tag{2.30}$$

where $M(\theta)$ is the total mass within the circle of angular diameter $\theta$. The solution for a source position $\beta = 0$ form a ring, known as Einstein ring ( fig. 2.5), in the lens plan given by

$$\theta_E = \sqrt{\frac{4\pi G \ M(\theta_E) \ D_{ds}}{D_d D_s c^2}} \tag{2.31}$$

The symmetry in the lens profile we considered makes solving the lens equation very trivial. In general, the angular deflection is a more complex function of $\theta$. The Einstein ring above is a function of the mass of the lens and the distances that characterizes the lens system, therefore it serves as a scale parameter.

In the example above where we find image position given circularly symmetric lens and known source position is called *forward lensing*. But in such cases we are not getting any new information out of it since the images are observable and everything else is given. The alternative method, called *inverse modeling*, where given the image position (based on observation) finding the mass profile of the lens is a very important probe to the mass content of the lens.

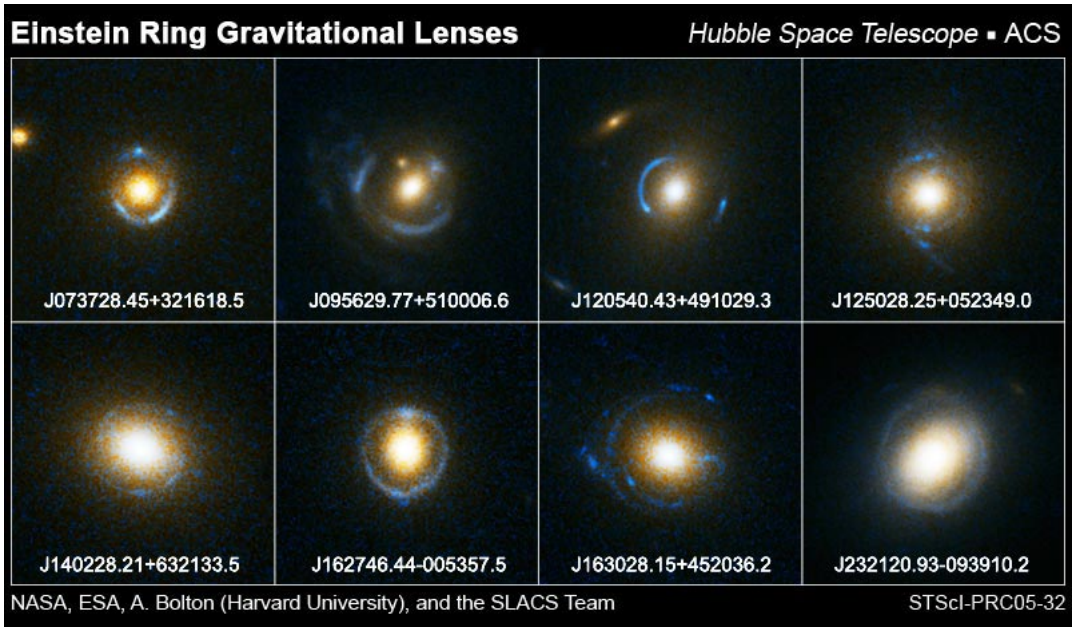


Figure 2.5: Observed lensed system with Einstein ring.

### 2.2.3 GL Phenomena: Strong, week, and micro lensing

#### STRONG LENSING

Starting from the lens equation 2.26 we can solve for the reduced deflection angle as,

$$\boldsymbol{\alpha}(\boldsymbol{\theta}) = \frac{1}{\pi} \int d^2\theta' \; \kappa(\boldsymbol{\theta'}) \; \frac{\boldsymbol{\theta} - \boldsymbol{\theta'}}{|\boldsymbol{\theta} - \boldsymbol{\theta'}|^2} \tag{2.32}$$

where $\kappa(\boldsymbol{\theta'}) = \frac{\Sigma}{\Sigma_{cr}}$ for $\Sigma_{cr} = \frac{c^2 D_s}{4\pi G \; D_d \; D_{ds}}$. $\Sigma_{cr}$ is called critical surface density and it characterizes the lens system. Now looking back at the lens equation (2.27), we can see that multiple image positions, that are visibly separated, are in general possible if the angular deflection is big enough. And in the above equation

if $\kappa(\boldsymbol{\theta'}) \ll 1$, i.e $\frac{\Sigma}{\Sigma_{cr}} \ll 1$, then it means the mass is not enough for the lens system to give rise to the appropriate amount of deflection that results in multiple images. When $\Sigma \sim \Sigma_{cr}$, for some angular position in the lens plane, magnified multiple images or even Einstein rings may result from the lens equation and we call this kind of GL **strong lensing**.

The first ever (1979) observed multiple image lens system, SBS 0957+561, was a twin image of a quasar at z = 1.41 [15]. Lensing of galaxies by clusters, Figure 2.6, gives a deeper view of our universe and provides better probability of multiple image lensing event than galaxy-by-galaxy or quasar-by-galaxy. Figure 2.7 shows the first ever captured five star-like images of a distant quasar by galaxy cluster. The first four image system discoverd was PG1115. The central image of five images system lensed by galaxies is shadowed by the bright central part of the galaxies, such images are commonly called quads.

What makes strong lensing one of the most adept tools for probing the universe, due to multiple image formation and background magnification, can be summarized as follows:

- Analyzing the positions and distributions of multiple images on the lens plane, through inverse modeling or statistical analysis, can help infer the mass content of the lens.

- Measuring the time delay of multiple image lens system can be used to determine the geometry of the universe.

- Due to magnification, we can capture faint distant cosmic objects which are otherwise not visible.

- In addition, the enlarged solid angle due to strong lensing exposes more of the internal properties of distant objects.

Figure 2.6: Multiple images (extended, blue) of a distance galaxy lensed by a foreground cluster of elliptical and spiral galaxies (yellow). Credit: W.N. Colley and E. Turner (Princeton University), J.A. Tyson (Bell Labs, Lucent Technologies) and NASA

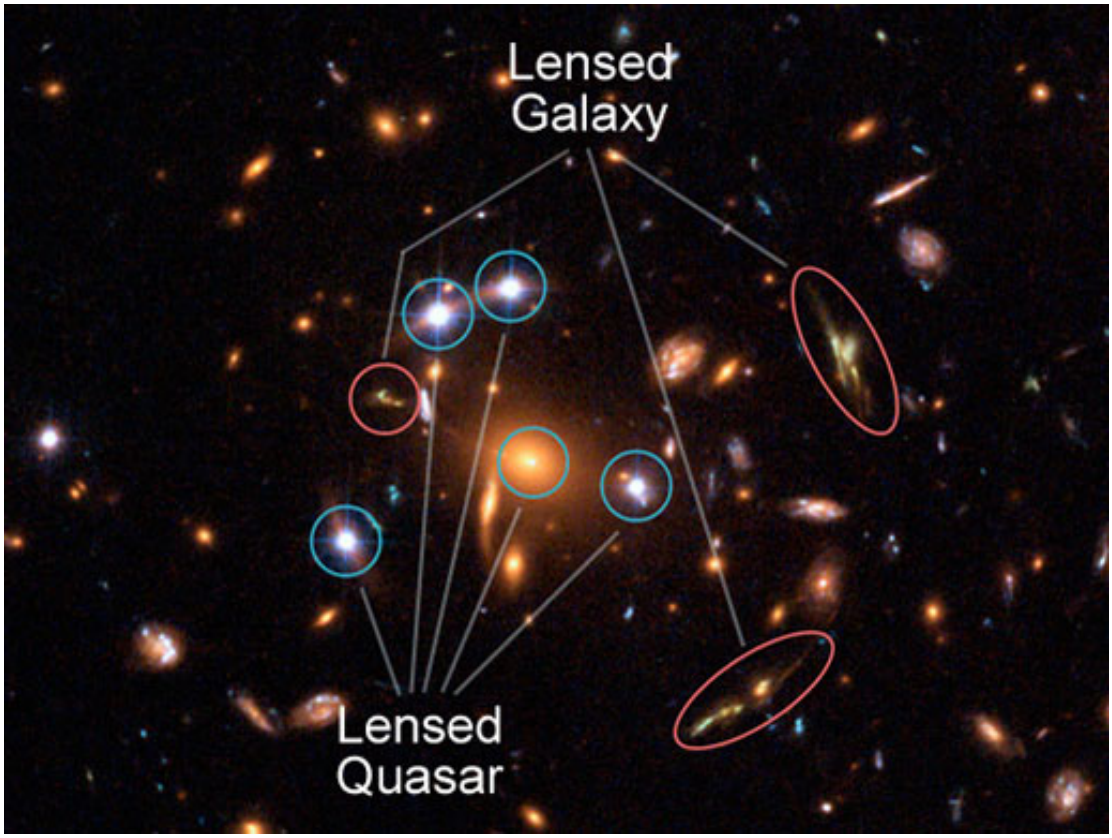


Figure 2.7: The first ever observed five images of a distant quasar lensed by SDSS J1004+4112 cluster. Credit: NASA, ESA, K. Sharon (Tel Aviv University) and E. Ofek (Caltech)

**WEAK LENSING**

For lenses with masses density less than critical density, multiple images are not formed. Rather the result of lensing of background sources in such a situation is just small distortion. By statistically analyzing the distortion of background galaxies, the mass distribution of the foreground object can be deduced. The intrinsic elongation of galaxies pauses a challenge to measure the actual distortion due to lensing. This is called the shape noise (Figure 2.8). To circumvent this

challenge, we should measure the distortion of many background galaxies and the mean distortion is taken to be arising from weak lensing. This is because the intrinsic distortion of background galaxies is random hence averaging to zero.

The first observed weak lensing signal was documented by Tyson et al. [19]. But the most profound observation that shows the power of weak lensing as a technique to probe the universe is that of the Bullet Cluster. The isodensity contour lines of the cluster's total mass as predicted by weak lensing, from systematic distortion of background galaxies, is given in Figure 2.9. The overlap of this figure with the the X-ray signal from hot gas is consistent with what is observed (fig 2.11 )

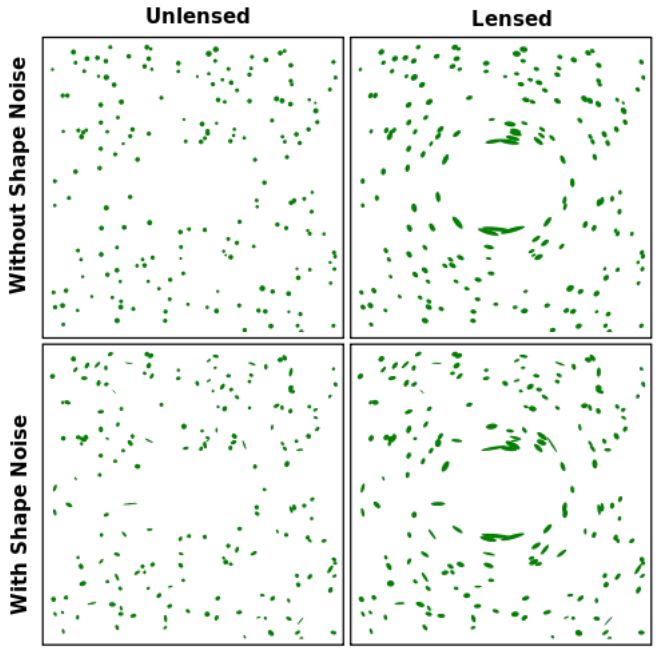


Figure 2.8: Schematics to show the distortion of background galaxies due to weak lensing. "Note that the distortion shown here is greatly exaggerated relative to real astronomical systems."
Credit: TallJimbo/WeakLensing

## MICRO LENSING

When the size of a lens is very small, a typical star for example, the Einstein radius is going to be too small too resolve any multiple images or distortion backgrounds. But when a small foreground object transverses between a background and an observer the background object will temporarily be magnified. This transient event is called micro lensing. One of the application of microlensing is in search of exoplanets. When an exoplanet orbits around its star, the momentary magnification of the star would imply the existence of such planets. Another similar application is searching for dark compact objects within galaxies by studying

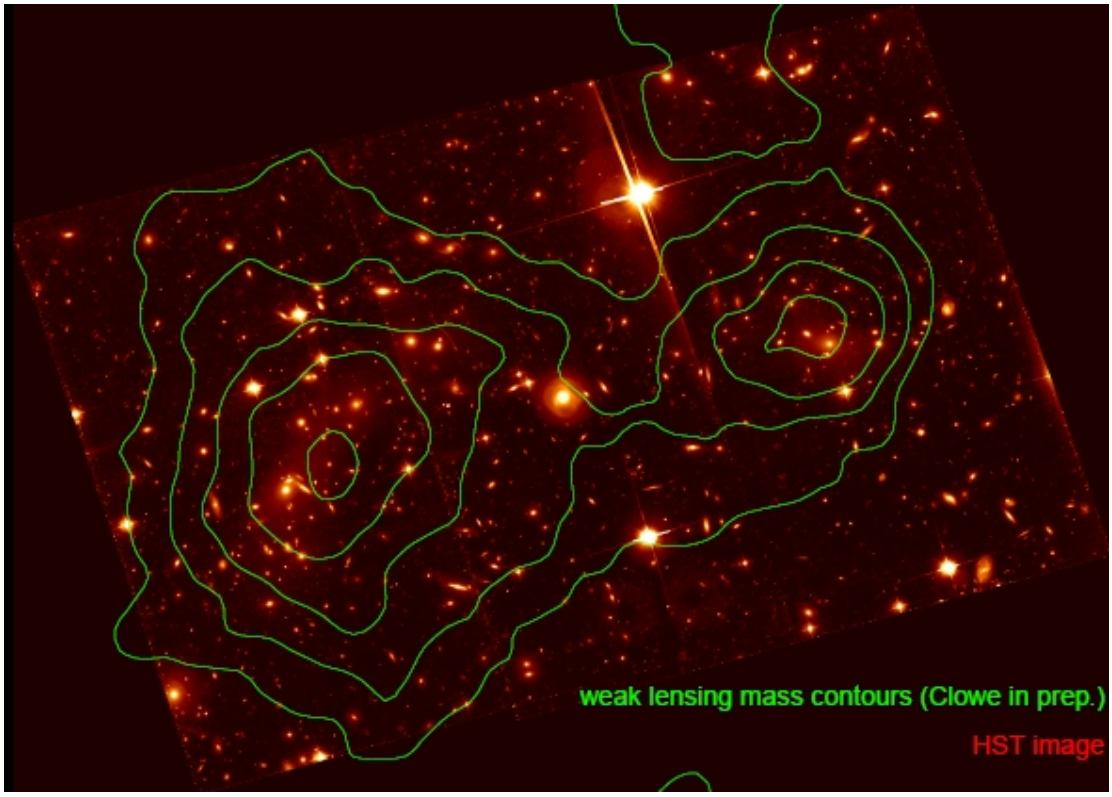


Figure 2.9: Isodens contour lines (green) due the total mass of the cluster as predicted by weak lensing.
Source: *http://cxc.harvard.edu/symposium_2005/proceedings/files/markevitch_maxim.pdf*

potential brightening of stars in the galaxy due to the relative motion between the two.

## 2.3 Dark Matter

Even though the exact particle nature of Dark Matter(DM) is yet to be determined, its existence is undoubtedly known. Since its first theoretical and observational inception a variety of observational methods such as studying the dynamics of galactic motion, X-ray emissions by elliptical galaxies and clusters of galaxies, the power spectrum of the cosmic radiation, and gravitational lensing provide strong evidence for the presence of DM in the universe. Below we explore some of these pieces of evidence [1].

### 2.3.1 Evidence for the existence of Dark Matter

***At the scale of cluster of galaxies:***

The study of both the dynamics of galactic motion in clusters and the mass deduced using the observations of X-rays from hot gas both imply the existence of matter beyond the visible amount. Much of the evidence for the existence of dark matter comes from the study of the motion of galaxies. Many cluster of galaxies appear to be fairly relaxed so by the virial theorem the total kinetic energy should be half the total gravitational bounding energy of galaxies. However, experimentally the total kinetic energy is found to be much greater, in particular, assuming the gravitational mass is due to only the visible matter of the galaxies; galaxies far from the center of the cluster have much bigger velocities than predicted by the virial theorem.

The concept of dark matter was introduced by F. Zwicky[20] in 1933 who observed that the velocities of galaxies within the great clusters of galaxies (Coma

and Virgo) are too large for the gravity of the stars within the galaxies to hold the clusters together. This made him suggest the existence of DM which he, by then, called the "missing mass".

The mapping of the temperature and the mass density of hot X-ray emitting gas in a cluster of galaxies is used to determine the overall mass required for the hot gas to be gravitationally bound [21]. In addition, N-body simulation of the evolution of collisionless matter using the SMC is consistent with observed large scale structures, implying that DM plays an important role in the formation of these structures [22].

***At the scale of a galaxy:***

Similar methods used for large scale tests of the presence of matter apply at galactic scale too. The measure of galactic rotation curves, which illustrate the velocity of rotation versus the distance from the galactic center, gives an important experimental evidence for the existence of DM. The rotational velocity $v$ of an object on a stable Keplerian orbit with radius $r$ around a galaxy scales like $v(r) \sim \sqrt{M(r)/r}$, where $M(r)$ is the mass of the galaxy inside the orbit. With this relation we would expect a test particle beyond the point where the light from a galaxy effectively ceases to have a velocity $v(r) \sim r^{-\frac{1}{2}}$, considering only the luminous body to account for the mass content of the universe. But observationally, for spiral galaxies, [23, 24, 25] in the mentioned region the point particle is found to have $v \approx constant$, which can only be obtained by having a mass distribution $M(r) \sim r$ in $v(r) \sim \sqrt{M(r)/r}$, unless Newtonian dynamics fails at galactic scales

which is considered as a possibility[1] . This implies the existence of a dark halo, which for a spherical distribution of mass gives $\rho_{dark} \sim r^{-2}$, see Figure 2.10.

The study of X-ray emitting hot gases in elliptical galaxies also shows that the visible mass only makes up about 1% of the total mass [28, 29].

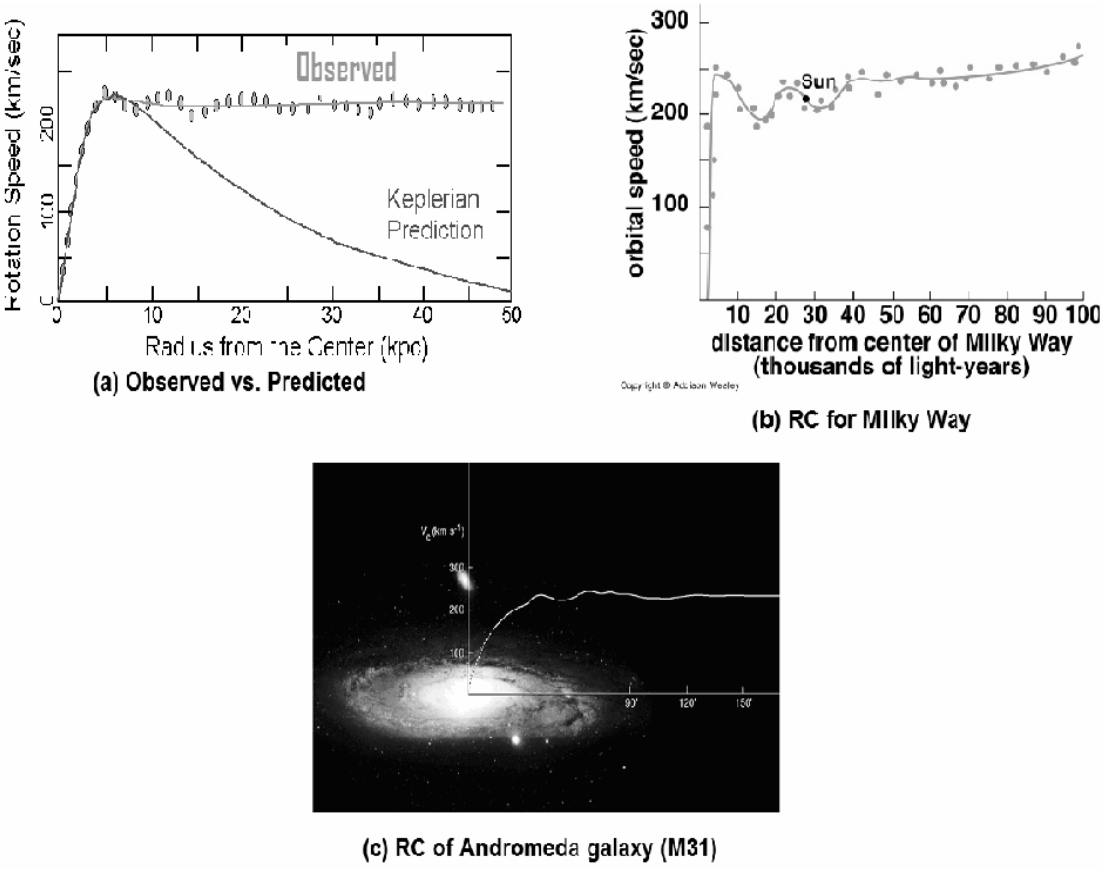


Figure 2.10: *Galactic Rotational curves (a) a sketch of the observed as compared with the expected according to Newtonian dynamics (b) that of Milkyway that confirms the presence of DM in our galaxy [1]*

[1] Rather than introducing a non luminous matter to explain galactic rotational curves, some scientists introduced the concept of new Modified Newtonian Dynamics [26], but this predicts a much lower third acoustic peak than observed by WMAP [10, 27]

***Cosmological parameters measurements from WMAP:***

The cosmological parameters from observations such as WMAP and Planck projects [30, 31] are in excellent agreement with the concordance model of big bang cosmology, namely ΛCMD (Λ-Cold Dark Matter). According to this model the universe comprises baryonic matter, non-baryonic cold dark matter and a cosmological constant Λ. The WMAP data gives the following values for matter and baryon density respectively; $\Omega_m h^2 = 0.1277 \pm 0.0080$ and $\Omega_b h^2 = 0.2229 \pm 0.00073$ implying the existence of non-baryonic matter. The detection of the structure of CMB (Cosmic Microwave Background radiation) acoustic peak as predicted by ΛCMB model implies that dark matter is non-baryonic. Models without dark matter are very poor fits to the data from WMAP implying a much lower third acoustic peak of CMB than what is observed.

***Evidence from Gravitational Lensing:***

Gravitational Lensing (GL) is one of the most important tools used to "weigh" the universe and study its geometry. Studying the image position and flux ratio of multiple image gravitational lens systems provides an invaluable insight about the mass distribution of the lens. In addition to image positions, the amount of distortion of background sources due to a foreground lens sheds light on the mass profile of the latter.

Direct parametric modeling of lenses as constrained by the image properties is the most widely practiced method of modeling total mass in galaxies. A galactic lens of $\sim 10^{12}$ solar masses creates images separated by few arc-seconds, while

clusters with total mass $\sim 10^{14}$ can strongly lens a background source into multiple images which are separated by up to an arc-minute [32]. These are typically observed values of image separations and the above amount of mass both in galaxies and clusters of galaxies is consistent with what is deduced from virial theorem. On the other hand, the visible mass is only about 10% of this total mass. In addition to individual clusters masses, the lensing of numerous background galaxies by clusters provide a more stringent constrain in matter density parameter $\Omega_m$ [28].

Weak lensing is also another tool used to determine the overall distribution of matter in clusters and the extent of galactic halos. The shearing of background galaxy shapes due to weak lensing by a foreground mass and a cumulative effect of the universe between the former and the observer is very small. As a result, we can not infer the total mass of the foreground lens like the case of strong lensing from a single background. But by studying the statistical shearing of background galaxies and accounting for shape noise, we can reconstruct the mass profile of the lens. The Bullet cluster in Figure 2.11 is reconstructed in the same manner.

### 2.3.2 Prospects of Dark Matter

Evidence is piling up that our universe is almost ordinary matter empty and rather filled with exotic things that we term as dark matter and dark energy. Hence we have now compelling reasons to look for possible candidates that could explain the nature of the dark side of the universe. This section gives a summary of some of the candidates for dark matter discussed in different literatures.

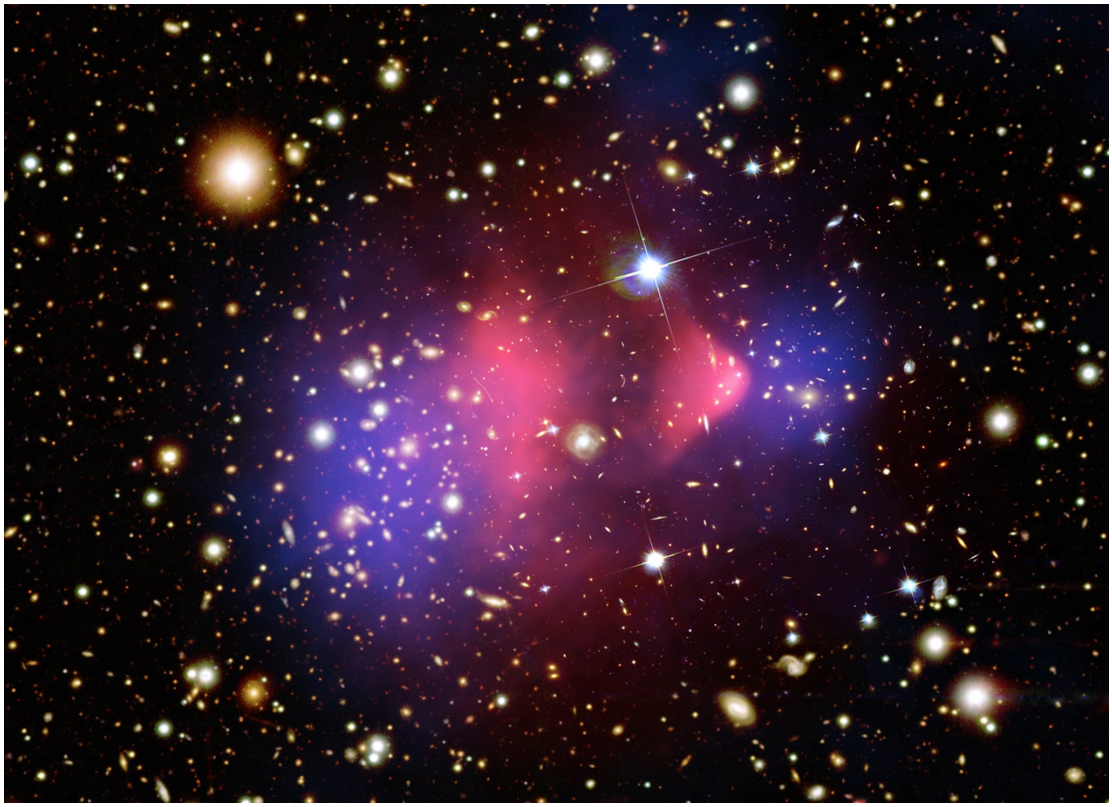

Figure 2.11: The Bullet Cluster showing two colliding clusters of galaxies with the smaller cluster receding away.

### *Baryonic dark matter candidates*

The fraction of critical density directly associated with light is measured by Astronomers to have a lower bound $\Omega_{lum} \approx 0.007$[33] while the mass of the universe in the form of baryons has $\Omega_B \approx 0.044$ [30]. Therefore, since $\Omega_B > \Omega_{lum}$, we can see the potential existence of baryonic dark matter. This actually is not a surprise because objects like black holes and neutron stars are made of baryons though they are not luminous. The term dark matter refers to not only those that do not emit radiation in the visible range but also those that do not emit radiation

of any range that can be detected. Hence ionized gas which is a strong emitter of X-rays and atomic gases that radiate strongly at 21 cm are excluded from the list of baryonic dark matter. Furthermore dust particles that emit IR radiation are also counted out. The other options are MACHOs (Massive Compact Halo Objects) which are baryonic matter that emit little or no radiation like brown dwarfs or planets. These objects were considered to contribute a large part of DM and were expected to be observed through their effect of gravitational lensing. Based on observation by MACHO collaboration of such objects by monitoring the luminosity of millions of stars in the Large and Small Magellanic Clouds for several years, it is concluded that MACHOs cannot contribute for more than 20% to the mass of galactic halo [34].

***Non-baryonic dark matter***

As already mentioned repeatedly, observations strongly suggest the existence of non-baryonic dark matter. In general, this category is further subdivided as hot or cold dark matter depending on whether the candidate was relativistic or non-relativistic upon decoupling. Relic particles from Big Bang should play a vital role as dark matter and the calculation of the present abundance of such candidates is well explained in the next chapter. The general characteristic of this particle dark matter could be summarized as follows:

- The relic particle should be neutral, i.e. no coupling with photons, otherwise they would have been already detected by electromagnetic interaction.
- They should be stable or should have life time at least comparable with the

age of the universe, so that they could account for the present observed dark matter density .

- Their interaction with ordinary matter should be weak or otherwise they would remain in thermal equilibrium, if they are thermal relics, for longer time than they actually did, so that their abundance by now is much less than observed. This statement will become more clear after the discussion of the relationship between freeze out abundance and reaction cross-section, one varies inversely with the other, in the next chapter. In addition, were they strongly coupled to ordinary matter their detection at collider experiment would have been easy, which unfortunately is not the case.

Below we discuss few of the many candidates

1. *Hot dark matter (HDM)*: neutrinos are the chief candidates of hot dark matter. If neutrinos are massless then their contribution to the total density is negligible. The current energy density of three species of massless neutrino is $\rho_\nu = \frac{21}{8}(4/11)^{\frac{4}{3}}\rho_\gamma$ [35], where $\rho_\gamma = 2.07\times10^{-51}$ GeV$^4$ is the present energy density of CMB. Hence massless neutrinos are ruled out as a candidate for DM. On the other hand, if neutrinos are massive they can significantly contribute for the composition of DM.

   A light neutrino that decouples when the rate of its weak interaction falls below the expansion of the universe at T $\sim$ MeV, for a spatially flat universe, the density parameter is given as [35]

$$\Omega_{\nu\bar{\nu}}h^2 = \frac{m_{\nu tot.}}{94\text{eV}}, \tag{2.33}$$

This implies for massive neutrino to account for the entire DM content of the universe , $\Omega_{DM} \approx .11$ , the average mass of the three families of $\nu$ should be $\approx$ 3.4 ev.. Recent discoveries [36, 37] have confirmed the existence of neutrino oscillation which implies that neutrinos are massive and they give an upper bound of 0.1 ev to mass of neutrino which according to the above argument implies that the entire DM is not represented by $\nu$. But with the mass bound from neutrino oscillation data, hot DM in the form of neutrino contributes as much as visible stars to the entire mass of the Universe.

A problem is associated with hot DM in that they fail to explain structure formation at small scales. Fast moving particles cannot clump together on such scale which puts neutrinos in doubt to be viable candidates for DM.

2. *Cold dark matter (CDM)*: This category is the most competent DM candidate. CDM remains as the most viable candidate because models involving it are very successful in providing the best explanation of structure formation compatible with observation. The two most theoretically motivated CDM candidates are Axions and Neutralinos; a highlight is given about them in this section.

   (a) Neutralinos [38, 28]: these are spin $\frac{1}{2}$ Majorana particles which are linear combinations of the super symmetric partners of photon, $Z^o$ and Higgs boson. These particles are one of the predictions of SUSY with a mass less than a few TeV, stable and weakly interacting with ordinary matter. The standard procedure of calculating the cosmological

abundance can be used to calculate the relic abundance for weakly interacting massive particles (WIMPs) which applies to thermal relics like the neutralinos.

(b) Axions: these are another CDM candidates with mass constrained to be less than 0.01eV from experimental search. They were first motivated as a possible solution to the strong CP-violation problem. Unlike many of particle DM candidates they are not thermal relics but irrespective of the fact that they are even much lighter than hot DM candidates they still move non-relativistically. A more elaborated discussion of the properties, possible production, the reason behind their theoretical invention and the like is given in [35].

# Chapter 3

# Type I Lenses

## 3.1 Introduction

Recovering projected mass distribution of galaxies and clusters given the images of lensed background sources is an important problem, and much effort has been devoted to lens mass modeling over the last couple of decades. In this Chapter we show that useful information about the lensing object can be obtained without any recourse to mass modeling. We work exclusively with quadruply imaged lens systems (the fifth central image is usually not detected and is not part of the analysis), and more specifically, with the angular distribution of the four point-like images around the lens center, that was introduced in [39]. We do not consider image fluxes.

A typical quad image configuration is shown in Figure 3.1. The images are labeled by their arrival time at the observer, 1 through 4. In most cases this

[0] This Chapter is published at MNRAS[2]

ordering can be determined from the morphology of the quad, without measured time delays [40]. Here we are interested only in the mass distribution of the lens, not its total mass (or, equivalently, its normalization), or orientation. In this case the image configuration of any quad is described uniquely by 6 parameters, which we chose to be of the polar variety, measured with respect to the lens center: three relative angles, and three distance ratios of images. The three relative angles between images are marked on the plot, $\theta_{12}$, $\theta_{34}$ and $\theta_{23}$. Angle $\theta_{12}$ is between the two minima of the arrival time surface, while $\theta_{34}$ is the angle between the saddle points. We define $\theta_{12}$ such that it encloses image 3, and $\theta_{34}$ such that it encloses image 2. Of the three angles, $\theta_{23}$ is special because the separation between images 2 and 3 gets arbitrarily small for sources approaching the diamond caustic shown in the lower right panels of Figure 3.1; when the source crosses the caustic these two images disappear and the quad becomes a double. Note that any linearly independent combination of the above three angles can be used, but we chose $\theta_{12}$, $\theta_{34}$ and $\theta_{23}$ because they have a simple physical meaning.

Working with only two angles, $\theta_{23}$ and a certain linear combination of $\theta_{12}$ and $\theta_{34}$, [39] showed that a wide range of simple, twofold symmetric lens models generate apparently indistinguishable patterns in the two dimensional plane of these angles. Twofold symmetric means that the mass distribution, and hence the potential, is symmetric about two orthogonal axes, and 'simple' excludes lenses with 'wavy' isodensity shapes. The simple, twofold symmetric class of lenses includes all popular parametric lens models, such as Singular Isothermal Ellipsoids (SIE), and Singular Isothermal Elliptical Potential (SIEP), as well lenses of any density profile and ellipticity.

The present work is an extension of [39], but here we work with the full set of three angles, $\theta_{12}$, $\theta_{34}$ and $\theta_{23}$. We show that quads from all simple lens mass distributions with twofold symmetry lie on nearly the same two dimensional surface in the three dimensional space of relative angles. We call this the Fundamental Surface of Quads (FSQ).

One can draw some interesting parallels between the FSQ we introduce here and the well studied Fundamental Plane of Ellipticals. Both of these lie in the three dimensional space whose axes are parameters describing the structural properties of the respective objects. In the case of quad lenses, these are the relative image angles, while in the case of ellipticals they are the effective radius, the surface brightness at the effective radius, and the central velocity dispersion. A wide class of objects belong to the Surface and the Plane with small scatter. In other words, the objects do not fill the full three dimensional space, implying that there is a tight relation between the three parameters. The existence of the Fundamental Plane is basically the consequence of the virial theorem, while the reason for the near invariance of the Fundamental Surface of Quads for a wide class of twofold symmetric lenses is yet to be identified.

## 3.2 The SIS+elliptical lensing model

We start by studying a simple, analytically tractable, two dimensional projected gravitational potential. It belongs to the generic family of separable potentials, $\phi(r, \theta) = r \cdot f(\theta)$, where $r$ and $\theta$ are polar coordinates in the lens plane. Properties of such potentials are discussed in Kassiola and Kovner [41], [42] and Dalal [43].

For our purpose we choose

$$f(\theta) = b[1 + \gamma\cos(2\theta)] \tag{3.1}$$

hence,

$$\phi = rb[1 + \gamma\cos(2\theta)] \tag{3.2}$$

which is sometimes called SIS+elliptical; we will call it SISell for short. The normalization factor $b$ is the Einstein radius, and $\gamma$ is the shear parameter.

The Poisson equation, $\Delta\phi = 2\kappa$, yields the projected dimensionless mass density profile,

$$\kappa = \frac{b}{2r}[1 - 3\gamma\cos(2\theta)]. \tag{3.3}$$

Note that $\gamma$ cannot be greater than $1/3$ since otherwise $\kappa$ will have an unphysical negative value. The lens equation,

$$\vec{r_s} = \vec{r} - \vec{\nabla}\phi \tag{3.4}$$

where $\vec{r_s}$ and $\vec{r}$ are source and image positions respectively, can be rewritten as two independent equations

$$r_s\cos(\theta - \theta_s) = r - b[1 + \gamma\cos(2\theta)] \tag{3.5}$$

$$r_s\sin(\theta - \theta_s) = -2b\gamma\sin(2\theta) \;\Rightarrow\; -a\sin(\theta - \theta_s) = \sin(2\theta), \quad a = \frac{r_s}{2b\gamma}. \tag{3.6}$$

Setting the magnification $M = 1/\det(A)$ , where $A$ is the Jacobian matrix of the lens equation, to infinity, i.e. $\det(A) = 0$, one gets

$$\det(A) = \frac{1}{r}\left[(r - b\{1 + \gamma\cos(2\theta)\}) + 4b\gamma\cos(2\theta)\right] = 0, \tag{3.7}$$

which yields the condition for the caustic,

$$r = b - 3b\gamma\cos(2\theta). \tag{3.8}$$

Now using equation (3.8) in the lens equation, eq. 3.6, allows one to express the caustic coordinates $(r_{sc}, \theta_{sc})$ in the source plane as a function of parameter $\theta$,

$$r_{sc} = b\gamma\sqrt{2[5 + 3\cos(4\theta)]} \tag{3.9}$$

$$\theta_{sc} = -\tan^{-1}\left(\tan^3\theta\right). \tag{3.10}$$

Our aim is to calculate the three relative angles, $\theta_{12}$, $\theta_{34}$ and $\theta_{23}$ for all the quads within the diamond caustic. Using eq. 3.6, which is independent of image distance $r$, we get the angular positions of the four images, in radians.

$$\theta_1 = \cos^{-1}\left(\tfrac{1}{2}\sqrt{C + \tfrac{-a^3\cos^3(\theta_s)+a(a^2-4)\cos(\theta_s)+8a\cos(\theta_s)}{4B}} - \tfrac{1}{4}a\cos(\theta_s) + \tfrac{B}{2}\right), \tag{3.11}$$

$$\theta_2 = \cos^{-1}\left(-\tfrac{1}{2}\sqrt{C - \tfrac{-a^3\cos^3(\theta_s)+a(a^2-4)\cos(\theta_s)+8a\cos(\theta_s)}{4B}} - \tfrac{1}{4}a\cos(\theta_s) - \tfrac{B}{2}\right), \tag{3.12}$$

$$\theta_3 = \cos^{-1}\left(\tfrac{1}{2}\sqrt{C - \tfrac{-a^3\cos^3(\theta_s)+a(a^2-4)\cos(\theta_s)+8a\cos(\theta_s)}{4B}} - \tfrac{1}{4}a\cos(\theta_s) - \tfrac{B}{2}\right), \tag{3.13}$$

$$\theta_4 = -\cos^{-1}\left(-\tfrac{1}{2}\sqrt{C + \tfrac{-a^3\cos^3(\theta_s)+a(a^2-4)\cos(\theta_s)+8a\cos(\theta_s)}{4B}} - \tfrac{1}{4}a\cos(\theta_s) + \tfrac{B}{2}\right), \tag{3.14}$$

where,

$$A = \sqrt[3]{108a^4\sin^2(2\theta_s) + 2\left(a^2-4\right)^3 + 12\sqrt{3}\sqrt{a^4\sin^2(2\theta_s)\left(27a^4\sin^2(2\theta_s) + \left(a^2-4\right)^3\right)}}, \tag{3.15}$$

$$B = \sqrt{\frac{\left(a^2-4\right)^2}{62^{2/3}A} + \frac{1}{4}a^2\cos^2(\theta_s) + \frac{1}{6}\left(4-a^2\right) + \frac{A}{12\sqrt[3]{2}}}, \tag{3.16}$$

$$C = -\frac{\left(a^2-4\right)^2}{62^{2/3}A} + \frac{1}{2}a^2\cos^2(\theta_s) + \frac{1}{3}\left(4-a^2\right) - \frac{A}{12\sqrt[3]{2}}. \tag{3.17}$$

The above equations are rather cumbersome and so preclude simple analytical expressions for the relative angles. Instead, we numerically generate random source positions within the caustic, calculate $\theta_i$'s using the above equations, and then compute relative angles.

The symmetry of the potential implies that it is sufficient to consider source positions only within one of the quadrants of the elliptical potential. Therefore, without any loss of generality we align the $x$-axis with the major axis of the ellipse and consider $\theta_s$ only from 0 to $\pi/2$. For a given $\theta_s$, $r_s$ can vary in the range $[0,r_{sc})$, therefore with eqs. 3.6 and 3.9 we see that $a$ runs in the range of $\left[0, 0.5\sqrt{2[5+3\cos(4\theta)]}\right)$, which is independent of $b$ and $\gamma$, where the parameter $\theta$ is determined by the value of $\theta_s$ using eq. 3.10.

## 3.3 The Fundamental Surface of Quads

We use the expressions for $\theta_i$'s given in the previous Section to parametrically plot the relative quad angles in the three dimensional space of $\theta_{12}$, $\theta_{34}$ and $\theta_{23}$.

The resulting distribution is a two dimensional surface, shown in Figure 3.2(a). The fact that it is a surface means that in a quad resulting from a SISell lens, two relative image angles completely determine the third.

The surface is simple with distinct properties. It has a slightly curved triangular shape–resembles a Dorito chip–with its apex at $(\theta_{12}, \theta_{34}, \theta_{23}) = (180°, 180°, 90°)$; quads at the apex have a "cross" configuration. The two edges connecting the apex to the base at $\theta_{23} = 0°$ correspond to $\theta_{12} = 180°$ and $\theta_{34} = 180°$, because in a twofold symmetric lens the latter two angles do not exceed 180°. Note that the base of the triangular surface that represents small values of $\theta_{23}$ and source positions close to the caustic, shows some unevenness, or jaggedness. It is unclear whether this is intrinsic to $\theta_i$ equations, or if it is due to the numerical noise arising from the implementation of these equations. In all what follows we ignore these small features; in particular, our fit to the surface, discussed below, smooths over this unevenness.

This surface is universal for all SISell lenses, however the meaning of universality requires some clarification. For a given source position $(\theta_s, r_s)$, a relative angle $\theta_{ij}$ depends on $b$ and $\gamma$, and therefore two SISell models with different $b$ and $\gamma$ give rise to two different points on the surface. However, the surface itself does not depend on $b$ and $\gamma$. This is the result of the elimination of $b$ and $\gamma$ dependence when considering all source positions within the caustic as discussed in Section 3.2. Therefore quads from SISell models of all shears and normalizations lie on the same invariant surface.

We would like to have an explicit functional form for the surface, as $\theta_{23} = \text{fcn}(\theta_{12}, \theta_{34})$, but since the equations for individual angles, eq. 3.11-3.14, contain

inverse cosines and are complicated, there is no simple expression. Instead, we calculate thousands of sets of relative angles, ($\theta_{12}$, $\theta_{34}$, $\theta_{23}$), from the expressions for the $\theta_i$'s (eq. 3.11-3.14) and fit these with a surface represented by a polynomial function in $\theta_{12}$ and $\theta_{34}$. The fitting was done using Matlab's Least Absolute Errors (LAE) method. As compared to the Least Squares method, LAE is less stable and could generate more than one function. We chose LAE anyway because it is resistant to outliers, which in our case correspond to quads with small values of $\theta_{23}$, and are responsible for the jaggedness of the surface.

We determine the optimal order of the polynomial by considering the deviations, or errors, of the SISell quad points from the fit surface, quantified by the root mean square error, RMSE. A number of trials and tests revealed that a fourth order polynomial[1] has the lowest value of RMSE, $\approx 0.00032$ radians, or $\approx 0.018°$, for approximately 160 thousand quads. We note that using different sets of quads to obtain the fit equation resulted in slightly different values for the coefficients of the polynomial, and for some sets of quads the RMSE varied by up to a factor of two.

To test the robustness of our fit to changes in the fitting method, we also computed the best fit surface using the Least Square method[2] , and using custom versus in-build polynomials within Matlab. Again, the resulting fit surface changed somewhat, but did not deviate substantially from the fit we present below. We conclude, therefore, that although the fit equation is not reproducible

[1] Matlab allows up to 5th degree polynomial fit.

[2] Numerical Recipes' Singular Value Decomposition routine did not provide a good fit when single precision was used, while in double precision `svdcmp` failed to invert the matrix at all.

exactly, it is completely adequate for our purposes:

$$\begin{aligned}\theta_{23} &= -5.792 + 1.783\,\theta_{12} + 0.1648\,\theta_{12}^2 - 0.04591\,\theta_{12}^3 - 0.0001486\,\theta_{12}^4 \\ &\quad +1.784\,\theta_{34} - 0.7275\,\theta_{34}\,\theta_{12} + 0.0549\,\theta_{34}\,\theta_{12}^2 + 0.01487\,\theta_{34}\,\theta_{12}^3 \\ &\quad +0.1643\,\theta_{34}^2 + 0.05493\,\theta_{34}^2\,\theta_{12} - 0.03429\,\theta_{34}^2\,\theta_{12}^2 - 0.04579\,\theta_{34}^3 \\ &\quad +0.01487\,\theta_{34}^3\,\theta_{12} - 0.0001593\,\theta_{34}^4 \end{aligned} \tag{3.18}$$

Figure 3.2(b) shows the fit as the gray semi-transparent surface. The red points are SISell quads corresponding to a random distribution of source positions within the diamond caustic, on the source plane. As depicted in the Figure, a random distribution of source positions does not imply a random distribution of quads on the Fundamental Surface; quad density increases with increasing $\theta_{23}$. Two other orientations of the Fundamental Surface are shown in Figure 3.3.

Because the RMSE of the SISell quad distribution about the fit plane is $\sim 0.02^\circ$ the differences between the two will be invisible in the full three dimensional angles space. Instead, we calculate the difference in $\theta_{23}$ of the SISell quads and the fitted surface keeping the other two angles fixed; we call this difference $\Delta\theta_{23} = \theta_{23} - \theta_{23,fit}$, where $\theta_{23,fit}$ is obtained by plugging $\theta_{12}$ and $\theta_{34}$ of a quad in to eq. 3.18. Figure 3.4 plots $\Delta\theta_{23}$ vs. $\theta_{23}$. The straight horizontal line represents the surface fit, eq. 3.18, while the points are the SISell quads. The wiggles in the distribution of points represents the wiggles in the SISell surface, compared to the fourth order polynomial fit. However, for all practical purposes, the differences are negligible, and eq. 3.18 can be taken to be a good representation of the SISell potential.

We call this surface the Fundamental Surface of Quads because, as we show in the next section, not just SISell, but most twofold symmetric models do not

differ from it by more than a few degrees. This near invariance probably stems from the shape of the caustic of this class of potentials. The twofold symmetry of the lensing mass distribution implies the twofold symmetry of the diamond caustic. More specifically the diagonals of the caustic intersect at 90° and all four quadrants of the caustic are identical.

## 3.4 Other two-fold symmetric potentials

In this Section we explore a wider range of simple twofold symmetric mass models, motivated by the commonly used parametric models. We choose two different radial density profiles, isothermal (SIS), and de Vaucouleurs (deV). Here, isothermal means that if mass ellipticity were zero, the projected density profile would scale as $1/r$. The de Vaucouleurs profile has projected density given by,

$$\Sigma = \Sigma_e \exp\left(-7.673\left[(r/r_e)^{1/4} - 1\right]\right), \tag{3.19}$$

where $r_e$ is the half-mass radius, and $\Sigma_e$ is the projected mass density at $r_e$. To generate a diamond caustic the density profiles must be accompanied by either ellipticity, $e$, or external shear, $\gamma$. Ellipticity, $e$ of the mass isodensity contours is related to the axis ratio of the isodensity contours, $b/a = (1-e)/(1+e)$. We present a total of four models: SIS with $e = 0$ and $\gamma = 0.3$; deV with $e = 0$ and $\gamma = 0.4$; SIS with $e = 0.3$ and $\gamma = 0$; deV with $e = 0.4$ and $\gamma = 0$.

Each mass model generates a two dimensional surface in the three dimensional space of relative angles. All surfaces coincide at the apex, where $(\theta_{12}, \theta_{34}, \theta_{23}) = (180°, 180°, 90°)$, since all twofold symmetric models can produce a perfect cross

configuration (though the distance ratios of images will differ). At other locations the surfaces deviate from each other somewhat, and from the one defined by SISell; largest deviations are seen at small $\theta_{23}$ values, i.e. towards the base of the triangular surface. However, even at the widest separation, the surfaces differ by only a few degrees. The left panel of Figure 3.5 shows that these differences are hard to discern in the full three dimensional angles space, even if the surface is split up into four pieces for easier visualization. To make the deviations visible, in the right panel of Figure 3.5 we fold the surface along the vertical mid-line, and show only a narrow range of angles, a few degrees in each case. In this zoom, the deviations are seen to be a few degrees.

Another way to show deviations is to use $\Delta\theta_{23}$ introduced in the previous Section; see Figure 3.6. As before the horizontal line at $\Delta\theta_{23} = 0$ represents the Fundamental Surface of Quads, given by the fit eq. 3.18, and the points are quads from the four mass models. The isothermal models and the de Vaucouleurs models are shown in the left and right panels, respectively. The top row shows the models with external shear, $\gamma$, while the bottom rows represent elliptical mass distributions.

To quantify the effect of shear or ellipticity on any given mass model, we quote the average distance ratio $< d_4/d_1 >$, where $d_1$ and $d_4$ are the distances of the first and fourth arriving images from the lens center, and the average is over quads randomly populating the inside of the diamond caustic. A given lens mass distribution produces quads with a range of image distance ratios, but in general image 1 tends to be farthest from the lens center, while image 4 tends to be closest. For the four models, $< d_4/d_1 > \sim 0.75 - 0.79$. For the sample of 40

observed quads (Section 3.5) $< d_4/d_1 > \sim 0.68$. i.e. more extreme than our four models. As will be discussed in the next Section many of the observed quads are the result of mass distributions that are more involved than two-fold symmetric lenses; most require an external shear in addition to and elliptical lens, while some require substructure. The presence of these would tend to reduce the $d_4/d_1$ ratio.

Note that the vertical axes range are different in the top and bottom panels of Figure 3.6. As opposed to the quad distributions generated by the elliptical mass models, the ones from models with external shear are much closer to the FSQ, and appear more similar to that of the SISell model. When viewed in 3D, the surface containing quads from the elliptical lens models sags below the FSQ, but even for the bottom two panels of Figure 3.6 the differences in $\theta_{23}$ are $< 4^\circ$, for $e = 0.4$, or axis ratio $b/a = 0.43$, or an E5.7 if it were an optical elliptical galaxy. The RMSE is around $1.5^\circ$. Larger ellipticities (or larger $\gamma$) would result in larger deviations from the FSQ.

Also note that for very large ellipticities two opposite cusps of the diamond caustic protrude outside of the oval caustic producing so-called naked cusps, which do not produce quads. The corresponding surfaces of relative angles look similar to the ones without the naked cusps, except that the portions at the bottom corners of the surface are devoid of quads.

## 3.5 Observed Quads

In this Section we illustrate one of the practical uses of the Fundamental Surface of Quads (FSQ).

Galaxy lens systems can be approximately divided into three categories, depending on whether the lens mass model is (a) an elliptical mass distribution or a circularly symmetric mass distribution with an external shear, (b) an elliptical mass distribution plus some external shear, or (c) a more complicated mass distribution, possibly with additional lens galaxies or substructure mass clumps. A survey of the literature indicates that only a handful of systems belong to (a). A model-free way to come to that conclusion is to look at the quads in the 3D angles space.

We have assembled a sample of 40 galaxy-lens quads. The sample was collected from all available sources, and is therefore heterogeneous. Where possible, the astrometry, including the positional uncertainties on the images and the lensing galaxy was taken from the CASTLeS web-site [16]; otherwise from individual papers. In the latter case, systems listed in Table 3.1 have a footnote with a reference; a lens system with no reference means that its data were obtained entirely from CASTLeS. The image arrival time was determined from the morphology of the lens [40], and the relative angles were calculated. These are listed in Table 3.1, in columns labeled $\theta_{12}$, $\theta_{34}$ and $\theta_{23}$.

In Figure 3.7 we show two orientations of the 3D angles space with the FSQ and the 40 quads. For clarity, we do not show errors in this plot. The main conclusion is that most observed quads lie more than a few degrees away from the FSQ; 12 are within $\pm 2^\circ$, so most cannot be modeled adequately with an elliptical lens, or a circularly symmetric lenses with external shear.

Next, we incorporate errors into the analysis. Even though the astrometric measurement errors of images and galaxy lens center are largely independent of

each other, a shift in the lens center translates into correlated relative angle errors. To account for this we calculate the errors as follows. We assume that the $x$, $y$ positional errors of each of the four images and the lens center are normally distributed, with $\sigma_x$ and $\sigma_y$ taken from the literature. We then draw thousands of independent image and lens center positions, and for each generated lens system calculate relative angles $\theta_{12}$, $\theta_{34}$ and $\theta_{23}$. The thousands of generated quads per lens system then give us the error distribution for each of the three relative angles. We calculate the mean and the rms of these distributions, and list them in columns labeled $\theta_{ij,errors}$ in Table 3.1. Note that the average of these distributions need not be the same as $\theta_{ij}$, however, the differences tend to be small, generally $< 0.1^\circ$.

We quantify the deviation of the quads from the FSQ as in earlier Sections, by calculating $\Delta\theta_{23}$. The error in $\Delta\theta_{23}$, listed as $\Delta\theta_{23,errors}$ is calculated similarly to what was described above, using thousands of quads generated based on astrometric uncertainty.

Figure 3.8 shows the distribution of the 40 quads in the $\theta_{23}$ vs. $\Delta\theta_{23}$ plane. Within error-bars, only 10 systems are consistent with FSQ. Several of these have published parametric modeling, and are, in fact, well represented by two-fold symmetric mass distributions. For example, B2045+265 is successfully modeled by [44] using SISell potential, eq. 3.2. SDSS J002240 is modeled by [45] with Singular Isothermal Ellipsoid (SIE) using `gravlens` software of [46]. The same software was used by [47] to fit the positions (not the flux ratios) of SDSS J1538 with three types of twofold symmetric models: de Vaucoulers, SIE and a power law density profile.

On the other hand, some of the lenses which lie away from the FSQ are known

to require external shear in addition to elliptical lens. PG 1115 where the lensing galaxy is a member of a galaxy group is inconsistent with FSQ; its $|\Delta\theta_{23}| \sim 4°$. RXJ 0911+0551 has a cluster next to it [48], so the lens model requires an external shear in addition to an elliptical galaxy lens; its $|\Delta\theta_{23}| \sim 6°$. For LSD Q0047-2808, [49] state that SIE+shear does not fit the image positions well (but sufficient for the determination of the Einstein ring radius); it has $|\Delta\theta_{23}| \sim 14°$. Lenses with known secondary galaxies also lie far from the FSQ. HE 0230-2130 has a secondary lensing galaxy [50] very close to the images, and so its $|\Delta\theta_{23}| \sim 30°$. B1608 has a complicated galaxy merger as a lens, and its $|\Delta\theta_{23}| \sim 5°$, and so it is inconsistent with the FSQ.

A few caveats are in order. If a quad does not lie within a couple of degrees of the Fundamental Surface of Quads (i.e. the range defined by the various density profile and ellipticity models, such as the ones in Figure 3.5 and 3.6), it cannot be modeled by a twofold symmetric lens. However, the opposite need not be true. If a quad lies on the FSQ does that immediately imply that it can be modeled by a twofold symmetric lens, regardless of its image distance ratios? This question will be addressed in a future study. We also note that even if a quad does belong to the locus of twofold symmetric lens in the full 6D space of image position properties, it does not mean that other types of lens models cannot fit it. Reconstruction of the lens mass reconstruction from single quads is a highly underconstrained problem, so the solution is not unique, and many mass models can reproduce the image positions exactly [51].

## 3.6 Conclusions and Future Work

In this Chapter we present a model-free way of making inferences about the lensing mass distribution given its quad image positions. The latter are represented by three relative angles that describe the distribution of images around the lens center. We show that in the three dimensional space of these angles, quads generated by SIS+elliptical mass distribution belong to an invariant two dimensional surface, regardless of the shear parameter $\gamma$, and normalization $b$. Furthermore, quads from a wider class of lenses with twofold symmetry outline almost the same surface, making the surface a near invariant descriptor of twofold symmetric mass distributions. Because of that property we call the two dimensional surface the Fundamental Surface of Quads (FSQ).

The existence of FSQ allows one to characterize galaxies and clusters based on the quads they generate. To aid in that, we provide a fitting formula for the FSQ based on the SIS+elliptical lensing potential. If a quad does not lie within a couple of degrees of the FSQ (i.e. the range defined by the various density profile and ellipticity models, such as the ones in Figure 3.5 and 3.6), the mass distribution is not twofold symmetric. This method of determining if a lens can be fit with a twofold symmetric lens is superior to answering this question using parametric modeling. The latter fits quads with a finite set of models, while our method addresses all twofold symmetric models irrespective of the specific parametric form.

However, the main importance of the FSQ is not in ascertaining if the lens mass distribution is twofold symmetric or not, but in the following aspects, which

we will investigate in Chapter 4. First, the near invariance of FSQ provides a new framework for studying quads, and strong lensing theory in general. We remind the reader that it is still not understood why a wide class of twofold symmetric lenses form such a tight, near invariant distribution in the space of relative angles. Second, as already shown in [39], the relative angles present a promising way of investigating realistic mass distributions, and specifically, differentiating substructured lenses from smooth non-twofold symmetric ones. Finally, the full set of quad image properties lives in the six dimensional space that includes image distance ratios. An investigation of this space is yet to be undertaken.

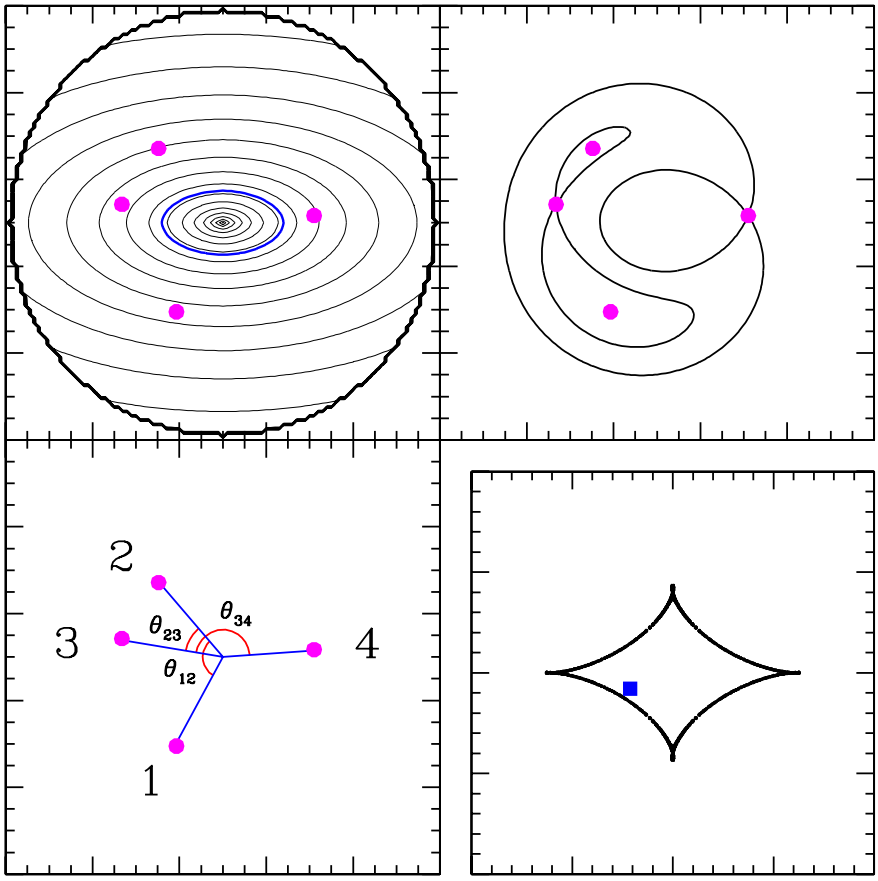


Figure 3.1: A representative quad from a twofold symmetric lens. *Top left:* An elliptical lens mass distribution, with the $\kappa = 1$ contour shown as a thick blue line. Images are the magenta filled circles. *Top right:* Arrival time contours and images. *Bottom left:* Images, labeled by arrival time. The relative angles, $\theta_{12}$, $\theta_{23}$ and $\theta_{34}$ are marked. *Bottom right:* The diamond caustic, with the location of the source represented by a solid blue square.

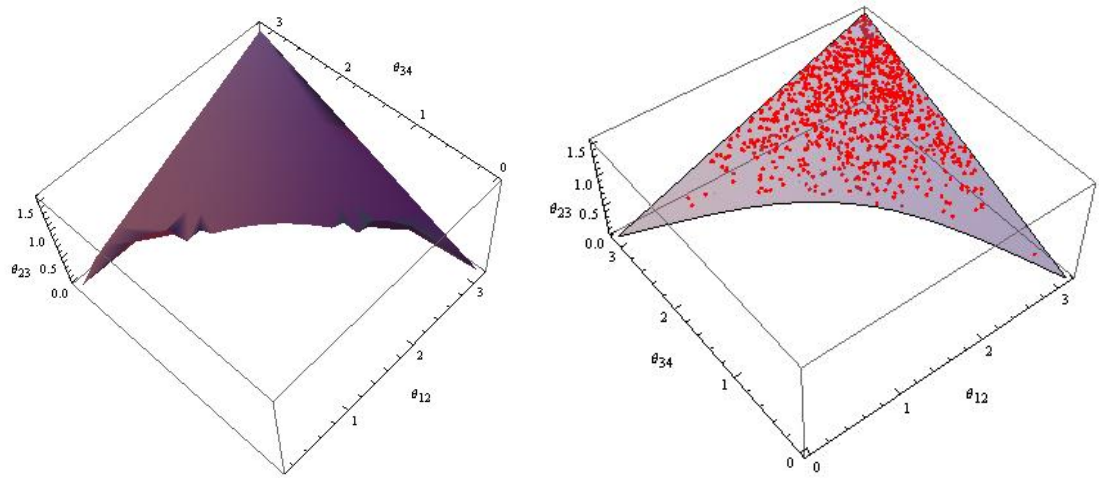


Figure 3.2: The three dimensional space of three image angles, $\theta_{12}$, $\theta_{23}$ and $\theta_{34}$ for the SIS+elliptical, or SISell mass distribution. (a) The surface outlined by quads whose relative image angles were calculated using eq. 3.11-3.14. (b) The fit surface to the Fundamental Surface of Quads (FSQ), eq. 3.18, is shown as the gray surface, while the points are quads randomly distributed within the diamond caustic in the source plane.

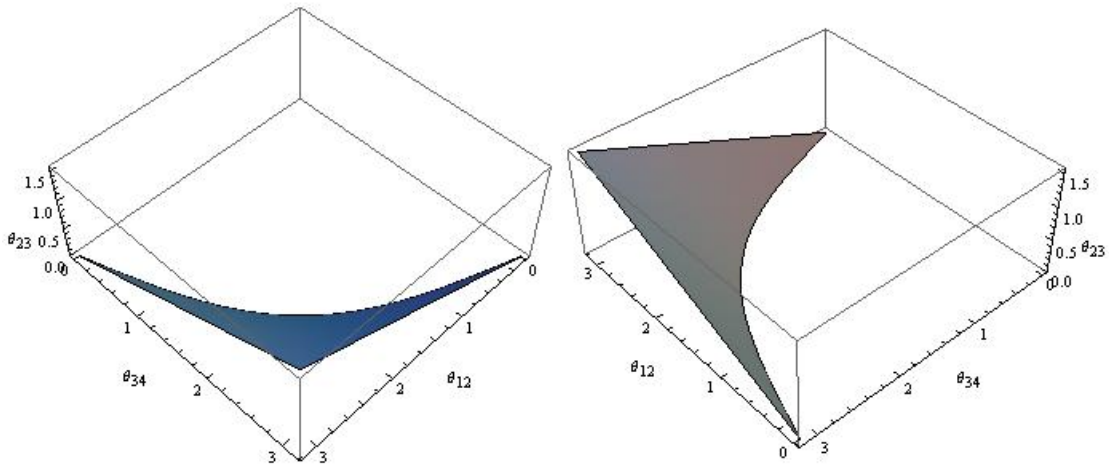


Figure 3.3: Two additional orientations of the Fundamental Surface of Quads.

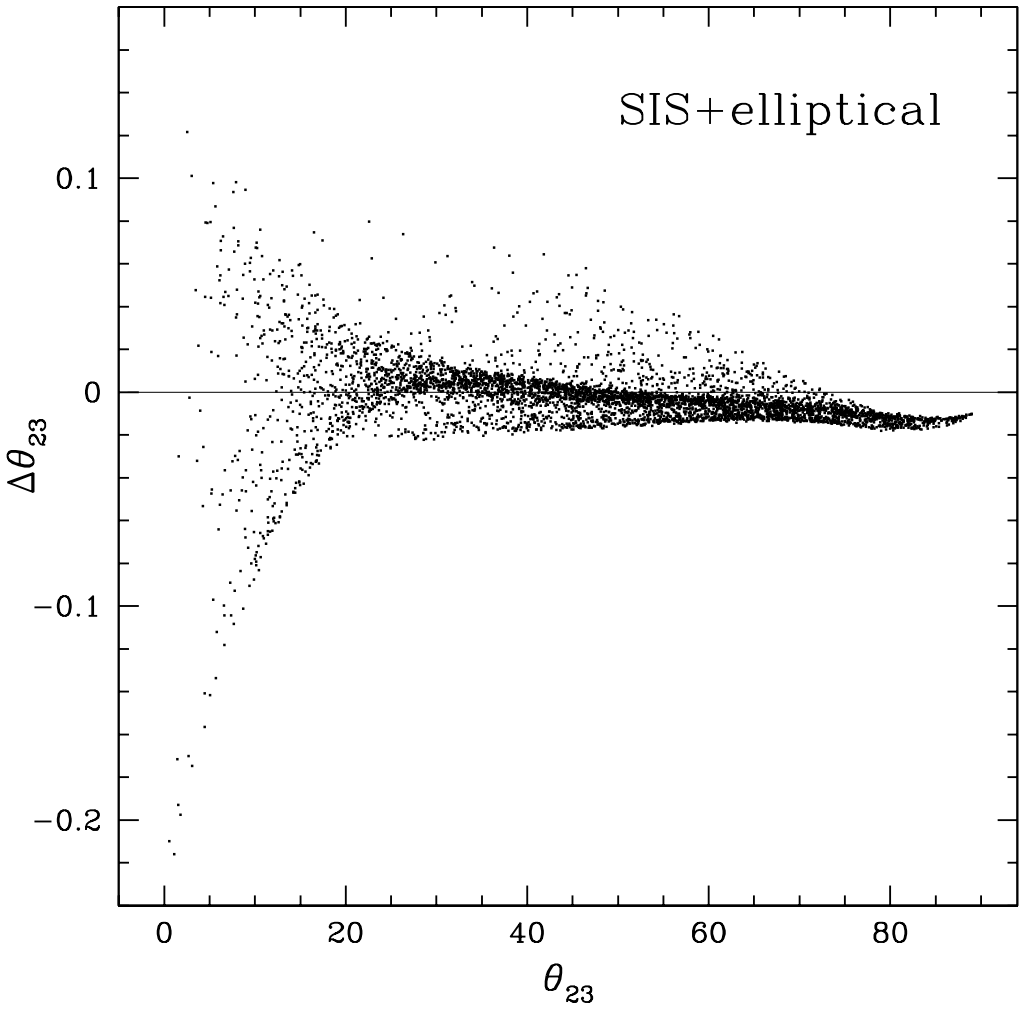


Figure 3.4: Deviations of the SISell quads from the best fit 4th degree polynomial presented in equation 3.18. The vertical axis shows the deviations of the quads' $\theta_{23}$ from the prediction of equation 3.18. The quads used to compute the best fit were obtained using analytical equations for angles $\theta_1$, $\theta_2$, $\theta_3$ and $\theta_4$ presented in Section 3.2, while the quads in this Figure were generated using a ray tracing code. The difference between the two is small.

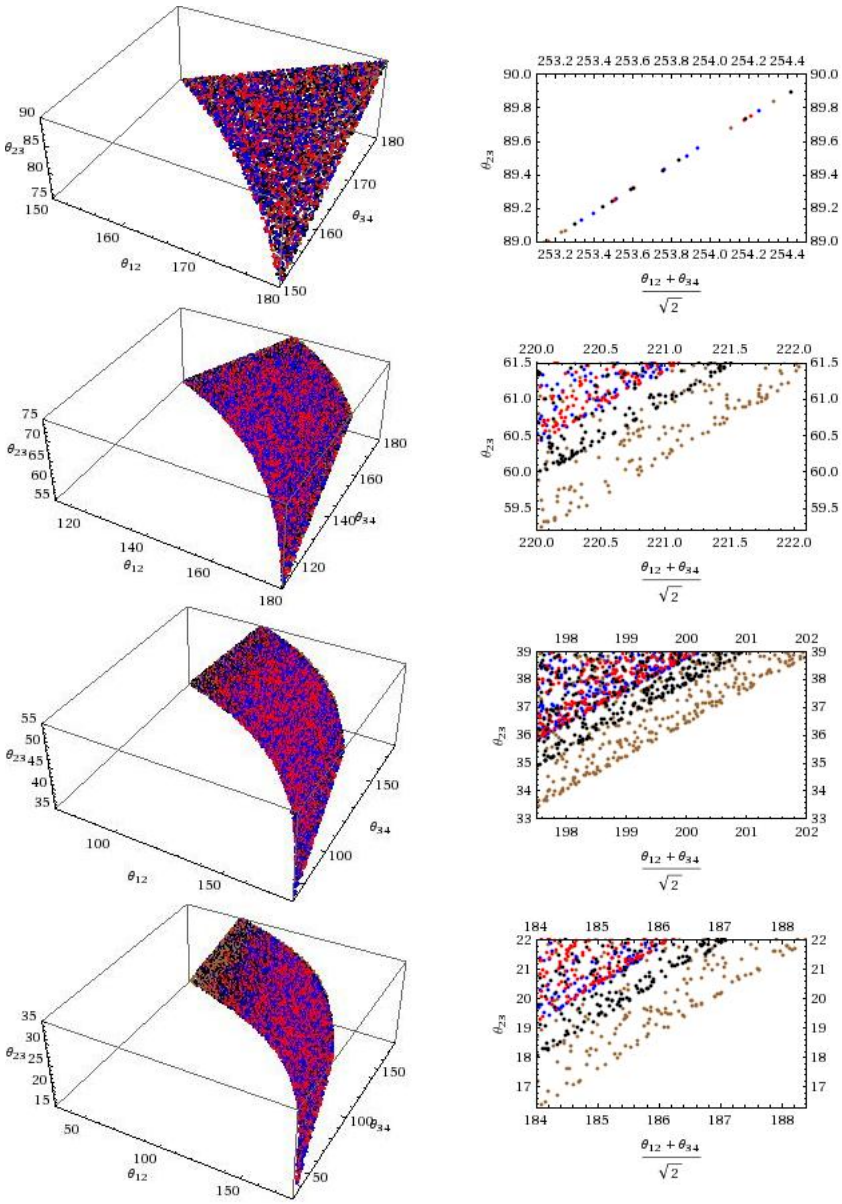


Figure 3.5: Simple twofold symmetric lens mass distributions define a nearly invariant Fundamental Surface of Quads. Quads from four mass models are shown: SIS with $e = 0$ and $\gamma = 0.3$ (red); deV with $e = 0$ and $\gamma = 0.4$ (blue); SIS with $e = 0.3$ and $\gamma = 0$ (black); deV with $e = 0.4$ and $\gamma = 0$ (brown). On the left we show the 3D space of relative angles sliced into four segments divided by $\theta_{23} = 35°, 55°, 75°$. The fact that the points of different lens potentials are hard to tell apart demonstrates the near invariance of the FSQ. To make the deviations visible, on the right we fold and project a small angle range of the surface; see Section 3.4 for details.

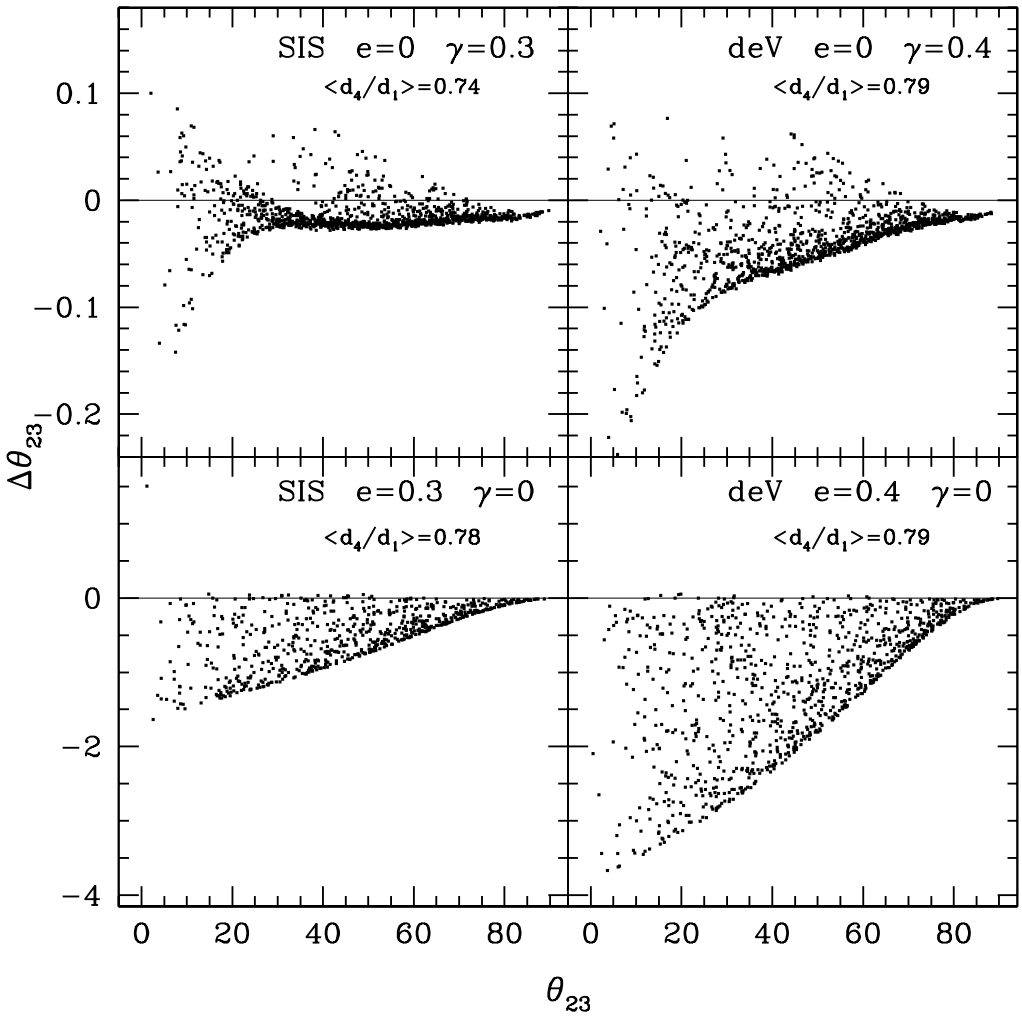


Figure 3.6: The deviations of the quads of four mass distributions from the predictions of the 4th degree polynomial fit, equation 3.18. The four mass distributions are the same as the ones shown in Figure 3.5 *Top left:* circularly symmetric SIS with external shear $\gamma = 0.3$; *Top right:* circularly symmetric de Vaucouleurs profile with external shear $\gamma = 0.4$; *Bottom left:* SIS with ellipticity $e = 0.3$; *Bottom left:* de Vaucouleurs profile with ellipticity $e = 0.4$. The average value of the distance ratio of the fourth to first arriving image, $< d_4/d_1 >$, is shown in each panel. This aids in visualizing the meaning of $\gamma$ and $e$ value. Note that the vertical axes have different ranges in the top and bottom panels.

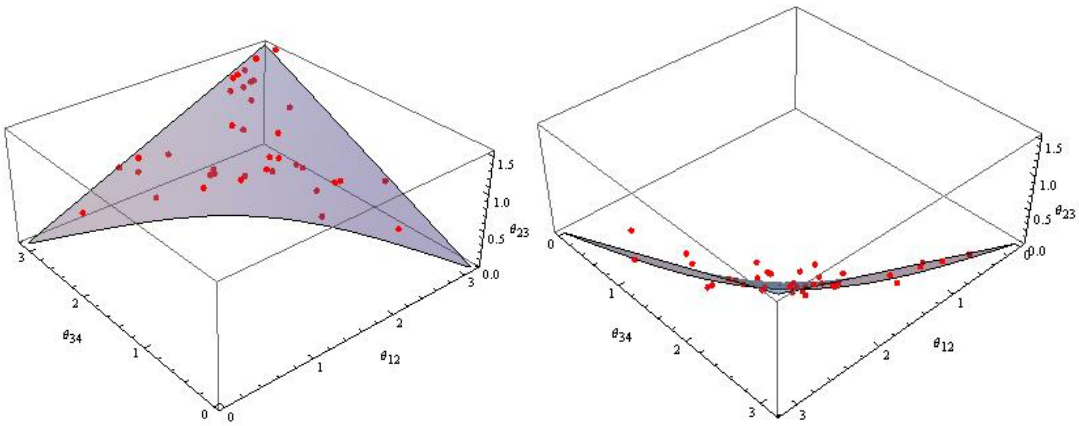


Figure 3.7: The Fundamental Surface of Quads fit equation (shaded region) and the forty observed galaxy quads (red dots). Two orientations are shown; in the second one the deviation of the observed quads from the Plane are clearly visible.

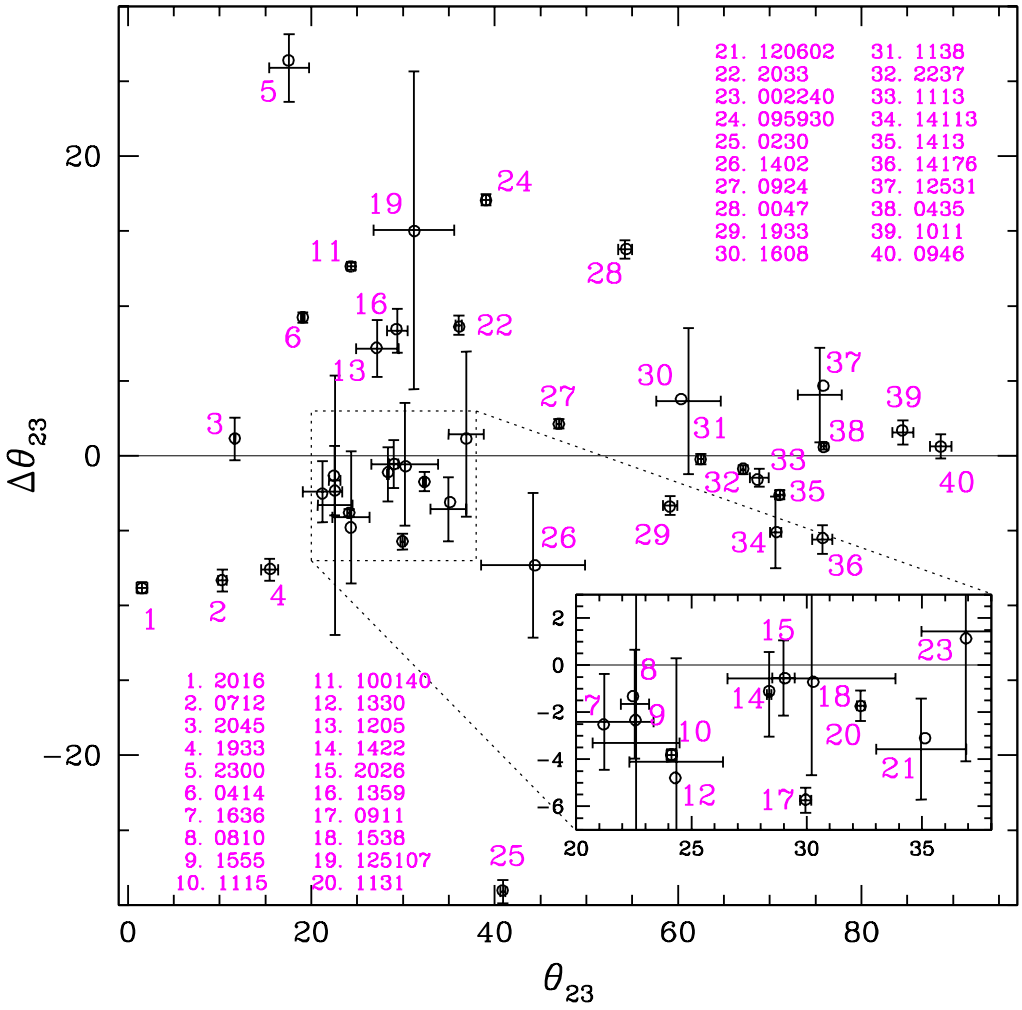


Figure 3.8: Deviations, $\Delta\theta_{23}$, of the observed quads from the FSQ. The horizontal axis is the observed $\theta_{23}$. The empty circles represent the observed relative angles and their deviations from the FSQ. The error bars are calculated as explained in Section 3.5. The horizontal and vertical axes values are given in Table 3.1.

Table 3.1: Relative Angles

| N | Lens name | $\theta_{12}$ | $\theta_{12,\text{errors}}$ | $\theta_{34}$ | $\theta_{34,\text{errors}}$ | $\theta_{23}$ | $\theta_{23,\text{errors}}$ | $\Delta\theta_{23}$ | $\Delta\theta_{23,\text{errors}}$ |
|---|---|---|---|---|---|---|---|---|---|
| 1 | MG 2016+112 | 150.8 | 150.7 ± 0.4 | 91.4 | 91.3 ± 0.6 | 1.5 | 1.5 ± 0.6 | -8.8 | -8.8 ± 0.4 |
| 2 | B 0712+472 | 79.8 | 79.8 ± 0.3 | 163.2 | 163.3 ± 0.7 | 10.2 | 10.3 ± 0.4 | -8.3 | -8.3 ± 0.7 |
| 3 | B 2045+265 | 34.9 | 34.9 ± 0.1 | 175.2 | 175.2 ± 1.0 | 11.7 | 11.7 ± 0.1 | 1.2 | 1.1 ± 1.4 |
| 4 | B 1933+503 lobe | 155.5 | 155.5 ± 0.7 | 101.7 | 101.7 ± 0.9 | 15.5 | 15.5 ± 0.9 | -7.6 | -7.6 ± 0.7 |
| 5 | SLACS J2300+002 | 160.8 | 161.2 ± 2.0 | 38.5 | 38.5 ± 2.0 | 17.5 | 17.6 ± 2.2 | 26.4 | 25.9 ± 2.3 |
| 6 | MG 0414+0534 | 101.5 | 101.5 ± 0.3 | 144.1 | 144.1 ± 0.3 | 19.1 | 19.1 ± 0.2 | 9.2 | 9.2 ± 0.3 |
| 7 | SLACS J1636+470 | 128.0 | 127.9 ± 1.8 | 136.9 | 136.9 ± 2.5 | 21.2 | 21.2 ± 2.1 | -2.5 | -2.4 ± 2.0 |
| 8 | HS 0810+2554 | 111.3 | 111.5 ± 1.1 | 150.1 | 150.4 ± 2.3 | 22.5 | 22.5 ± 0.6 | -1.3 | -1.7 ± 2.3 |
| 9 | B 1555+375 | 114.0 | 113.1 ± 5.9 | 149.3 | 150.6 ±10.7 | 22.6 | 22.6 ± 1.9 | -2.3 | -3.3 ± 8.7 |
| 10 | PG 1115+080 | 141.9 | 141.9 ± 0.3 | 127.5 | 127.5 ± 0.4 | 24.1 | 24.1 ± 0.2 | -3.8 | -3.8 ± 0.3 |
| 11 | J 100140.12+020 | 120.4 | 120.4 ± 0.1 | 131.3 | 131.3 ± 0.5 | 24.3 | 24.3 ± 0.4 | 12.6 | 12.7 ± 0.2 |

*continued on the next page*

Relative Angles

| N | Lens name | $\theta_{12}$ | $\theta_{12,\mathrm{errors}}$ | $\theta_{34}$ | $\theta_{34,\mathrm{errors}}$ | $\theta_{23}$ | $\theta_{23,\mathrm{errors}}$ | $\Delta\theta_{23}$ | $\Delta\theta_{23,\mathrm{errors}}$ |
|---|---|---|---|---|---|---|---|---|---|
| 12 | SDSS J1330+1810 | 115.6 | 115.7 ± 3.2 | 152.2 | 151.5 ± 4.8 | 24.3 | 24.3 ± 2.0 | -4.8 | -4.1 ± 4.4 |
| 13 | SLACS J1205+491 | 159.1 | 159.3 ± 1.9 | 90.4 | 90.3 ± 2.1 | 27.1 | 27.2 ± 2.3 | 7.2 | 7.2 ± 1.9 |
| 14 | B 1422+231 | 74.8 | 74.8 ± 0.3 | 173.8 | 174.0 ± 1.4 | 28.4 | 28.4 ± 0.1 | -1.1 | -1.2 ± 1.8 |
| 15 | WFI 2026-4536 | 154.1 | 154.1 ± 1.8 | 113.6 | 113.5 ± 1.3 | 29.1 | 29.0 ± 0.5 | -0.5 | -0.5 ± 1.6 |
| 16 | CLASS B1359+154 | 135.9 | 135.8 ± 1.2 | 125.8 | 126.1 ± 3.2 | 29.3 | 29.4 ± 1.1 | 8.4 | 8.3 ± 1.5 |
| 17 | RXJ 0911+0551 | 180.7 | 180.7 ± 0.5 | 69.6 | 69.7 ± 0.4 | 29.9 | 29.9 ± 0.2 | -5.7 | -5.7 ± 0.5 |
| 18 | SDSS J1538+5817 | 152.7 | 152.7 ± 4.0 | 117.7 | 117.3 ± 4.0 | 30.3 | 30.2 ± 3.6 | -0.7 | -0.6 ± 4.1 |
| 19 | SDSS J125107 | 158.8 | 158.1 ± 9.9 | 85.2 | 86.4 ± 8.8 | 31.3 | 31.2 ± 4.4 | 15.0 | 15.1 ±10.6 |
| 20 | RXJ 1131-1231 | 66.0 | 66.0 ± 0.2 | 180.9 | 180.8 ± 0.5 | 32.3 | 32.3 ± 0.2 | -1.8 | -1.7 ± 0.6 |
| 21 | SDSS J120602.09 | 96.0 | 95.9 ± 2.2 | 171.6 | 171.9 ± 2.1 | 35.1 | 35.0 ± 2.0 | -3.1 | -3.6 ± 2.1 |
| 22 | WFI 2033-4723 | 140.6 | 140.5 ± 0.6 | 128.5 | 128.5 ± 0.7 | 36.1 | 36.1 ± 0.3 | 8.6 | 8.7 ± 0.6 |

*continued on the next page*

Relative Angles

| N | Lens name | $\theta_{12}$ | $\theta_{12,\mathrm{errors}}$ | $\theta_{34}$ | $\theta_{34,\mathrm{errors}}$ | $\theta_{23}$ | $\theta_{23,\mathrm{errors}}$ | $\Delta\theta_{23}$ | $\Delta\theta_{23,\mathrm{errors}}$ |
|---|---|---|---|---|---|---|---|---|---|
| 23 | SDSS J002240 | 77.9 | 78.3 ± 1.8 | 177.5 | 177.1 ± 4.4 | 36.9 | 36.9 ± 1.9 | 1.1 | 1.4 ± 5.5 |
| 24 | J 095930.94+023 | 141.2 | 141.2 ± 0.4 | 120.9 | 121.0 ± 0.5 | 39.0 | 39.1 ± 0.5 | 17.0 | 17.1 ± 0.4 |
| 25 | HE 0230-2130 | 127.2 | 127.2 ± 0.3 | 186.7 | 186.8 ± 0.9 | 40.9 | 40.9 ± 0.3 | -29.0 | -29.1 ± 0.8 |
| 26 | SDSS 1402+6321 | 142.6 | 142.7 ± 6.1 | 156.1 | 155.7 ± 6.8 | 44.4 | 44.2 ± 5.6 | -7.3 | -7.3 ± 4.8 |
| 27 | SDSS 0924+0219 | 153.6 | 153.6 ± 0.4 | 135.9 | 135.9 ± 0.5 | 47.0 | 47.0 ± 0.3 | 2.1 | 2.1 ± 0.3 |
| 28 | LSD Q0047-2808 | 130.9 | 130.8 ± 0.7 | 152.8 | 152.7 ± 0.8 | 54.3 | 54.2 ± 0.8 | 13.8 | 13.8 ± 0.6 |
| 29 | B 1933+503 core | 169.1 | 169.1 ± 0.8 | 142.8 | 142.8 ± 0.8 | 59.1 | 59.1 ± 0.8 | -3.4 | -3.3 ± 0.6 |
| 30 | B 1608+656 | 97.9 | 99.2 ± 5.9 | 186.7 | 187.2 ± 4.9 | 60.3 | 61.1 ± 3.5 | 3.8 | 3.7 ± 4.9 |
| 31 | SDSS 1138+0314 | 153.1 | 153.1 ± 0.5 | 161.1 | 161.1 ± 0.6 | 62.5 | 62.5 ± 0.3 | -0.2 | -0.2 ± 0.4 |
| 32 | Q 2237+0305 | 146.3 | 146.3 ± 0.4 | 173.4 | 173.5 ± 0.6 | 67.1 | 67.1 ± 0.3 | -0.9 | -0.9 ± 0.3 |
| 33 | HE 1113-0641 | 154.4 | 154.6 ± 1.2 | 170.3 | 170.3 ± 1.2 | 68.6 | 68.9 ± 1.0 | -1.6 | -1.5 ± 0.6 |

*continued on the next page*

Relative Angles

| N | Lens name | $\theta_{12}$ | $\theta_{12,\text{errors}}$ | $\theta_{34}$ | $\theta_{34,\text{errors}}$ | $\theta_{23}$ | $\theta_{23,\text{errors}}$ | $\Delta\theta_{23}$ | $\Delta\theta_{23,\text{errors}}$ |
|---|---|---|---|---|---|---|---|---|---|
| 34 | HST 14113+5211 | 163.2 | 163.2 ± 0.6 | 171.0 | 171.0 ± 3.8 | 70.7 | 70.6 ± 0.6 | -5.1 | -5.1 ± 2.4 |
| 35 | H 1413+117 | 160.3 | 160.3 ± 0.6 | 170.3 | 170.4 ± 0.7 | 71.1 | 71.1 ± 0.4 | -2.6 | -2.6 ± 0.3 |
| 36 | HST 14176+5226 | 163.1 | 163.1 ± 0.5 | 179.5 | 179.6 ± 1.6 | 75.8 | 75.7 ± 1.1 | -5.5 | -5.6 ± 1.0 |
| 37 | HST 12531-2914 | 149.9 | 149.6 ± 2.2 | 175.0 | 175.5 ± 4.4 | 75.8 | 75.4 ± 2.4 | 4.7 | 4.1 ± 3.2 |
| 38 | HE 0435-1223 | 155.1 | 155.2 ± 0.3 | 176.8 | 176.7 ± 0.3 | 75.9 | 75.9 ± 0.3 | 0.6 | 0.6 ± 0.2 |
| 39 | SDSS 1011+0143 | 169.7 | 169.9 ± 0.9 | 176.4 | 176.6 ± 1.5 | 84.4 | 84.5 ± 1.2 | 1.7 | 1.6 ± 0.8 |
| 40 | SLACS J0946+100 | 182.9 | 182.9 ± 0.9 | 172.8 | 172.7 ± 1.1 | 88.6 | 88.6 ± 1.2 | 0.6 | 0.6 ± 0.8 |

MG 2016+112 [52, 53], B2045+265 [44], B 1933+503 [54], SLACS J2300+002, SLACS J1636+470, SLACS J1205+491 [55], SDSS J125107 [56], SDSS J1330+1810 [57], J 100140.12+020 [58], SDSS J1538+5817 [47], SDSS J002240 [45], SDSS J120602.09 [59], J 095930.94+023 [58], SDSS 1402+6321 [60], LSD Q0047-2808 [49], HE 1113-0641 [61], SLACS J0946+100 (outer ring) [62]

# Chapter 4

# Type II Lenses

## 4.1 Introduction

The field of multiple image gravitational lensing was born about 35 years ago with the discovery of Q0957+561 [15] and PG1115+08 [63], which were followed by discoveries of many more doubly and quadruply imaged quasars. The theoretical understanding of these systems grew up alongside the growing body of observations. The earliest works found that simple parametric forms for the mass distribution in the lens can account for the systems' observables [64], and that image properties, namely positions, shapes, time delays and flux ratios can be derived from the suitably defined lensing potential [65, 17].

It was also soon realized that strong lensing has degeneracies and invariants, and that these theoretical insights prove useful when lensing is used as a tool. For example, mass sheet degeneracy, and some other degeneracies where different

[0] This Chapter is submitted for publication to MNRAS

lenses reproduce exactly the same image observables have been well studied [66, 67, 68, 69], especially in relation to mass modeling, where degeneracies affect the conclusions about the mass profiles of lenses. The first lensing invariant discovered was the magnification invariant. It states that the sum of signed magnifications for all lensed images of any source within the caustic of a given lens is a constant. This constant can be the same for more than one lensing potential, and is often independent of the parameters characterizing the potential [70, 43]. [71] and [72] showed that image positions can also be used in forming invariants. Aside from their intrinsic theoretical value, the invariants allow us to rule out some lens models without even fitting the lens. To quote [72], "The major application of lensing invariants is to shortcut the modeling process."

Because observational uncertainties on the image observables are never zero, not only exact but also approximate degeneracies and invariants are important for the practical work. For example, [73] start with an exact invariance transformation that applies to axisymmetric lenses, and show that it survives in an approximate, but still useful form when applied to a wider range of lens models.

Our work in this Chapter is in the same vein: we study near invariants that provide useful insights without mass modeling, and have important consequences for mass substructure in lenses. Our analysis is of quads; it involves image positions only, and does not rely on magnifications.

The relative image locations of a quad are specified by six numbers, say, $(x, y)$ coordinates of any of the three images with respect to the 4th. Lens mass modeling—parametric or free-form—attempts to reproduce all six numbers at

once. In [39] and [2] (hereafter WW11) we started developing a new way of looking at quads, that considers only the three polar angular coordinates of quads, and disregards the three $r$ coordinates. We showed that information about the mass distribution of certain lens models contained in the azimuthal, or angular coordinates of images around the center of the lens is almost independent of that contained in the radial coordinates, and that the angular coordinates of images show approximate degeneracies. Specifically, if a lens with double mirror symmetry can reproduce the relative images angles of a quad, then all lenses with double mirror symmetry can reproduce the relative image angles of that quad, though for different locations of the (unobservable) source. Here we continue developing the theory of relative image angles of quads by extending it to lenses represented by purely or approximately elliptical mass profiles with external shear. The lenses in this general class of mass models are important to study because they fit observed quads well, and are common in parametric lens modeling.

Since we study a wide class of such lenses, and identify similarities, we are able to make conclusions that are independent of a specific lens model. Our analysis suggests that even though these common models are able to reproduce observed quads one at a time, they are unable to reproduce them *as a population*. Instead, substructured lenses or luminous or dark nearby perturbers are likely needed.

Because of their importance in the ΛCDM cosmological model [74, 75], substructure has been the focus of many recent papers. The main method employed for finding substructure uses flux ratios of close pairs or triples of images of quad lenses. In the absence of substructure clumps, i.e. when the potential is smooth, the magnifications of these images obey certain relations [65, 76]. Substructure

induces deviations from these relations, or anomalies [77, 78]. The substructure finding methods based on flux anomalies and image positions are complementary because the former are sensitive to small clumps located close to the images, while the latter are less easily perturbed and respond to larger clumps, $\gtrsim 10^9 - 10^{10} M_\odot$, located anywhere around the Einstein radius. The two methods also differ in other respects. Image fluxes are subject to different effects, depending on wavelength, like microlensing by stars in the optical and near infra-red, and propagation effects in the radio, and it is still unclear how major a role these factors play in the observed flux anomalies [79]. Image positions are affected only by relatively massive clumps.

This Chapter is organized as follows. In Section 4.2 we define our classification of lens types based on the caustics they produce. In Sections 4.3 and 4.4 we discuss the detailed properties of lenses that belong to what we call Type II lenses, which are the focus of this section. Readers interested primarily in substructure can skip directly to Section 4.5. Section 4.6 summarizes our findings.

## 4.2 Type II lens models

Parametric modeling, where parameters such as ellipticity, shear, position angle, etc. identify a lens model, is a commonly used method to theoretically represent gravitational lenses. Simple models obeying certain symmetries are used to fit observed properties of lens systems, such as image positions, time delays, and magnifications. The symmetries could be either in the isopotential or isodensity

contours of lenses with different radial density profiles. Examples of such axisymmetric models that are widely used are Elliptic Mass Distribution (EMD) and Elliptic Potential (EP)[41] with different radial profile such as Isothermal and NFW. The amount of constraining information that can be obtained from a given set of observed images is very limited, and inadequate to fully describe the details of the lensing mass. This means the lens equation is severely under constrained allowing it to admit multiple solutions. But any symmetry in how images are distributed on the lens plane is a direct consequence of the underlying symmetry of the lens and the source position in the source plane. For example, any axially symmetric lens, independent of the radial density profile, would give rise to an Einstein ring for a central source. Therefore categorizing and studying lenses that share sets of symmetries using parameters is a practical approach that does not contradict observational data.

In previous work by the authors (WW11) three classes of lenses were introduced. The classification is based on azimuthal symmetries of isopotential or isodensity contours of lenses, and is independent of the radial density profile. Lens models obeying twofold symmetry (symmetric about two orthogonal axes) in the lens plane were termed Type I lenses, and breaking this symmetry once resulted in Type II lenses. Type III encompassed all other models.

A more precise categorization, which we will adopt in this Chapter, can be achieved by using the symmetries of the diamond caustics. Type I lenses are those that give rise to caustics with twofold rotational symmetry[1] and double

[1] Objects with n-fold rotational symmetry look the same when rotated by $\frac{360}{n}$ degrees. Twofold symmetry is identical to inversion symmetry through the origin.

mirror symmetries, while Type II lenses are the ones that give rise to caustics obeying only twofold rotational symmetry. In this new definition of Type I and II we also limit ourselves to lenses with diamond caustics and exclude those that produce caustics with higher order catastrophes. Such constraint is justified for our analysis which aims to understand the population of observed lens systems. Higher order catastrophes can produce lenses with more than five images, which are not observed in galaxy lenses. Type III lenses include everything except Type I and Type II, for example, substructured lenses. This section examines Type II models in detail.

Elliptical potentials or mass distributions of arbitrary ellipticity and density profile have twofold and double mirror symmetries. By introducing external shear at a non-zero angle with respect to the ellipticity axes, the double mirror symmetry is broken giving rise to Type II lenses. In this section we look at Type IIs with power law and NFW density profiles. We identify a lens by three parameters: ellipticity, $\epsilon$, external shear, $\gamma$, and the angle, $\beta$, between shear and the ellipticity principal axis. By definition, $\beta$ lies between $0^\circ$ and $90^\circ$.

Our basic analysis method uses the relative angular distribution of the four images of quads[2] about the center of lens. This approach was introduced in [39] and refined in WW11. The method is statistical in nature in the sense that it works with quads as a class to draw conclusions about the mass distribution in galaxy hosts of quad lenses. We will show that properties related to quad image angles are approximately independent of the radial mass density profile of the

[2] Technically, quads are five image configuration with one of the images invisibly sitting near the very bright center of lenses. For all purposes of this thesis, the fifth central image is ignored.

lens, and that Type I and II lenses cannot account for the observed population of quads.

## 4.3 Power law potentials as examples of Type II

Type II lenses are a wide class. Our strategy is to study a few representative examples of Type IIs in detail, note their similarities and differences, and draw conclusions based on these. Our examples are chosen to be representative of the models used in the lensing literature and to resemble the real galaxy lenses. Furthermore, for computational ease, we use models whose lensing potentials are expressed by simple analytical functions.

Power law lensing potentials are one example that satisfy all the above criteria. They have a general form,

$$\phi(r,\theta) = br^{\alpha}\sqrt{1-\epsilon\cos(2\theta)} + \frac{\gamma}{2}r^2\cos(2[\theta-\beta]). \tag{4.1}$$

In the above expression $b$ is the normalization factor, $\epsilon$ is an ellipticity parameter (henceforth ellipticity)[3] , and $r$ is the sky-projected distance from the lens center. The second term is external shear of strength $\gamma$ oriented at an angle of $\beta$ relative to the ellipticity's principal axis. The exponent $\alpha$ in the first term is physically constrained to be between zero ($\alpha < 0$ implies decreasing total enclosed mass with increasing $r$), and two ($\alpha > 2$ implies that the density is increasing with $r$), but observations constrain it even further to be around 1 [49]. Theoretically, we can use any values of $\gamma$ as long as the lens gives rise to quads, whereas $\epsilon$ is limited

[3] Note that $\epsilon$ is related to the standard definition of ellipticity (1 - axes ratio) as $1-\frac{b}{a} = 1-\sqrt{\frac{1-\epsilon}{1+\epsilon}}$

to be between 0 and 1 by definition. In addition, $\epsilon$ and $\gamma$ are also restricted from above by the requirement that the corresponding isodensity contours are not peanut shaped, which happens, for example, for $\alpha \approx 1.2$ and $\epsilon \approx 0.25$, or $\alpha \approx 1$ and $\epsilon \approx 0.15$.

### 4.3.1 Singular Isothermal Elliptical Potential with External Shear (SIEP+shear)

In this section we use singular isothermal elliptical potential with external shear to demonstrate detailed properties of Type II lenses. SIEP+shear, given by eq. 4.1 with $\alpha = 1$, is chosen because it is the simplest form of power law potential that is semi-analytically treatable. Different combinations of $\epsilon$, $\gamma$ and $\beta$ give rise to different diamond caustics (based on orientation, elongation of cusps and curving of folds) but all obey the twofold rotational symmetry that identifies Type II lenses.

One interesting property of Type IIs concerns the isopotential contours. The main galaxy, i.e. first term in equation 4.1 with $\alpha = 1$ gives rise to contours all of which have the same ellipticity axis, but the addition of external shear results in slightly twisting isopotential contours, i.e. angular orientation of the principal axis of each contour of the total lens potential changes with radius. This is true of the contours in the first panel of Figure 4.1, but is hard to see because the degree of twisting is small.

We parametrize a given diamond caustic by angles formed by its diagonals and the ratio of the length of the diagonals. We do not consider the curvatures

of the folds, i.e. there could be two diamond caustics of the same diagonal ratios and angles but with different fold curvatures. In the case of Type I lenses, the caustic diagonals are perpendicular to each other while for Type II caustics, the diagonals form angles other than 90°; see the middle panel of Figure 4.1.

Another interesting property of SIEP+shear is that the singularity at the center is not a true critical point; mapping it to the source position using the lens equation gives rise to a set of points forming an oval which acts like an oval caustic, and is called a 'cut' [80]. Even though this set of points does not satisfy the common definition of a caustic, where the determinant of the Jacobian of the lens mapping is zero, it still acts like one; crossing the cut results in a change of image multiplicity.

Quads are formed when a source is within the diamond caustic and the cut. The angular distribution of the four images about the center of the lens can be uniquely represented by three relative angles $\theta_{ij}$ (the acute angle between image $i$ and image $j$), where image $i$ is the $i^{th}$ arriving image. Image ordering for synthetic lenses is always known. Images in observed quads can be correctly time ordered in most cases using image morphology [40].

In this section we use the same set of relative angles as in WW11: $\theta_{12}$, $\theta_{34}$, and $\theta_{23}$. A 3D space can now be formed using these angles, where a point in the space represents a single quad. Given a lens characterized by $(\epsilon, \gamma, \beta)$, one can generate a large number of quads arising from different source positions. The distribution of the corresponding points in the 3D angle space can be used as an alternative way of characterizing the lens[4] . Quads produced by Type I lenses lie on a slightly

[4] The code that generates the 3D plot is given in the Appendix

curved surface, which we called the Fundamental Surface of Quads (FSQ) with a peak at $(\theta_{12},\ \theta_{34},\ \theta_{23}) = (180°,\ 180°,\ 90°)$. Quads from all Type I lenses lie very close to the FSQ, making it a nearly invariant surface, and a useful reference.

On the other hand, quads arising from Type II lenses form two separate surfaces, each usually confined to two different portions in the 3D angle space separated by the FSQ. Based on the positions relative to the FSQ, the two surfaces are identified as upper or lower surface. Like the FSQ, each of these surfaces has two well defined edges which corresponds to $\theta_{12} = 180°$ and $\theta_{34} = 180°$. These two edges of each of the two surfaces meet to form two peaks, one above and one below the FSQ peak as shown in the left panel of Figure 4.2. Each surface sits at the farthest point relative to the FSQ at its peak, i.e. near $\theta_{23} \sim 90°$. The edges of the surfaces come closer to each other at lower values of angle $\theta_{23}$ while their middle parts stay farther apart (right panel of Figure 4.2). The two $\theta_{23}$ angles of the peaks of the two surfaces of an SIEP+shear lens (or any Type II lens) are supplementary angles (i.e. they add to 180°). We use the $\theta_{23}$ value of the peak quad of the upper of the two surfaces, $\theta_{23,p}$, as an index to parametrize the surfaces of a given lens in the 3D space.

### Potential, caustic and 3D angles space

As described above, Type II lenses can be characterized in three different spaces (Figure 4.1). The potential space, where $\epsilon$, $\gamma$ and $\beta$ parametrize the lens, the caustic space where the angles between caustic diagonals and the ratio between their lengths characterize the caustic, and the 3D angles space where $\theta_{23,p}$ value of the peak of the top surface is the characteristic parameter. Now, we describe

how the three spaces and their corresponding parameters are related.

**The central source.** The source at the center of the lens corresponds to the center of the diamond caustic and is mapped to two pairs of images with each image of a given pair having the same arrival time. We arbitrarily choose one of the first arrivals as image 1 and the other image 2. The same is done with images 3 and 4. The two images with the same arrival time sit at 180° of each other on the lens plane, therefore $\theta_{12} = \theta_{34} = 180°$. For Type I's, the line connecting opposite images (those with the same arrival time) are orthogonal, so $\theta_{23} = 90°$, but this is not the case for Type IIs, where $\theta_{23}$ is either acute or obtuse, depending on the choice of ordering, but the two possibilities are always supplementary angles. The maximum angular separation of images 2 and 3 is attained when the source is at the center of the caustic, and this separation decreases as the source moves radially out from the center. In the 3D angles space, the central source corresponds to two degenerate quads, each located at the peak of each of the two surfaces, at $(180°, 180°, \theta_{23,p})$, and $(180°, 180°, 180° - \theta_{23,p})$.

SIEP+shear has an interesting property connecting the caustic and the images arising from the central source. The two supplementary angles formed by the diagonals of a diamond caustic are same as the $\theta_{23,p}$ angles of the 3D space. (In addition, the ratio of the caustic diagonal lengths is the same as the ratio of the radial positions of images 2 and 3 from the center of the lens, but we do not consider the image distance ratios, so we will not explore this relation any further.)

**Sources on the caustic diagonals.** The images of sources on the diagonals of the caustic form the two outer edges of the sheets, $(180°, \theta_{34}, \theta_{23})$ and

$(\theta_{12}, 180^\circ, \theta_{23})$. Just like the central source, sources on the diagonals results in degenerate images in terms of arrival time. It is important to note that this degeneracy is only for source positions along the diagonals. All other sources within the caustic are mapped to quads that form the body of the 3D surfaces, with each image arriving at distinctly different time from the rest. Therefore, the two sheets are completely different and not a result of ordering choice of the equally arriving images.

**The rest of the sources.** The rest of the two sheets in the 3D angles space comprises quads arising from sources within the body of the diamond caustic. As shown in the top panels of Figure 4.3 there is a bifurcation about the diagonal of the caustic. Continuously crossing a diagonal, i.e. moving from one quadrant of the diamond caustics to another (for example, from the black region to the yellow, lighter shade, one) results in a jump between the two sheets of the 3D angles space. Sources on straight lines of constant source position angle in the source plane (various colored lines in the caustic shown in the lower left panel of Figure 4.3) result in quads that form non-crossing monotonic, but not necessarily straight curves on the 3D surfaces (lower right panel).

**The inversion symmetry of Type II lenses.** The twofold (inversion) symmetry of the Type II lens diamond caustic also applies to the potential, and is further reflected in the 3D angles space. Source positions from the two opposite quadrants of the caustic generate quads that form one of the sheets. The remaining two quadrants produce the second sheet. In Figure 4.3 the two yellow, lighter shade, (black) quadrants of the caustic shown in the upper left panel generate the yellow, lighter shade, (black) surface in the 3D angles space shown in the upper

right panel. So the inversion symmetry reduces the number of distinct caustic quadrants from four to two. *The existence of the two surfaces in the 3D space of relative image angles is the most important characteristic of Type II lenses.*

Note that the properties described in this subsection are not unique to SIEP+shear lenses, but are common to all Type IIs. The inversion symmetry of Type II, which is their defining property, naturally predicts the two surfaces in the 3D angles space. We have tested the existence of the two sheets on many more lenses than are presented here (for example, several Sersic type models), and have confirmed the qualitative behavior of the two sheets. At large $\theta_{23}$ the two surfaces are always found on the opposite sides of the FSQ in the 3D angles space (left panel of Figure 4.2), and the separation of the two peaks depends on how much the lens potential deviates from that of Type I. At small $\theta_{23}$ the edges of the two sheets approach each other and the FSQ (right panel of Figure 4.2).

**Near degeneracies of lens models with different sets of ($\epsilon$, $\gamma$, $\beta$)**

As mentioned earlier, we chose to parametrize the distribution of quads in the 3D angles space by $\theta_{23,p}$, the angle between the 2nd and 3rd arriving images of the source located at the center of the lens. The full distribution of quads from a single lens are the two surfaces or sheets (right panel of Figure 4.1, or Figure 4.2). One may ask if it is adequate to represent the surfaces with just a single point, $\theta_{23,p}$?

Figure 4.4 shows contour surfaces of constant $\theta_{23,p}$ in $\gamma$ vs. $\epsilon$ vs. $\beta$ space. Any two points on a given surface represent two different lenses in the potential space, each characterized by a different set of ($\epsilon,\ \gamma,\ \beta$), but sharing the same $\theta_{23,p}$. The

two contour surfaces shown have $\theta_{23,p} = 91^\circ$ and $\theta_{23,p} = 92^\circ$. In the caustic space these lenses have some commonalities: the diagonals of the caustics intersect at the same angle, since, as previously discussed, these angles are the same as $\theta_{23,p}$. However the folds and cusps of these caustics look different.

Having matched different lenses based on their $\theta_{23,p}$ value, we would like to see how the corresponding surfaces in the 3D angle space compare. We carry out the comparison in two steps: first we compare the edges and then the bodies of the surfaces. To carry out these comparisons we picked four different lens models, each belonging to the same $\theta_{23,p} = 92^\circ$ contour. We identify each lens as L($\epsilon,\ \gamma,\ \beta,\ \theta_{23,p}$). Table 3.1 summarizes these lenses.

For the first comparison, the $(180^\circ, \theta_{34}, \theta_{23})$ edge of the lower of the two 3D surfaces for lenses A-D are plotted in Figure 4.5. Visually they seem to form the same line. But in order to quantify any difference between the edges, we compare fit equations of the lines. The fit equations for Lenses A-D are

$$\begin{aligned} \theta_{23} &= 0.48617\theta_{34} + 0.25271 \\ \theta_{23} &= 0.48617\theta_{34} + 0.252017 \\ \theta_{23} &= 0.48621\theta_{34} + 0.247357 \\ \theta_{23} &= 0.48627\theta_{34} + 0.240303 \end{aligned} \tag{4.2}$$

respectively, and the angles are expressed in degrees. The average of the median observational error of the three relative angles is $\sim 0.8^\circ$ (WW11) which is at least two orders of magnitude greater than the difference between the intercepts of the above equations. Similarly, the median observational error of the slope $\theta_{23}/\theta_{34}$ is $\sim$ 0.006 which is again two orders of magnitude greater than the difference

between the slopes of the four equations above. A corresponding comparison for the other edge of the 3D surface, the $(\theta_{12}, 180°, \theta_{23})$, yields similar results. Therefore, the difference between the edges of these four, and presumably other different SIEP+shear lenses in the 3D space is negligible for all practical and observational purposes.

For the second comparison we generate two sets of random source positions on one of the two surfaces of each lens. The quads from the first set are used to obtain an interpolation fit equation, which is then compared to the quads of the second set. This is our calibration, or cross-validation procedure. The comparison is done with the root mean square of errors, RMSE. The cross-validation for Lens A yields RMSE of 0.005°. The RMSE's of Lenses B-D, when compared to the fit equation of Lens A are 0.011°, 0.029°, and 0.017°, respectively (see Table 1). A visual indication of how close these surfaces look is provided by Figure 4.6, which plots a certain projection of the 3D angles space (explained in detail in Section 4.5) for Lenses A-D. The largest deviation is for Lens C, represented by (green) diamond symbols, which extend lower along the vertical axis by about 0.1 degree compared to the other three lenses. In general, lenses with largest deviations from the rest of their family members are those with larger ratios of $\epsilon/\gamma$.

The RMSE values and Figure 4.6 show that the surfaces are not mathematically identical, but because the deviations between lenses sharing the same $\theta_{23,p}$ are smaller than the typical observational error (even for Lens C), observationally speaking these four SIEP+shear lenses of different lens parameters ($\epsilon,\ \gamma,\ \beta$) are degenerate in the 3D angles space, i.e. in terms of the relative image angles. In

other words, if a lens model described by ($\epsilon_1,\ \gamma_1,\ \beta_1$) is found to fit the relative angles of an observed quad, then any other lens characterized by the same $\theta_{23,p}$, but a different set ($\epsilon_2,\ \gamma_2,\ \beta_2$) will also be able to reproduce the image angles, though for a different location of the source.

So the answer to the question raised at the top of this section is *yes*, a single point in the 3D angles space, $\theta_{23,p}$, adequately represents the rest of the surfaces.

We note an interesting consequence of the degeneracy described above. Taking a $\beta$=const two dimensional slice through the surfaces in Figure 4.4 we get contours plotted in Figure 4.7. These contours are symmetric about $\epsilon = \gamma$ line, which implies that $\epsilon$ and $\gamma$ are interchangeable. This is unexpected because this symmetry is not at all obvious from the equation of the lens potential, eq. 4.1 with $\alpha = 1$. Later we will see that this symmetry applies to other potentials if the isopotential contours are purely elliptical (as defined in Section 4.3.2).

Note that here we do not consider image distances from the lens center; two lenses degenerate in image angles need not be degenerate in image distances.

### 4.3.2 Non-isothermal Elliptical Potentials with External Shear

As discussed when introducing the general power law potential, eq. 4.1, $\alpha$ is observationally constrained to be $\sim 1$ [49]. Therefore, we extend our discussion of Type II lenses only somewhat beyond this value; we use $\alpha = 0.9$ and $\alpha = 1.2$. We expand $\alpha$ up to 1.2 so that we can explore lenses with higher values of ellipticity. Going beyond these limits results in the mass density contours becoming peanut

shaped even for moderate values of ellipticity $\epsilon$. For $\alpha = 1.2$ the two sheets in the 3D space starts crossing for small values of $\theta_{23}$ when the ratio $\epsilon/\gamma \gtrsim 1$.

We note that the way $\alpha$ is introduced in eq. 4.1 creates lenses whose isopotential contours due to the main galaxy are not exactly elliptical; we call these hybrid potentials. The pure elliptical potentials are obtained by raising what we call the elliptical radius, $r\sqrt{1-\epsilon\cos 2\theta}$, to the power of $\alpha$ instead of raising just $r$. But the angular distribution of quads generated by pure elliptical potentials are not distinctly different from that of SIEP+shear, therefore our discussion in this section focuses on hybrid potentials.

The $\gamma$ vs. $\epsilon$ contour is not symmetric about $\gamma = \epsilon$ line, with the contours rotated clockwise for $\alpha = 0.9$ and counter clockwise for $\alpha = 1.2$; see Figure 4.5. But for pure elliptical lenses defined above, the contours remain symmetric independent of $\alpha$ and this symmetry extends to NFW profiles discussed in the next section, as already alluded to at the end of Section 4.3.1.

We would like to know if the degeneracy property of SIEP+shear (Section 4.3.1) applies to non-isothermal lenses, i.e. if these lenses can be adequately characterized by just $\theta_{23,p}$. For that purpose we generate quad distributions for Lenses F - I; see Table 3.1. Lens F and G have $\alpha = 1.2$, while H and I have $\alpha = 0.9$ and all share the same peak of $\theta_{23,p} = 93°$. We use the second of the two tests introduced in Section 4.3.1. We find fit equations for one of the two surfaces of Lenses F and H, and compared these to the actual surfaces of Lenses G and I.

The cross-validation RMSE for Lenses F and H are 0.013° and 0.003°. The RMSE for Lens I as predicted by H is 0.264°. The RMSE for Lens G as predicted by F is 0.551°. However, the high $\epsilon$ to $\gamma$ ratio of Lens F ($\epsilon/\gamma = 4.5$) results in

its two surfaces in 3D angles space crossing each other, which makes it hard to separate out a single surface and find a fit equation for it. Therefore the latter value can be compared only approximately to other RMSE values.

This comparison of different lenses within the same family (F vs. G and H vs. I) shows that non-isothermal hybrid potential lenses sharing the same peak $\theta_{23,p}$ are approximately degenerate in the 3D angles space (all RMSEs quoted above are smaller than observational uncertainty), but are not as similar to each other as those within the SIEP+shear family.

We note, however, that this comparison might be affected by our numerical method; SIEP+shear potential is simple enough to be amenable to semi-analytical calculations, whereas non-isothermal hybrid potentials require fully numerical computations, and there are two places where numerical errors can creep in: (i) when selecting $(\epsilon,\ \gamma,\ \beta)$ sets from the same $\theta_{23,p}$ contour, and (ii) when doing forward lensing of sources to produce images and measure their polar angles. These numerical errors could contribute to the differences in the 3D surfaces. In the next section, where these errors are also an issue, we carry out a test to assess the error arising from (i).

As with isothermal lenses, the models that differ the most from the rest of the family are those with larger $\epsilon/\gamma$ ratios. For $\alpha = 1.2$ larger $\epsilon/\gamma$ ratio also make the two surfaces in the 3D angle space cross the FSQ and each other. Nevertheless, the differences quoted above are at most of the order of observational errors. Therefore observations based on the relative image angles of quads can not discriminate between any of the lenses within the family given by eq. 4.1, as long as $\epsilon/\gamma \lesssim 2 - 2.5$.

## 4.4 Non Power law potentials as examples of Type II

In this section we broaden our exploration of Type II lenses to include models with non power law density profiles. We chose NFW radial density profile [81], which has an analytical form for its lensing potential [82]. Though the central density profiles of lensing galaxies are significantly affected by baryons and so typically have steeper than NFW slopes, we use this profile to explore how non power law profiles behave as Type II lenses. In order to make a Type II lens with NFW radial density profile we introduce external shear and ellipticity to the potential,

$$\phi(r,\theta) = b\left(\ln^2\frac{r}{2} - \frac{1}{4}\ln^2\frac{1+\sqrt{1-r^2}}{1-\sqrt{1-r^2}}\right) + \frac{\gamma}{2}r^2\cos(2[\theta-\beta]) \tag{4.3}$$

where $r = x\sqrt{1-\epsilon\cos(2\theta)}/r_s$, $x$ is the polar radius in the lens plane, $r_s$ is the scale factor of NFW density profile, and $b$ is a normalization that is a function of $r_s$ and the characteristic density. The rest of the variables are as defined in previous sections. This potential is defined for $r < 1$, i.e for $x < r_s$.

The diamond caustic of this potential has the symmetry of Type II lenses, and gives rise to two surfaces in the 3D space of relative image angles of quads. As shown in upper right panel of Figure 4.7, $\gamma$ vs. $\epsilon$ contour map of constant $\theta_{23,p}$ is symmetric with respect to $\gamma = \epsilon$ line. Lenses J and K in Table 3.1 are two different lenses in potential space whose two surfaces each have the same peak, $\theta_{23,p}$, in the 3D angles space. To check if these surfaces of two different lenses are degenerate in 3D angles space, the second test of Section 4.3.1 is implemented. A cross-validation RMSE for Lens J is 0.006° while the RMSE of Lens K as predicted

by Lens J is 0.181°.

Again, numerical errors could contribute to the difference between the 3D angles space surfaces of these two lenses. To show that this is likely to be the case we made use of the symmetry with respect to the $\gamma = \epsilon$ line mentioned in the previous paragraph. We generated 3D angle space surfaces for sets of lenses related by this symmetry: Lenses K and KK, and J and JJ in Table 1 are two examples. All four lenses share the same $\theta_{23,p} = 93°$, but the $\epsilon$ and $\gamma$ parameters of J and K were picked from numerically generated output, whereas those of K and KK (J and JJ) were obtained by swapping $\epsilon$ and $\gamma$ values, which yields exact $\epsilon$ and $\gamma$ parameters. The RMSE from the comparison of Lenses J and JJ (K and KK) yields 0.007° (0.036°), values which are considerably smaller that 0.181° quoted in the previous paragraph.

Whatever the source of the discrepancy between lenses such as J and K, the difference is still less than the observational errors, so elliptical NFW+shear lenses with the same $\theta_{23,p}$ are nearly degenerate in terms of image relative angles.

## 4.5 Implications for the Observed Quads and Type III lenses

In this section we rely on the basic property of Type II lenses, namely that the quads of each lens generate two distinct surfaces in the 3D space of image relative angles, such as shown in Figure 4.2 (Section 4.3.1), and that the two sheets are qualitatively similar for all Type II lenses that are suitable as models for observed

quads. Our analysis differs significantly from lens modeling. Unlike lens mass modeling, parametric or free-form, which is done with one lens system at a time, we study the population properties of quads, and compare them to the generic properties of Type II lenses. This is why we refer to our method as model-free analysis of quads.

To do that one needs to explore a wide range of Type II lens models that are used in the literature to model quads. This task is made easier by the results of Sections 4.3-4.4, where we explored detailed properties of three different representative classes of parametric models as examples of Type II lenses, and showed that lenses within the same class, like SIEP+shear, or elliptical NFW+shear exhibit approximate degeneracies, in the sense that lenses with the same angle $\theta_{23,p}$ have very similar distribution of quad relative angles in the 3D angle space.

Furthermore, this degeneracy extends to lenses with different radial density profiles sharing the same peak, $\theta_{23,p}$, as long as the ratio $\epsilon/\gamma$ is smaller than $2 - 2.5$. To show this we introduce another lens, Lens E (SIEP+shear), which has the same $\theta_{23,p}$ as Lenses F - K. Interpolation fit for Lens E gives a cross-validation RMSE=0.003 degrees. Then, fitting Lenses G (hybrid with $\alpha = 1.2$), H (hybrid with $\alpha = 0.9$), and J (NFW) give RMSE of 0.146, 0.011, and 0.085 degrees, respectively (Table 1), which are all smaller or of the order of observational uncertainty. This is an important result: most Type II lenses which have the same angle between 2nd and 3rd arriving images of the central source are nearly degenerate in terms of their image angles, for all sources.

The existence of this degeneracy, even if approximate, reduces the number of lens models one has to consider. It follows that we have to consider only a set of

lenses with different $\theta_{23,p}$, and any density profile (power law or curved in log-log space, like NFW, with the projected density slope not too different from 1 and any set of ($\epsilon,\ \gamma,\ \beta$), as long as $\epsilon/\gamma \lesssim 2 - 2.5$. The restrictions on $\alpha$ and $\epsilon$ are because the degeneracies break down outside of the specified ranges. However, almost all of the lens models used to fit observed quad systems belong to the set of degenerate lenses. It is also important to stress that the general shape of the surfaces formed by quads in the 3D angles space is the same for all Type II lenses, even if they are not degenerate.

Now we are ready to compare Type II lenses with the observed quad population. We will work in two dimensions instead of the three dimensions of the 3D angles space. We use the FSQ as a reference surface, and plot the vertical "distance" between a quad in the 3D relative angles space and the FSQ, called $\Delta\theta_{23}$, versus $\theta_{23}$. This plane is shown in Figure 4.8, together with the quads data originally presented in WW11. FSQ in this plot is the $\Delta\theta_{23} = 0$ line. Using this same diagnostic tool, Type I lenses were shown to be inconsistent with the observed quad population (WW11). Specifically, the deviation of even extreme Type I lens models from the FSQ is not enough to account for the wide spread of observed quads in $\Delta\theta_{23}$ vs. $\theta_{23}$ plane, especially at the lower values of $\theta_{23}$.

Type II lenses can correct for the deficiencies of Type Is in reproducing the data. As discussed in Section 4.3.1, the two surfaces of Type II lenses deviate from FSQ, especially as the values of ellipticity and external shear are increased. The gray distributions in Figure 4.8 represent Type II lenses with $\theta_{23,p}$ selected to approximately span the observed quads. This spread might seem to imply that Type Is and Type IIs—the most commonly used parametric lens models—taken

together, can adequately model observed quads. But this is not so, as explained below.

As the values of ellipticity $\epsilon$ and shear $\gamma$ for model Type II lenses are increased to account for the observed quads at lower $\theta_{23}$, the gap between the peaks of the two surfaces, near large $\theta_{23}$, grows. These portions of the two surfaces have $\Delta\theta_{23}$ larger than $\pm$ few degrees, and hence predict the existence of many quads ($\sim 1/3$ of quads should have $\theta_{23} > 60^\circ$) where no observed quads are found (see Figure 4.8). Instead, observed quads with $\theta_{23} \sim 90^\circ$ congregate close to FSQ. Therefore, even if Type II lenses are able to alleviate the incompleteness of Type Is near small $\theta_{23}$, they introduce a more serious problem because they predict the existence of quads at large $\theta_{23}$ and $\Delta\theta_{23}$ of at least a few degrees.

Since the sample of quads we use does not represent a homogeneous sample, one may wonder if selection biases are responsible for the distribution of observed quads in the 3D angle space and hence in the $\Delta\theta_{23}$ vs. $\theta_{23}$ plane. To see that this is not the case let us recall how angle $\theta_{23}$ of a quad is related to the source's location within the caustic. Quads with large $\theta_{23}$ originate from the central regions of caustics, while those with small $\theta_{23}$, from the outer regions, adjacent to the folds and cusps. The distribution of Type I and II model lenses in the $\Delta\theta_{23}$ vs. $\theta_{23}$ plane would imply that the observed quads at large $\theta_{23}$ result from the central caustic regions of Type I lenses, while the quads at small $\theta_{23}$ arise from the outer caustic regions of Type II lenses. It would be hard for a selection bias to accomplish that. For example, magnification bias would bias against quads whose sources are located closer to caustic center. However, this bias could not distinguish between Type I and Type II caustics, which is what would be needed to explain

the distribution seen in Figure 4.8.

Furthermore, in order to reproduce quads at small $\theta_{23}$ Type II lenses would need to have high values of ellipticity and shear. For example, the full SLACS lens samples were fit with SIE mass profiles plus external shear model with median (maximum) values of $\gamma$ and $\epsilon$ of 0.05(0.27) and 0.21 (0.49), respectively [83], and the corresponding values from [84] for 14 quads are 0.12 (0.33) and 0.20 (0.49). The higher end of these parameter ranges appear to be larger than what should be expected in a realistic lensing case. Using monte carlo simulation and considering the effects of environment [85] have found the typical value of total shear to be 0.08 with highest value of 0.17, and [86] calculated a typical value for shear of 0.03.[5] Similar results were obtained by [87] and [88]. These works imply that there might be a problem with Type II lenses as models for observed quads.

This leaves us with Type III lenses, for example substructured lenses. A preliminary analysis gives promising results. As depicted in Figure 4.9, a better match to the distribution of quads in the $\Delta\theta_{23}$ vs. $\theta_{23}$ plane is achieved with the introduction of substructure in the main lens. By increasing the clumpiness of the lens, the gaps in the peak region, near large $\theta_{23}$, of the two surfaces of quads decreased significantly and looks more like the observational data. Too much clumpiness could lead to higher order catastrophes in the caustic which would result in observationally unsupported systems with higher image multiplicities. In the examples used in Figure 4.9 this is not a concern since even the clumpiest of the two substructured lenses (bottom row) produce more than five images for less than 1% of the total sources.

[5] Note that these ellipticity values refer to mass, so cannot be compared directly to our $\epsilon$.

Figure 4.10 shows that one does not need to use a highly substructured lens to reproduce the population distribution of observed quads. Here we start with a substructure-less Type I lens (top row) that gives rise to quads which are closely packed on the horizontal axis, i.e. the FSQ, failing to match the spread of observed quads. The introduction of substructure (bottom left) does not perturb the shape of the outer isodensity contours, but the resulting distribution of quads is dispersed in the $\Delta\theta_{23}$ vs. $\theta_{23}$ plane in the same fashion as the observed quads (bottom right).

This is just a limited foray into Type III lenses. The conclusion of this Section is that Type II lenses cannot reproduce the distribution of image angles of observed quads, and that possibly substuctured lenses, or additional nearby perturber galaxies are needed. We leave quantitative work on these lenses, and detained comparison with the observed quad distribution for future work.

## 4.6 Conclusions

In this Chapter we presented a technique to explore the properties of quadruple image gravitational lens systems. In general, the relative distribution of quad's four images about the center of a lens can be fully described in 6D space of three relative angles and three relative radial distances in the lens plane. Our technique uses only the 3D subspace of relative angles which is orthogonal to the remaining 3D subspace of relative distances.

We classify lenses into three main categories based on whether they obey twofold and double mirror symmetries. The caustics of Type I lenses fulfills both symmetries, those of Type II obey only the twofold symmetries while the caustics

of Type IIIs obey neither. In this Chapter we focused on Type II lenses. Our main working space is the 3D space spanned by the three relative image angles of a quad, $\theta_{12}$, $\theta_{23}$, and $\theta_{34}$. One of our main conclusions is that this space is a useful tool in studying quad lenses. We showed how the distribution of the three angles of a given lens relates to its lensing potential and the caustic. The two fold symmetry of the Type II lens caustic is reflected in the fact that in the 3D angle space the distribution of the relative angles is always confined to two surfaces (Figure 4.2). This is the defining feature of Type II lenses.

Of the three potentials we studied the closest quantitative connections between the lens potential, caustic and 3D angle space are exhibited by the SIEP+shear potential (eq. 4.1 with $\alpha = 1$). The angle between the second and third arriving images of the source located at the center of the lens, $\theta_{23,p}$ is equal to the angle between the caustic diagonals. (Though we do not study the images distances from lens center here, we note that the distance ratio of these two images is equal to the ratio of the two caustic diagonals.) SIEP+shear lenses that have the same angle $\theta_{23,p}$ have nearly the same distributions of quads in the 3D angle space, implying that $\theta_{23,p}$ is sufficient to specify the shape of the surfaces of all these lenses, and that these surfaces are degenerate. Other lenses also show close similarity between lenses of the same $\theta_{23,p}$, but not as close as for SIEP+shear. The similarity extended to lenses of different radial density profiles: quads of Type II lenses with ellipticities $\epsilon/\gamma \lesssim 2-2.5$ that have the same $\theta_{23,p}$ share approximately the same two surfaces in the 3D angles space.

The commonalities in the distribution of quads in the 3D angle space of all

Type IIs (the general shape and location of the two surfaces), and the near degeneracies described above allow us to draw conclusions about Type II lenses as a class. We call this approach model-free because it applies to a wide range of models. We conclude that, even though Type II lenses can successfully model individual quad lenses, they cannot reproduce the relative image angle distribution of the population of the observed quads.

We present two examples of Type III substructured lenses that have distributions of relative image angles that are generally consistent with the observed distribution. These examples are not meant to be a close match to observations. Future work will need to look at different types of substructure, as well as luminous and dark secondary perturber galaxies more carefully to ascertain what type and amount of substructure is necessary to fit the observed quad population. Finally, we note that the substructure mass clumps one would need to explain image angles are likely to be much larger in mass and extent compared to those thought to be responsible for the flux ratio anomalies of quads.

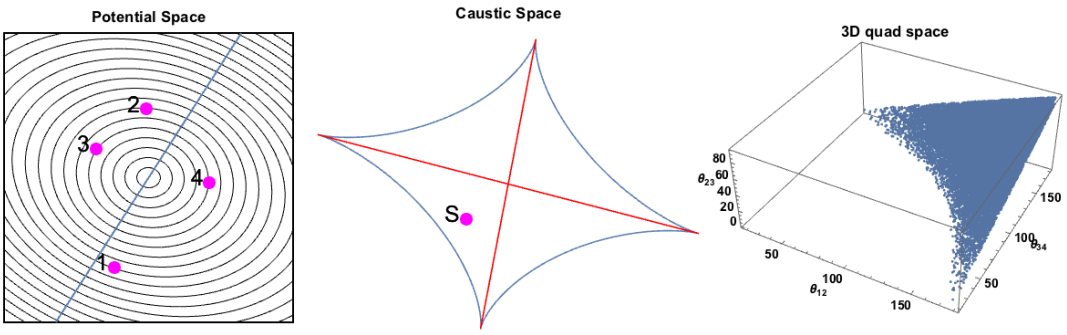


Figure 4.1: Lens Parametrization in three types of spaces: *Left:* Potential space. A Type II elliptical lens potential contours with external shear oriented along the line (inclined, and going through the center). The four images are numbered based on their arrival time *Middle:* Caustic space, parametrized by the ratio of its diagonals (red lines) and the angle they make at their crossing. **S** is the source that gives rise to the images shown in the left panel. *Left:* 3D space of quad relative image angles: three dimensional space formed by the three relative angles $\theta_{12}$, $\theta_{34}$ and $\theta_{23}$. Each point in this space represents a quad. The surfaces are generated by images of many randomly distributed sources within the diamond caustic and the cut.

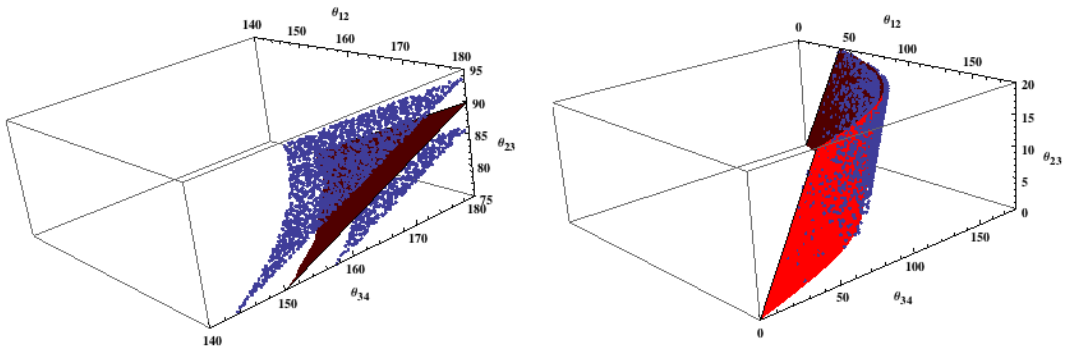


Figure 4.2: 3D angles space: Type II lenses produces quads that form two sheets on either side of the FSQ (the smooth dark, bright red, surface). Quads belonging to the Type II lens are represented by the, light blue, dots. *Left*: The top portion, $\theta_{23} > 75°$, of the 3D space and the surfaces. The peak of the FSQ is at $\theta_{23,p} = 90°$. The top peaks of the two surfaces of Type II lens are at $\theta_{23,p} \sim 94°$, and $\theta_{23,p} \sim 86°$. *Right*: The lower portion of the same 3D space, for $\theta_{23} < 20°$

.

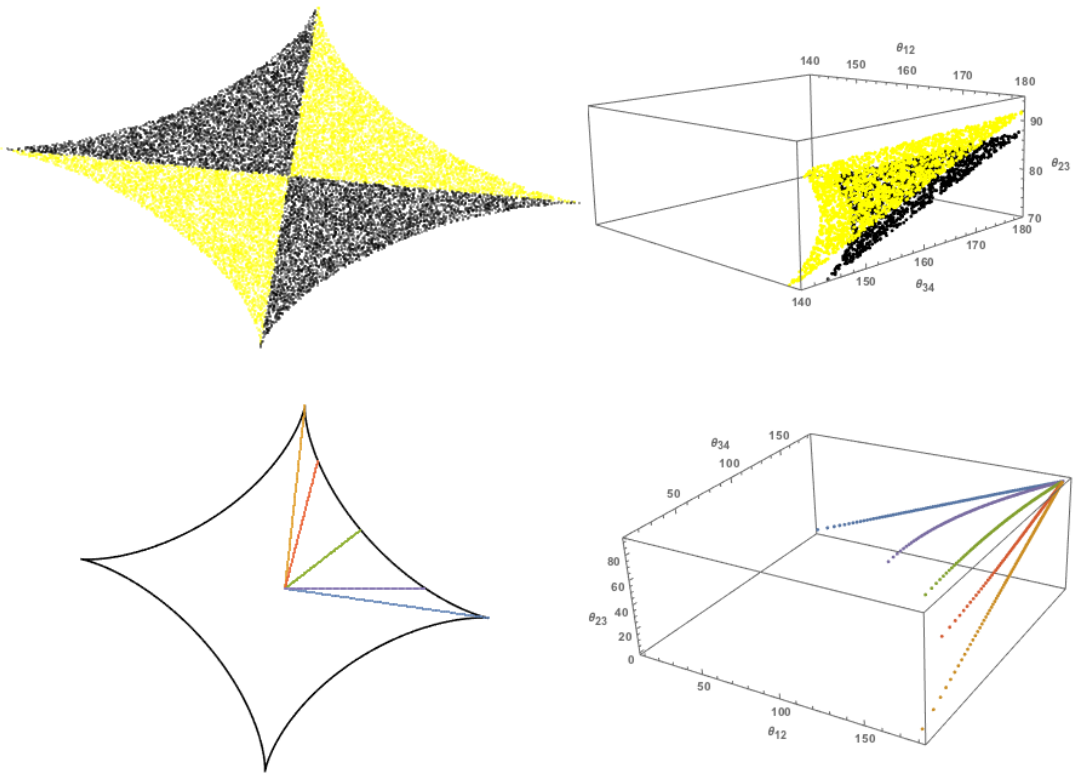


Figure 4.3: Mapping of the caustic space to the 3D space of relative image angles. *Top*: Each pair of opposite quadrants of the diamond caustic (for example, the two black quadrants) map into one of the two surfaces in the 3D space (black). This is a reflection of the twofold symmetry of Type II lenses. *Bottom*: Sources along constant position angle in the caustic plane (various colored lines) are mapped to non-crossing curves in the 3D angles space (similarly colored lines).

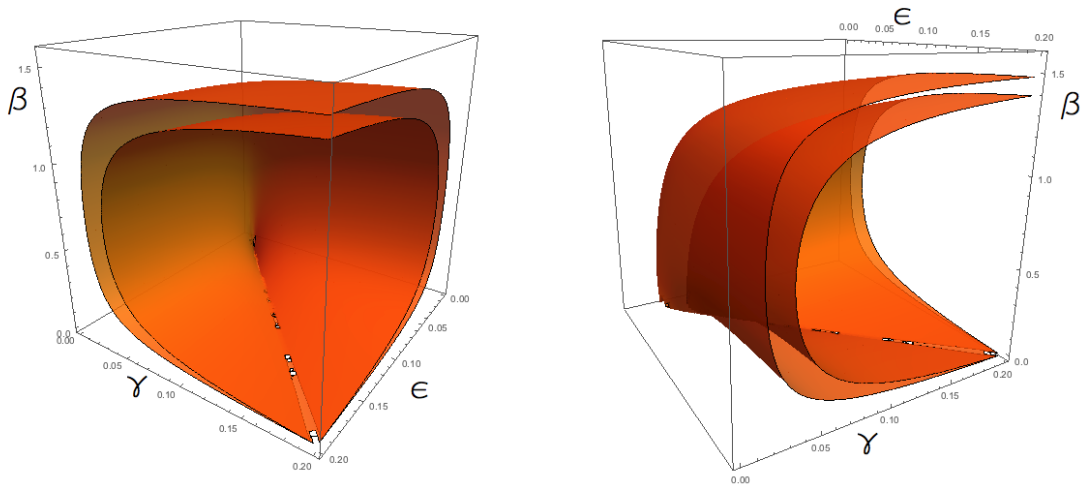


Figure 4.4: Contour surfaces of constant $\theta_{23,p}$ for SIEP+shear lens in $\gamma$ vs. $\epsilon$ vs. $\beta$ space. $\beta$ is in radians. The outer (inner) surface is for $\theta_{23,p} = 91°$ ($\theta_{23,p} = 92°$). The jagged line corresponding to $\beta = 0$ and $\gamma = \epsilon$ is the result of no quads being formed for those parameters. Two orientations of the same space are shown.

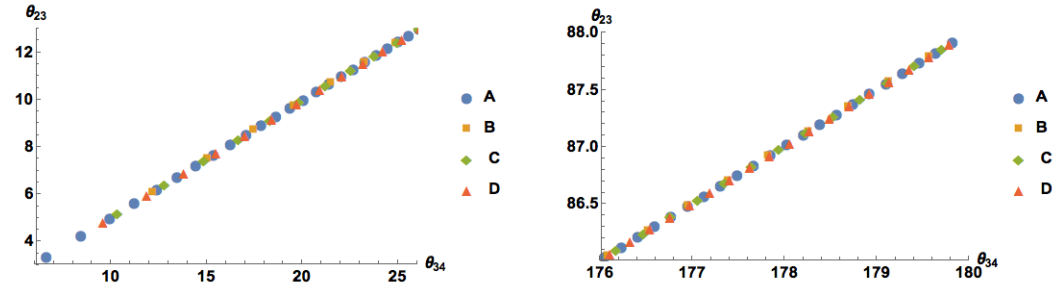


Figure 4.5: The $\theta_{12} = 180°$ edge of the lower of the two surfaces, in the 3D space of relative angles, for four SIEP+shear lenses sharing the same peak $\theta_{23,p}$. *Left:* Bottom end of the edge. *Right:* Top end of the edge. The parameters of the four lenses A-D are given in Table 1.

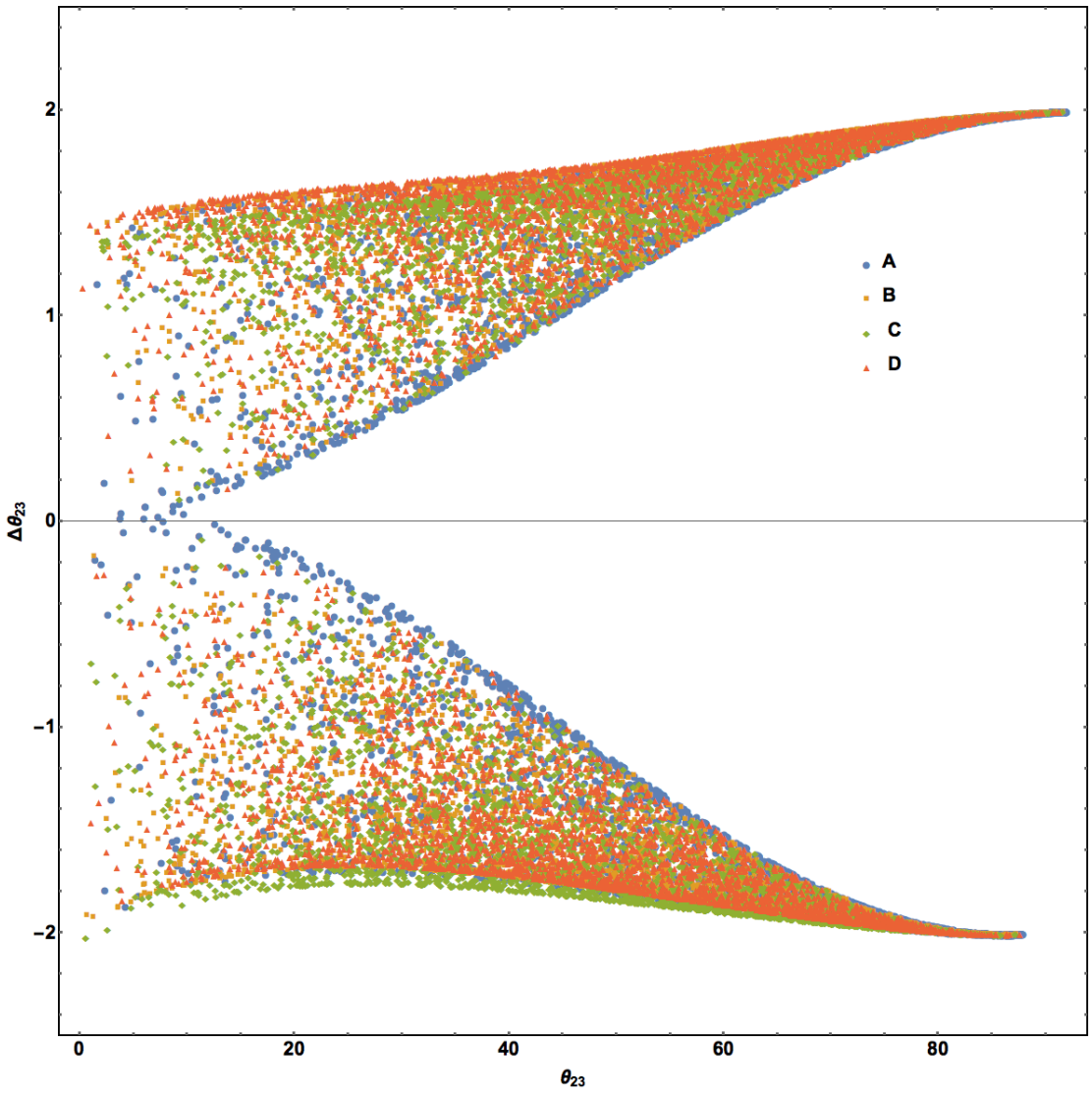


Figure 4.6: Projection of Lenses A-D with parameters as given in Table 3.1 . Lens C, diamond (green), slightly deviate from the other three lenses by sagging at the folds.

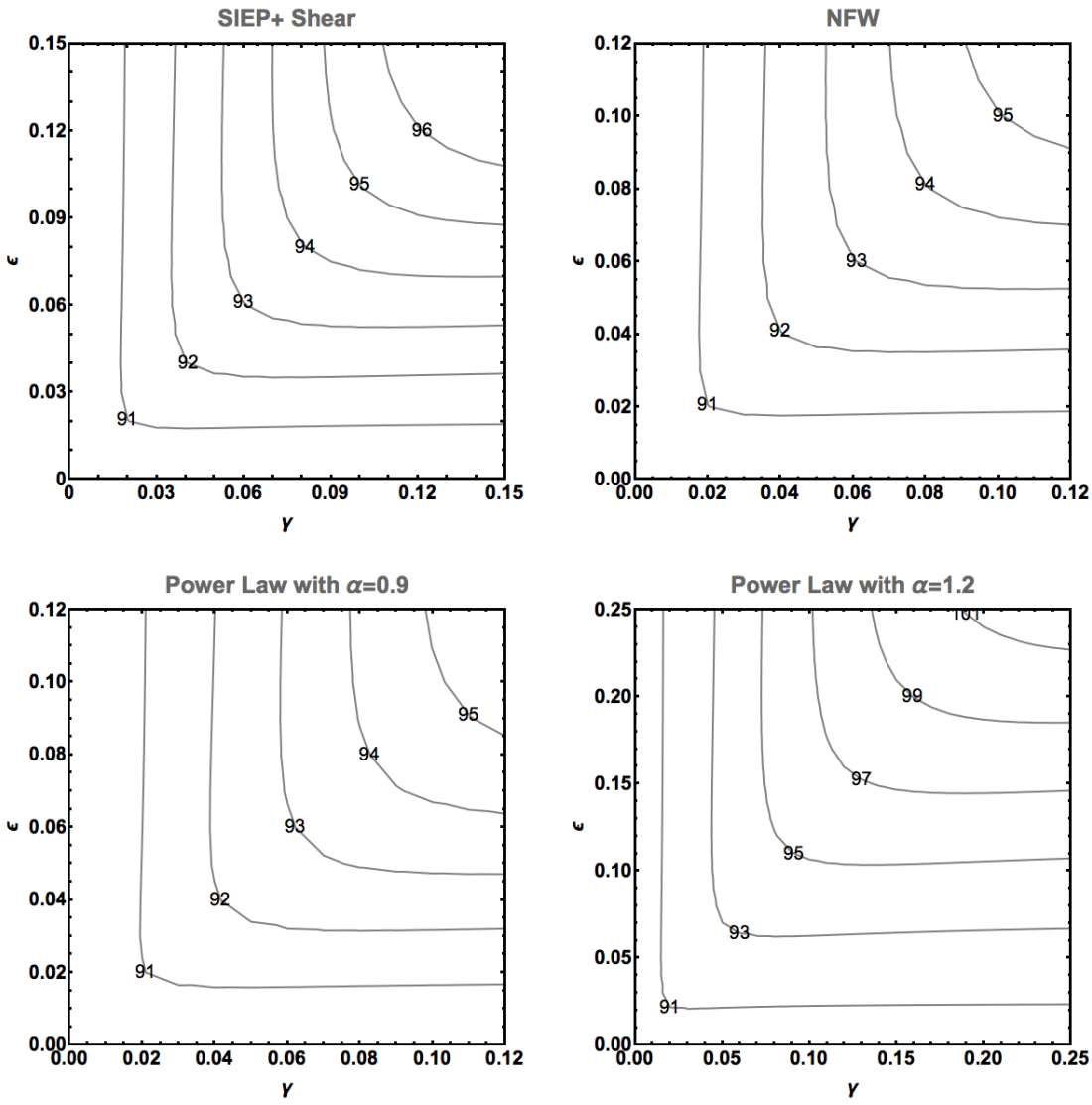


Figure 4.7: Contours of constant $\theta_{23,p}$ in $\gamma$ vs. $\epsilon$ plane for lenses of four different radial density profiles. The contours are labeled by $\theta_{23,p}$. For SIEP+shear (*Top left*) and NFW (*Top right*) lenses the contour lines are symmetric about $\gamma = \epsilon$ line. For hybrid power law potentials the contours are rotated, as compared to that of SIEP+shear, clockwise for $\alpha < 1$ (*Bottom left*) and counterclockwise for $\alpha > 1$ (*Bottom right*).

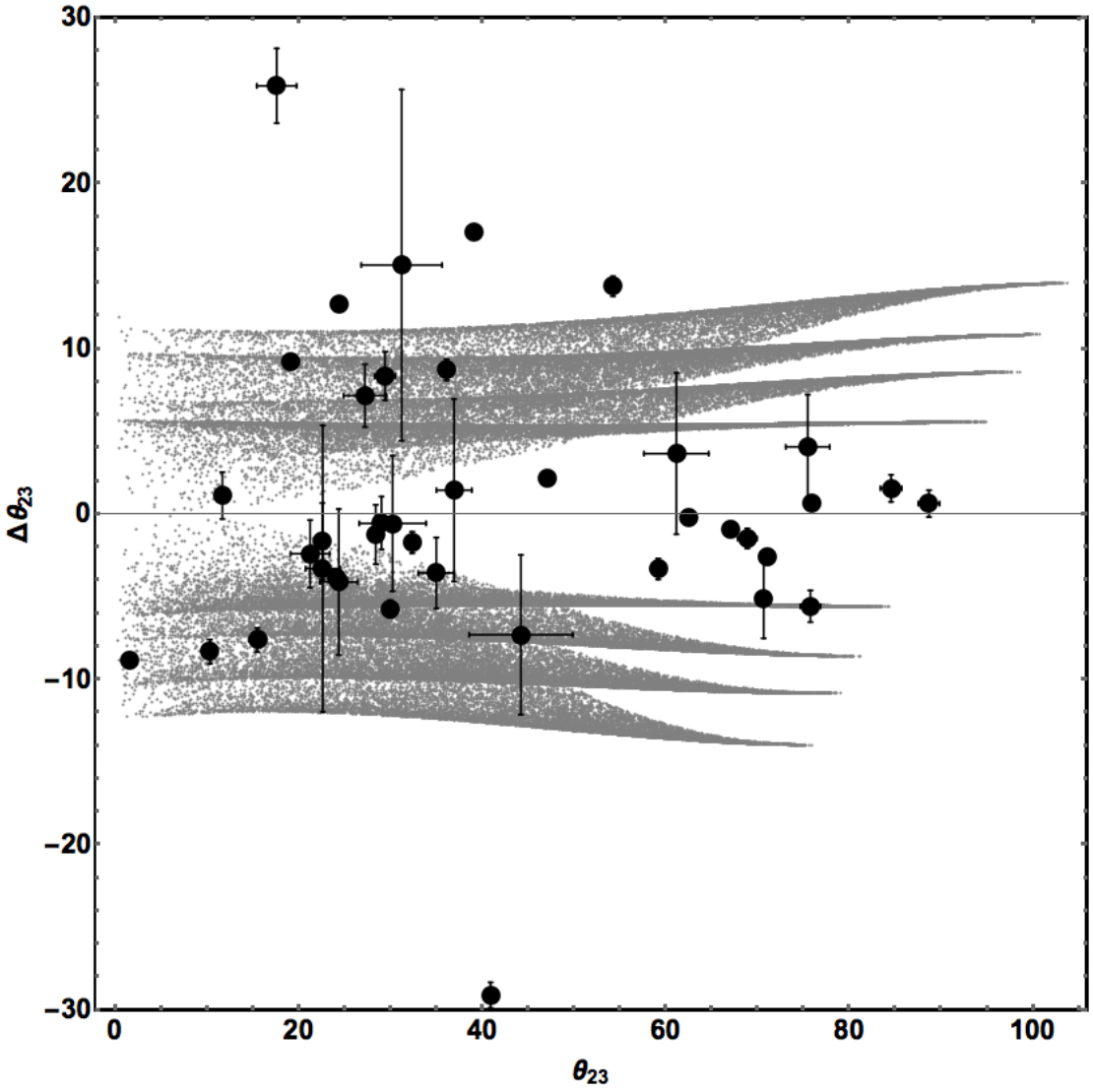


Figure 4.8: Distribution of observed quads (black filled circles) and quads from four Type II lenses (gray distributions) in $\theta_{23}$ vs. $\Delta\theta_{23}$ plane. The quad data and the errorbars were taken from WW11. $\Delta\theta_{23} = 0$ is FSQ. Each lens has two gray surfaces which are about equally close to, but on opposite sides of the FSQ. From the outermost to the innermost surfaces, the lens are: NFW ($\beta = 0.1$rad, $\epsilon = 0.27, \gamma = 0.25$), Power Law ($\alpha = 1.2, \beta = 0.2$rad, $\epsilon = 0.25, \gamma = 0.25$), Power Law ($\alpha = 1, \beta = 0.2$rad, $\epsilon = 0.15, \gamma = 0.17$), and Power Law ($\alpha = 0.9, \beta = 0.15$rad, $\epsilon = 0.14, \gamma = 0.13$), respectively.

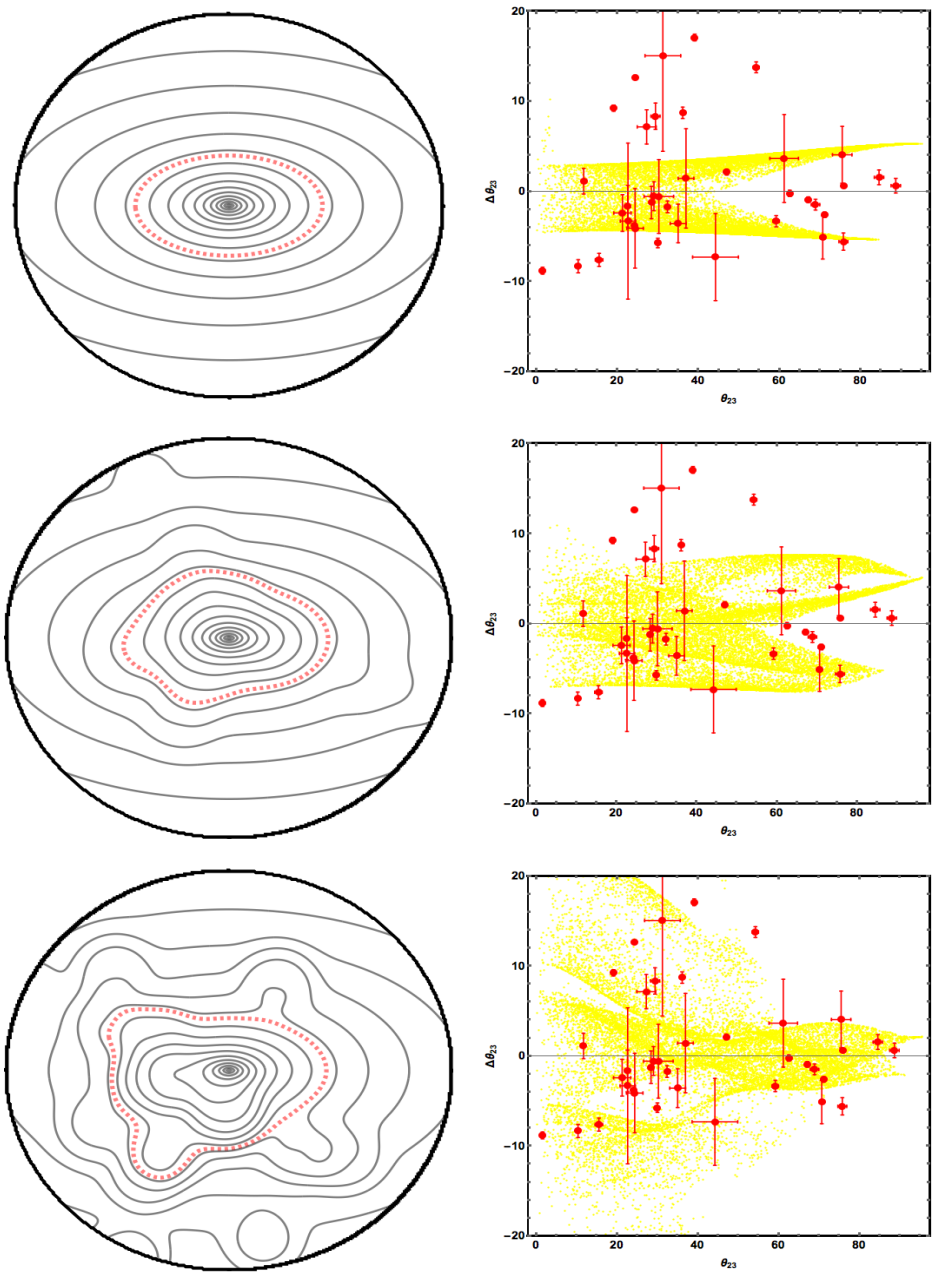


Figure 4.9: *Left panels:* All three have isothermal radial density profile with ellipticity $\epsilon = 0.25$ and shear $\gamma = 0.2$ oriented at an angle $\beta = \pi/6$ to each other. The $\kappa = 1$ contour is shown by the dashed, red, contour. *Right panels:* The corresponding distribution of quads from these lenses in the $\theta_{23}$ vs. $\Delta\theta_{23}$ plane are shown as the the light shade, yellow, distributions. The observed quads (same as in Figure 4.8) are red (black) dots. *Top:* A Type II lens with no substructure. *Middle:* A Type III lens with randomly distributed clumps that account for 4.38% of the total mass within the window. *Bottom:* A Type III lens with randomly distributed clumps that account for 17.96% of the total mass within the window.

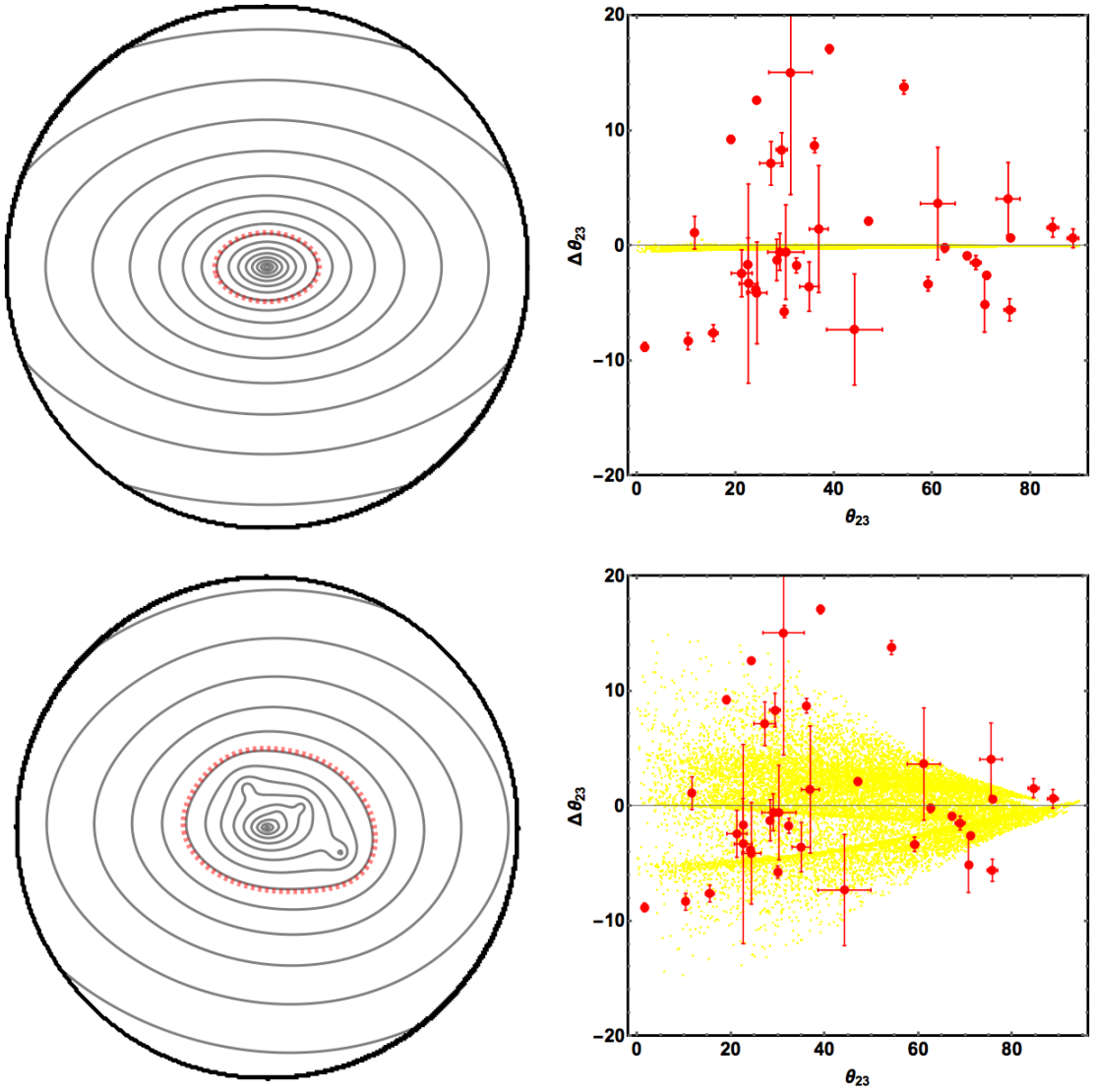


Figure 4.10: Similar to Figure 4.9, but different lenses. *Top panels:* A Type I lens with elliptical isothermal radial density profile with $\epsilon = 0.25$, and $\gamma = 0$. *Bottom panels:* A Type III substructured lens.

| Lens name | Radial Profile | L $(\beta, \epsilon, \gamma, \theta_{23,P})$ | Cross-validation RMSE (deg.) | Lens comparison RMSE (deg.) |
|---|---|---|---|---|
| A | SIEP | L (1.2, 0.09, 0.10366, 92) | 0.005 | |
| B | | L (1.2, 0.06603, 0.19, 92) | | A: 0.011 |
| C | | L (0.5, 0.14, 0.036752, 92) | | A: 0.029 |
| D | | L (0.5, 0.034944, 0.06, 92) | | A: 0.017 |
| E | | L ($\frac{\pi}{4}$, 0.069197, 0.08, 93) | 0.003 | |
| F | Power Law $\alpha$=1.2 | L ($\frac{\pi}{6}$, 0.2, 0.0446, 93) | 0.013 | |
| G | | L ($\frac{\pi}{6}$, 0.06536, 0.18, 93) | | E: 0.146, F: 0.551 |
| H | Power Law $\alpha$=0.9 | L ($\frac{\pi}{6}$, 0.04706, 0.11, 93) | 0.003 | E: 0.011 |
| I | | L ($\frac{\pi}{6}$, 0.095, 0.058, 93) | | H: 0.264 |
| J | NFW | L ($\frac{\pi}{6}$, 0.054, 0.075, 93) | 0.006 | E: 0.085 |
| JJ | | L ($\frac{\pi}{6}$, 0.075, 0.054, 93) | | J: 0.007 |
| K | | L ($\frac{\pi}{6}$, 0.13, 0.05265, 93) | 0.002 | J: 0.181 |
| KK | | L ($\frac{\pi}{6}$, 0.05265, 0.13, 93) | | K: 0.036 |

Table 4.1: Examples of Type II lenses. L $(\beta, \epsilon, \gamma, \theta_{23,P})$ refers to a lens with ellipticity $\epsilon$, external shear $\gamma$, which is oriented at an angle of $\beta$ (in radians) relative to the principal axis of the main lens, and relative image angle $\theta_{23,p}$ between images 2 and 3 of a central source. The subscript $p$ in $\theta_{23,p}$ indicates that it is the $\theta_{23}$ value of the quad located at the peak of the top surface in the 3D space of relative angles. The cross-validation column lists RMSE values between an interpolation fit to the lens and its own quads. The lens comparison column lists RMSE value between the fit to a lens (listed in column 5) and quads from a different lens (lens named in that row). Lenses JJ and J (and also K and KK) have their $\epsilon$ and $\gamma$ values swapped.

# Chapter 5

# Conclusion and future work

Gravitational lensing (GL) is a very valuable technique to probe the total mass distribution of galaxies. Direct mass modeling is the most commonly used approach to study galactic mass distribution using GL. This method fits one quad gravitational lens system at a time with finite set of parameters which are constrained by the properties of the quad images. But, since lens equation is severely under constrained which leads to more than one possible fit of a single lens system, parametric modeling does not always give the complete picture.

In this thesis, a novel statistical analysis of the angular distribution of quads with respect to the center of lenses is introduced. This method addresses population properties of quads and uses observational data to discriminate between classes of lens models. The summary of three different classes of lenses, as studied using our method, is given in Table 5.1. Preliminary work indicates that galaxies are not smooth. If this preliminary conclusion about substructure holds up under further scrutiny, then our work will provide a key test of $\Lambda$-CDM model.

We propose two major areas of expansion of the current work. One of these recommendations is to further investigate Type III lenses. Since this class is very vast by definition, everything but Type I and Type II, extensive exploration is required to make conclusive statements. The source of substructure suggested by the preliminary work is unknown at this point; therefore, using our method, future works can set out to address questions such as: Is it possible to identify the source of substructure( e.g. listed in Table 5.1)? And how much of it is there? and so on.

The other recommendation is to extend the 3D analysis to the full 6D space of relative positions of quad images. The degeneracies in the 3D space will probably break when viewed in higher dimensions. Nevertheless, since the relative angles space is an orthogonal subspace of the full 6D, the conclusion that Type I and Type II lenses do not represent the population property of observed quads will still hold true.

| | |
|---|---|
| **Type I Lenses** 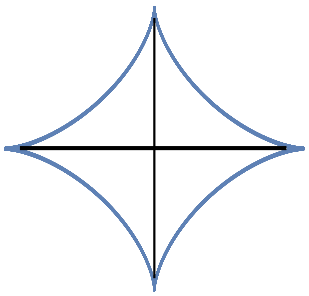 | • Obey double mirror and two fold symmetries.<br>• Existence of near-invariant surface in the 3D space of relative angles of quads (Fundamental Surface of Quads).<br>• Reproduce only 25% of observed quads. |
| **Type II Lenses** 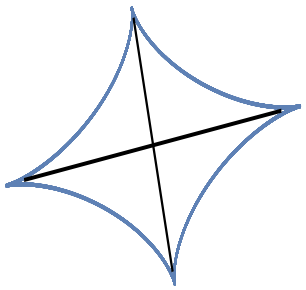 | • Obey two fold symmetry.<br>• The 3D space of relative angles has two surfaces.<br>• Existence of degeneracies in the potential space across different radial densities.<br>• Reproduce observed data only for small relative angles between the second and third arriving images.<br>• Predict existence of quads in observationally quad-void region of the 3D relative. space. |
| **Type III Lenses** 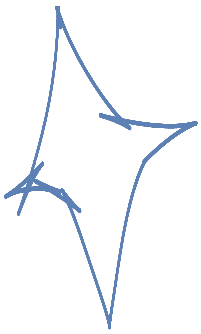 | • Anything but Type I and Type II.<br>• Preliminary work shows that observed data favors this class.<br>• The source of the substructure could be LOS, internal clumps, neighboring perturber. . . |

Table 5.1: Summary of the three types of lenses.

# References


[1] Addishiwot G. Woldesenbet. Dark Matter Candidate: A Singlet Scalar, 2007.

[2] Addishiwot G. Woldesenbet and Liliya L. R. Williams. The fundamental surface of quad lenses. *Monthly Notices of the Royal Astronomical Society*, 420: 2944–2955, /3/1 2012. URL `http://adsabs.harvard.edu/abs/2012MNRAS.420.2944W`.

[3] Edwin Hubble. A relation between distance and radial velocity among extragalactic nebulae. *Proceedings of the National Academy of Science*, 15:168–173, /3/1 1929. URL `http://adsabs.harvard.edu/abs/1929PNAS...15..168H`.

[4] V. M. Slipher. Nebulae. *Proceedings of the American Philosophical Society*, 56:403–409, /0/1 1917. URL `http://adsabs.harvard.edu/abs/1917PAPhS..56..403S`.

[5] Michael Rowan-Robinson. Cosmology author: Michael rowan-robinson, publisher: Oxford university press, usa pages: 200 published: 2004-01-29 isbn-1. 2004.

[6] J. V. Narlikar. *An Introduction to Cosmology*. Cambridge University Press,

2002. ISBN 9780521793766. URL https://books.google.com/books?id=3EbWfTXeC-EC.

[7] Albert A. Michelson and Edward W. Morley. On the relative motion of the earth and of the luminiferous ether. *Sidereal Messenger, vol.6, pp.306-310*, 6:306–310, /11/1 1887. URL http://adsabs.harvard.edu/abs/1887SidM....6..306M.

[8] Adam G. Riess, Lucas Macri, Stefano Casertano, Hubert Lampeitl, Henry C. Ferguson, Alexei V. Filippenko, Saurabh W. Jha, Weidong Li, and Ryan Chornock. A 3space telescope and wide field camera 3. *The Astrophysical Journal*, 730:119, /4/1 2011. URL http://adsabs.harvard.edu/abs/2011ApJ...730..119R.

[9] A. A. Penzias and R. W. Wilson. A measurement of excess antenna temperature at 4080 mc/s. *The Astrophysical Journal*, 142:419–421, /7/1 1965. URL http://adsabs.harvard.edu/abs/1965ApJ...142..419P.

[10] D. N. Spergel et al. Three-year wilkinson microwave anisotropy probe (wmap) observations: Implications for cosmology. *The Astrophysical Journal Supplement Series*, 170:377–408, /6/1 2007. URL http://adsabs.harvard.edu/abs/2007ApJS..170..377S.

[11] Max Pettini, Berkeley J. Zych, Michael T. Murphy, Antony Lewis, and Charles C. Steidel. Deuterium abundance in the most metal-poor damped lyman alpha system: converging on b,0h2. *Monthly Notices of the Royal*

*Astronomical Society*, 391:1499–1510, /12/1 2008. URL http://adsabs.harvard.edu/abs/2008MNRAS.391.1499P.

[12] F. W. Dyson, A. S. Eddington, and C. Davidson. A determination of the deflection of light by the sun's gravitational field, from observations made at the total eclipse of may 29, 1919. *Royal Society of London Philosophical Transactions Series A*, 220:291–333, /0/1 1920. URL http://adsabs.harvard.edu/abs/1920RSPTA.220..291D.

[13] A. Einstein. Erklarung der perihelionbewegung der merkur aus der allgemeinen relativitatstheorie. *Sitzungsber.preuss.Akad.Wiss., vol.47, No.2, pp.831-839, 1915*, 47:831–839, /0/1 1915. URL http://adsabs.harvard.edu/abs/1915SPAW...47..831E.

[14] E. B. Fomalont and R. A. Sramek. A confirmation of einstein's general theory of relativity by measuring the bending of microwave radiation in the gravitational field of the sun. *The Astrophysical Journal*, 199:749–755, /8/1 1975. URL http://adsabs.harvard.edu/abs/1975ApJ...199..749F.

[15] D. Walsh, R. F. Carswell, and R. J. Weymann. 0957 + 561 a, b - twin quasistellar objects or gravitational lens. *Nature*, 279:381–384, /5/1 1979. URL http://adsabs.harvard.edu/abs/1979Natur.279..381W.

[16] C.S. Kochanek, E.E. Falco, C. Impey, J. Lehar, B. McLeod, and H. X. Rix. Castles survey. URL https://www.cfa.harvard.edu/castles/.

[17] Peter Schneider, J Ehlers, and Emilio E. Falco. *Gravitational Lenses*. /0/1 1992. URL http://adsabs.harvard.edu/abs/1992grle.book.....S.

[18] Ramesh Narayan and Matthias Bartelmann. Lectures on gravitational lensing, /6/1 1996. URL http://adsabs.harvard.edu/abs/1996astro.ph..6001N. TY: Preprint.

[19] J. A. Tyson, R. A. Wenk, and F. Valdes. Detection of systematic gravitational lens galaxy image alignments - mapping dark matter in galaxy clusters. *The Astrophysical Journal Letters*, 349:L1–L4, /1/1 1990. URL http://adsabs.harvard.edu/abs/1990ApJ...349L...1T.

[20] F. Zwicky. On the masses of nebulae and of clusters of nebulae. *The Astrophysical Journal*, 86:217, 1937/10/1 1937. URL http://adsabs.harvard.edu/abs/1937ApJ....86..217Z.

[21] John S. Mulchaey, David S. Davis, Richard F. Mushotzky, and David Burstein. Diffuse x-ray emission from the ngc 2300 group of galaxies - implications for dark matter and galaxy evolution in small groups. *The Astrophysical Journal Letters*, 404:L9–L12, /2/1 1993. URL http://adsabs.harvard.edu/abs/1993ApJ...404L...9M.

[22] J. F. Navarro and S. D. M. White. Simulations of dissipative galaxy formation in hierarchically clustering universes - part one - tests of the code. *Monthly Notices of the Royal Astronomical Society*, 265:271, /11/1 1993. URL http://adsabs.harvard.edu/abs/1993MNRAS.265..271N.

[23] V. C. Rubin, J. Ford, W. K., C. J. Peterson, and C. R. Lynds. A new mapping of the velocity field of ngc 1275. *The Astrophysical Journal Supplement Series*,

37:235–249, /6/1 1978. URL http://adsabs.harvard.edu/abs/1978ApJS...37..235R.

[24] V. C. Rubin, J. Ford, W. K., K. M. Strom, S. E. Strom, and W. Romanishin. Extended rotation curves of high-luminosity spiral galaxies. ii - the anemic sa galaxy ngc 4378. *The Astrophysical Journal*, 224:782–795, /9/1 1978. URL http://adsabs.harvard.edu/abs/1978ApJ...224..782R.

[25] V. C. Rubin, N. Thonnard, and J. Ford, W. K. Extended rotation curves of high-luminosity spiral galaxies. iv - systematic dynamical properties, sa through sc. *The Astrophysical Journal Letters*, 225:L107–L111, /11/1 1978. URL http://adsabs.harvard.edu/abs/1978ApJ...225L.107R.

[26] Robert H. Sanders and Stacy S. McGaugh. Modified newtonian dynamics as an alternative to dark matter. *Annual Review of Astronomy and Astrophysics*, 40:263–317, /0/1 2002. URL http://adsabs.harvard.edu/abs/2002ARA%26A..40..263S.

[27] C. L. Bennett, M. Halpern, G. Hinshaw, N. Jarosik, A. Kogut, M. Limon, S. S. Meyer, L. Page, D. N. Spergel, G. S. Tucker, E. Wollack, E. L. Wright, C. Barnes, M. R. Greason, R. S. Hill, E. Komatsu, M. R. Nolta, N. Odegard, H. V. Peiris, L. Verde, and J. L. Weiland. First-year wilkinson microwave anisotropy probe (wmap) observations: Preliminary maps and basic results. *The Astrophysical Journal Supplement Series*, 148:1–27, /9/1 2003. URL http://adsabs.harvard.edu/abs/2003ApJS..148....1B.

[28] Keith A. Olive. Tasi lectures on dark matter, /1/1 2003. URL http://adsabs.harvard.edu/abs/2003astro.ph..1505O. TY: Preprint.

[29] D. Fabricant and P. Gorenstein. Further evidence for m87's massive, dark halo. *The Astrophysical Journal*, 267:535–546, /4/1 1983. URL http://adsabs.harvard.edu/abs/1983ApJ...267..535F.

[30] Planck Collaboration, P. A. R. Ade, N. Aghanim, M. Arnaud, M. Ashdown, J. Aumont, C. Baccigalupi, A. J. Banday, R. B. Barreiro, J. G. Bartlett, N. Bartolo, E. Battaner, R. Battye, K. Benabed, A. Benoit, A. Benoit-Levy, J. . Bernard, M. Bersanelli, P. Bielewicz, A. Bonaldi, L. Bonavera, J. R. Bond, J. Borrill, F. R. Bouchet, F. Boulanger, M. Bucher, C. Burigana, R. C. Butler, E. Calabrese, J. . Cardoso, A. Catalano, A. Challinor, A. Chamballu, R. . Chary, H. C. Chiang, J. Chluba, P. R. Christensen, S. Church, D. L. Clements, S. Colombi, L. P. L. Colombo, C. Combet, A. Coulais, B. P. Crill, A. Curto, F. Cuttaia, L. Danese, R. D. Davies, R. J. Davis, P. de Bernardis, A. de Rosa, G. de Zotti, J. Delabrouille, F. . Desert, E. Di Valentino, C. Dickinson, J. M. Diego, K. Dolag, H. Dole, S. Donzelli, O. Dore, M. Douspis, A. Ducout, J. Dunkley, X. Dupac, G. Efstathiou, F. Elsner, T. A. Ensslin, H. K. Eriksen, M. Farhang, J. Fergusson, F. Finelli, O. Forni, M. Frailis, A. A. Fraisse, E. Franceschi, A. Frejsel, S. Galeotta, S. Galli, K. Ganga, C. Gauthier, M. Gerbino, T. Ghosh, M. Giard, Y. Giraud-Heraud, E. Giusarma, E. Gjerlow, J. Gonzalez-Nuevo, K. M. Gorski, S. Gratton, A. Gregorio, A. Gruppuso, J. E. Gudmundsson, J. Hamann, F. K. Hansen, D. Hanson, D. L. Harrison, G. Helou, S. Henrot-Versille, C. Hernandez-Monteagudo,

D. Herranz, S. R. Hildebrandt, E. Hivon, M. Hobson, W. A. Holmes, A. Hornstrup, W. Hovest, Z. Huang, K. M. Huffenberger, G. Hurier, A. H. Jaffe, T. R. Jaffe, W. C. Jones, M. Juvela, E. Keihanen, R. Keskitalo, T. S. Kisner, R. Kneissl, J. Knoche, L. Knox, M. Kunz, H. Kurki-Suonio, G. Lagache, A. Lahteenmaki, J. . Lamarre, A. Lasenby, M. Lattanzi, C. R. Lawrence, J. P. Leahy, R. Leonardi, J. Lesgourgues, F. Levrier, A. Lewis, M. Liguori, P. B. Lilje, M. Linden-Vornle, M. Lopez-Caniego, P. M. Lubin, J. Macias-Perez, G. Maggio, D. Maino, N. Mandolesi, A. Mangilli, A. Marchini, P. G. Martin, M. Martinelli, E. Martinez-Gonzalez, S. Masi, S. Matarrese, P. Mazzotta, P. McGehee, P. R. Meinhold, A. Melchiorri, J. . Melin, L. Mendes, A. Mennella, M. Migliaccio, M. Millea, S. Mitra, M. Miville-Deschenes, A. Moneti, L. Montier, G. Morgante, D. Mortlock, A. Moss, D. Munshi, J. A. Murphy, P. Naselsky, F. Nati, P. Natoli, C. B. Netterfield, H. Norgaard-Nielsen, F. Noviello, D. Novikov, I. Novikov, C. A. Oxborrow, F. Paci, L. Pagano, F. Pajot, R. Paladini, D. Paoletti, B. Partridge, F. Pasian, G. Patanchon, T. J. Pearson, O. Perdereau, L. Perotto, F. Perrotta, V. Pettorino, F. Piacentini, M. Piat, E. Pierpaoli, D. Pietrobon, S. Plaszczynski, E. Pointecouteau, G. Polenta, L. Popa, G. W. Pratt, G. Prezeau, S. Prunet, J. . Puget, J. P. Rachen, W. T. Reach, R. Rebolo, M. Reinecke, M. Remazeilles, C. Renault, A. Renzi, I. Ristorcelli, G. Rocha, C. Rosset, M. Rossetti, G. Roudier, B. Rouille d'Orfeuil, M. Rowan-Robinson, J. Rubino-Martin, B. Rusholme, N. Said, V. Salvatelli, L. Salvati, M. Sandri, D. Santos, M. Savelainen, G. Savini, D. Scott, M. D. Seiffert, P. Serra, E. P. S. Shellard, L. D. Spencer, M. Spinelli, V. Stolyarov, R. Stompor, R. Sudiwala, R. Sunyaev, D. Sutton,

A. Suur-Uski, J. . Sygnet, J. A. Tauber, L. Terenzi, L. Toffolatti, M. Tomasi, M. Tristram, T. Trombetti, M. Tucci, J. Tuovinen, M. Turler, G. Umana, L. Valenziano, J. Valiviita, B. Van Tent, P. Vielva, F. Villa, L. A. Wade, B. D. Wandelt, I. K. Wehus, M. White, S. D. M. White, A. Wilkinson, D. Yvon, A. Zacchei, and A. Zonca. Planck 2015 results. xiii. cosmological parameters, /2/1 2015. URL http://adsabs.harvard.edu/abs/2015arXiv150201589P. TY: Preprint.

[31] G. Hinshaw, D. Larson, E. Komatsu, D. N. Spergel, C. L. Bennett, J. Dunkley, M. R. Nolta, M. Halpern, R. S. Hill, N. Odegard, L. Page, K. M. Smith, J. L. Weiland, B. Gold, N. Jarosik, A. Kogut, M. Limon, S. S. Meyer, G. S. Tucker, E. Wollack, and E. L. Wright. Nine-year wilkinson microwave anisotropy probe (wmap) observations: Cosmological parameter results. *The Astrophysical Journal Supplement Series*, 208:19, /10/1 2013. URL http://adsabs.harvard.edu/abs/2013ApJS..208...19H.

[32] Anthony Tyson. Mapping dark matter with gravitational lenses. *Physics Today*, 45:24–32, /6/1 1992. URL http://adsabs.harvard.edu/abs/1992PhT....45f..24T.

[33] M. Fukugita, C. J. Hogan, and P. J. E. Peebles. The cosmic baryon budget. *The Astrophysical Journal*, 503:518–530, /8/1 1998. URL http://adsabs.harvard.edu/abs/1998ApJ...503..518F.

[34] C. Alcock, R. Allsman, D. R. Alves, T. Axelrod, A. Becker, D. Bennett, C. Clement, K. H. Cook, A. Drake, K. Freeman, M. Geha, K. Griest, G. Kovcs, D. W. Kurtz, M. Lehner, S. Marshall, D. Minniti, C. Nelson, B. Peterson, P. Popowski, M. Pratt, P. Quinn, A. Rodgers, J. Rowe, C. Stubbs, W. Sutherland, A. Tomaney, T. Vandehei, and D. L. Welch. The macho project large magellanic cloud variable-star inventory. ix. frequency analysis of the first-overtone rr lyrae stars and the indication for nonradial pulsations. *The Astrophysical Journal*, 542:257–280, /10/1 2000. URL `http://adsabs.harvard.edu/abs/2000ApJ...542..257A`.

[35] E. W. Kolb and M. S. Turner. *The early universe*. /0/1 1990. URL `http://adsabs.harvard.edu/abs/1990eaun.book.....K`.

[36] J. K. Ahn, S. Chebotaryov, J. H. Choi, S. Choi, W. Choi, Y. Choi, H. I. Jang, J. S. Jang, E. J. Jeon, I. S. Jeong, K. K. Joo, B. R. Kim, B. C. Kim, H. S. Kim, J. Y. Kim, S. B. Kim, S. H. Kim, S. Y. Kim, W. Kim, Y. D. Kim, J. Lee, J. K. Lee, I. T. Lim, K. J. Ma, M. Y. Pac, I. G. Park, J. S. Park, K. S. Park, J. W. Shin, K. Siyeon, B. S. Yang, I. S. Yeo, S. H. Yi, and I. Yu. Observation of reactor electron antineutrinos disappearance in the reno experiment. *Physical Review Letters*, 108:191802, /5/1 2012. URL `http://adsabs.harvard.edu/abs/2012PhRvL.108s1802A`.

[37] Y. Fukuda et al. Evidence for oscillation of atmospheric neutrinos. *Physical Review Letters*, 81:1562–1567, /8/1 1998. URL `http://adsabs.harvard.edu/abs/1998PhRvL..81.1562F`.

[38] G. Jungman, M. Kamionkowski, and K. Griest. Supersymmetric dark matter. *Physics Reports*, 267:195–373, /3/1 1996. URL http://adsabs.harvard.edu/abs/1996PhR...267..195J.

[39] Liliya L. R. Williams, Patrick Foley, Damon Farnsworth, and Jason Belter. Lensed image angles: New statistical evidence for substructure. *The Astrophysical Journal*, 685:725–738, /10/1 2008. URL http://adsabs.harvard.edu/abs/2008ApJ...685..725W.

[40] Prasenjit Saha and Liliya L. R. Williams. Qualitative theory for lensed qsos. *The Astronomical Journal*, 125:2769–2782, /6/1 2003. URL http://adsabs.harvard.edu/abs/2003AJ....125.2769S.

[41] Aggeliki Kassiola and Israel Kovner. Elliptic mass distributions versus elliptic potentials in gravitational lenses. *The Astrophysical Journal*, 417:450, /11/1 1993. URL http://adsabs.harvard.edu/abs/1993ApJ...417..450K.

[42] Christopher S. Kochanek. The implications of lenses for galaxy structure. *The Astrophysical Journal*, 373:354–368, /6/1 1991. URL http://adsabs.harvard.edu/abs/1991ApJ...373..354K.

[43] N. Dalal. The magnification invariant of simple galaxy lens models. *The Astrophysical Journal Letters*, 509:L13–L16, /12/1 1998. URL http://adsabs.harvard.edu/abs/1998ApJ...509L..13D.

[44] C. D. Fassnacht, R. D. Blandford, J. G. Cohen, K. Matthews, T. J. Pearson, A. C. S. Readhead, D. S. Womble, S. T. Myers, I. W. A. Browne, N. J.

Jackson, D. R. Marlow, P. N. Wilkinson, L. V. E. Koopmans, A. G. de Bruyn, R. T. Schilizzi, M. Bremer, and G. Miley. B2045+265: A new four-image gravitational lens from class. *The Astronomical Journal*, 117:658–670, /2/1 1999. URL http://adsabs.harvard.edu/abs/1999AJ....117..658F.

[45] Sahar S. Allam, Douglas L. Tucker, Huan Lin, H. T. Diehl, James Annis, Elizabeth Buckley-Geer, and Joshua A. Frieman. The 8 o'clock arc: A serendipitous discovery of a strongly lensed lyman break galaxy in the sdss dr4 imaging data. *The Astrophysical Journal Letters*, 662:L51–L54, /6/1 2007. URL http://adsabs.harvard.edu/abs/2007ApJ...662L..51A.

[46] Charles R. Keeton. A catalog of mass models for gravitational lensing, /2/1 2001. URL http://adsabs.harvard.edu/abs/2001astro.ph..2341K. TY: Preprint.

[47] C. Grillo, T. Eichner, S. Seitz, R. Bender, M. Lombardi, R. Gobat, and A. Bauer. Golden gravitational lensing systems from the sloan lens acs survey. i. sdss j1538+5817: One lens for two sources. *The Astrophysical Journal*, 710:372–384, /2/1 2010. URL http://adsabs.harvard.edu/abs/2010ApJ...710..372G.

[48] I. Burud, F. Courbin, C. Lidman, A. O. Jaunsen, J. Hjorth, R. stensen, M. I. Andersen, J. W. Clasen, O. Wucknitz, G. Meylan, P. Magain, R. Stabell, and S. Refsdal. High-resolution optical and near-infrared imaging of the quadruple quasar rx j0911.4+0551. *The Astrophysical Journal Letters*, 501:L5–L10, /7/1 1998. URL http://adsabs.harvard.edu/abs/1998ApJ...501L...5B.

[49] L Koopmans, Tommaso Treu, Adam S. Bolton, Scott Burles, and Leonidas A. Moustakas. The sloan lens acs survey. iii. the structure and formation of early-type galaxies and their evolution since z 1. *The Astrophysical Journal*, 649: 599–615, /10/1 2006. URL `http://adsabs.harvard.edu/abs/2006ApJ...649..599K`.

[50] L. Wisotzki, N. Christlieb, M. C. Liu, J. Maza, N. D. Morgan, and P. L. Schechter. The new complex gravitational lens system he 0230-2130. *Astronomy and Astrophysics*, 348:L41–L44, /8/1 1999. URL `http://adsabs.harvard.edu/abs/1999A%26A...348L..41W`.

[51] Prasenjit Saha and Liliya L. R. Williams. A portable modeler of lensed quasars. *The Astronomical Journal*, 127:2604–2616, /5/1 2004. URL `http://adsabs.harvard.edu/abs/2004AJ....127.2604S`.

[52] S. Nair and M. A. Garrett. Gravitational lens models for 2016+112. *Monthly Notices of the Royal Astronomical Society*, 284:58–72, /1/1 1997. URL `http://adsabs.harvard.edu/abs/1997MNRAS.284...58N`.

[53] C. R. Lawrence, D. P. Schneider, M. Schmidt, C. L. Bennett, J. N. Hewitt, B. F. Burke, E. L. Turner, and J. E. Gunn. Discovery of a new gravitational lens system. *Science*, 223:46–49, /1/1 1984. URL `http://adsabs.harvard.edu/abs/1984Sci...223...46L`.

[54] S. Nair. Modelling the 10-image lensed system b1933+503. *Monthly Notices of the Royal Astronomical Society*, 301:315–322, /12/1 1998. URL `http://adsabs.harvard.edu/abs/1998MNRAS.301..315N`.

[55] Ignacio Ferreras, Prasenjit Saha, and Scott Burles. Unveiling dark haloes in lensing galaxies. *Monthly Notices of the Royal Astronomical Society*, 383: 857–863, /1/1 2008. URL http://adsabs.harvard.edu/abs/2008MNRAS.383..857F.

[56] Issha Kayo, Naohisa Inada, Masamune Oguri, Patrick B. Hall, Christopher S. Kochanek, Gordon T. Richards, Donald P. Schneider, Donald G. York, and Kaike Pan. A new quadruply lensed quasar: Sdss j125107.57+293540.5. *The Astronomical Journal*, 134:1515–1521, /10/1 2007. URL http://adsabs.harvard.edu/abs/2007AJ....134.1515K.

[57] Masamune Oguri, Naohisa Inada, Jeffrey A. Blackburne, Min-Su Shin, Issha Kayo, Michael A. Strauss, Donald P. Schneider, and Donald G. York. Mass models and environment of the new quadruply lensed quasar sdss j1330+1810. *Monthly Notices of the Royal Astronomical Society*, 391:1973–1980, /12/1 2008. URL http://adsabs.harvard.edu/abs/2008MNRAS.391.1973O.

[58] Neal Jackson. Gravitational lenses and lens candidates identified from the cosmos field. *Monthly Notices of the Royal Astronomical Society*, 389:1311–1318, /9/1 2008. URL http://adsabs.harvard.edu/abs/2008MNRAS.389.1311J.

[59] Huan Lin, Elizabeth Buckley-Geer, Sahar S. Allam, Douglas L. Tucker, H. T. Diehl, Donna Kubik, Jeffrey M. Kubo, James Annis, Joshua A. Frieman, Masamune Oguri, and Naohisa Inada. Discovery of a very bright, strongly

lensed z = 2 galaxy in the sdss dr5. *The Astrophysical Journal*, 699:1242–1251, /7/1 2009. URL http://adsabs.harvard.edu/abs/2009ApJ...699.1242L.

[60] Adam S. Bolton, Scott Burles, L Koopmans, Tommaso Treu, and Leonidas A. Moustakas. Sdss j140228.22+632133.3: A new spectroscopically selected gravitational lens. *The Astrophysical Journal Letters*, 624:L21–L24, /5/1 2005. URL http://adsabs.harvard.edu/abs/2005ApJ...624L..21B.

[61] Jeffrey A. Blackburne, Lutz Wisotzki, and Paul L. Schechter. He 1113-0641: The smallest-separation quadruple lens identified by a ground-based optical telescope. *The Astronomical Journal*, 135:374–379, /1/1 2008. URL http://adsabs.harvard.edu/abs/2008AJ....135..374B.

[62] Raphal Gavazzi, Tommaso Treu, L Koopmans, Adam S. Bolton, Leonidas A. Moustakas, Scott Burles, and Philip J. Marshall. The sloan lens acs survey. vi. discovery and analysis of a double einstein ring. *The Astrophysical Journal*, 677:1046–1059, /4/1 2008. URL http://adsabs.harvard.edu/abs/2008ApJ...677.1046G.

[63] D. Walsh, R. F. Carswell, R. J. Weymann, B. F. Burke, P. E. Greenfield, D. H. Roberts, E. E. Becklin, P. Young, J. E. Gunn, J. Kristian, J. B. Oke, and J. A. Westphal. Gravity's lens - squinting at a galaxy. *Science News*, 117:36, /0/1 1980. URL http://adsabs.harvard.edu/abs/1980SciN..117...36W.

[64] P. Young, J. E. Gunn, J. Kristian, J. B. Oke, and J. A. Westphal. The double quasar q0957 + 561 a, b - a gravitational lens image formed by a

galaxy at z = 0.39. *The Astrophysical Journal*, 241:507–520, /10/1 1980. URL http://adsabs.harvard.edu/abs/1980ApJ...241..507Y.

[65] Roger Blandford and Ramesh Narayan. Fermat's principle, caustics, and the classification of gravitational lens images. *The Astrophysical Journal*, 310: 568–582, /11/1 1986. URL http://adsabs.harvard.edu/abs/1986ApJ...310..568B.

[66] E. E. Falco, M. V. Gorenstein, and I. I. Shapiro. On model-dependent bounds on h(0) from gravitational images application of q0957 + 561a,b. *The Astrophysical Journal Letters*, 289:L1–L4, /2/1 1985. URL http://adsabs.harvard.edu/abs/1985ApJ...289L...1F.

[67] M. V. Gorenstein, I. I. Shapiro, and E. E. Falco. Degeneracies in parameter estimates for models of gravitational lens systems. *The Astrophysical Journal*, 327:693–711, /4/1 1988. URL http://adsabs.harvard.edu/abs/1988ApJ...327..693G.

[68] Prasenjit Saha. Lensing degeneracies revisited. *The Astronomical Journal*, 120:1654–1659, /10/1 2000. URL http://adsabs.harvard.edu/abs/2000AJ....120.1654S.

[69] J. Liesenborgs and S. De Rijcke. Lensing degeneracies and mass substructure. *Monthly Notices of the Royal Astronomical Society*, 425:1772–1780, /9/1 2012. URL http://adsabs.harvard.edu/abs/2012MNRAS.425.1772L.

[70] Hans J. Witt and Shude Mao. On the minimum magnification between caustic crossings for microlensing by binary and multiple stars. *The Astrophysical*

*Journal Letters*, 447:L105, /7/1 1995. URL http://adsabs.harvard.edu/abs/1995ApJ...447L.105W.

[71] Hans J. Witt and Shude Mao. On the magnification relations in quadruple lenses: a moment approach. *Monthly Notices of the Royal Astronomical Society*, 311:689–697, /2/1 2000. URL http://adsabs.harvard.edu/abs/2000MNRAS.311..689W.

[72] C. Hunter and N. W. Evans. Lensing properties of scale-free galaxies. *The Astrophysical Journal*, 554:1227–1244, /6/1 2001. URL http://adsabs.harvard.edu/abs/2001ApJ...554.1227H.

[73] Peter Schneider and Dominique Sluse. Source-position transformation: an approximate invariance in strong gravitational lensing. *Astronomy and Astrophysics*, 564:A103, /4/1 2014. URL http://adsabs.harvard.edu/abs/2014A%26A...564A.103S.

[74] Ben Moore, Sebastiano Ghigna, Fabio Governato, George Lake, Thomas Quinn, Joachim Stadel, and Paolo Tozzi. Dark matter substructure within galactic halos. *The Astrophysical Journal Letters*, 524:L19–L22, /10/1 1999. URL http://adsabs.harvard.edu/abs/1999ApJ...524L..19M.

[75] Anatoly Klypin, Andrey V. Kravtsov, Octavio Valenzuela, and Francisco Prada. Where are the missing galactic satellites? *The Astrophysical Journal*, 522:82–92, /9/1 1999. URL http://adsabs.harvard.edu/abs/1999ApJ...522...82K.

[76] P. Schneider and A. Weiss. The gravitational lens equation near cusps. *Astronomy and Astrophysics*, 260:1–13, /7/1 1992. URL http://adsabs.harvard.edu/abs/1992A%26A...260....1S.

[77] Shude Mao and Peter Schneider. Evidence for substructure in lens galaxies? *Monthly Notices of the Royal Astronomical Society*, 295:587, /4/1 1998. URL http://adsabs.harvard.edu/abs/1998MNRAS.295..587M.

[78] R. B. Metcalf and HongSheng Zhao. Flux ratios as a probe of dark substructures in quadruple-image gravitational lenses. *The Astrophysical Journal Letters*, 567:L5–L8, /3/1 2002. URL http://adsabs.harvard.edu/abs/2002ApJ...567L...5M.

[79] Dandan Xu, Dominique Sluse, Liang Gao, Jie Wang, Carlos Frenk, Shude Mao, Peter Schneider, and Volker Springel. How well can cold dark matter substructures account for the observed radio flux-ratio anomalies. *Monthly Notices of the Royal Astronomical Society*, 447:3189–3206, /3/1 2015. URL http://adsabs.harvard.edu/abs/2015MNRAS.447.3189X.

[80] Israel Kovner. The quadrupole gravitational lens. *The Astrophysical Journal*, 312:22–44, /1/1 1987. URL http://adsabs.harvard.edu/abs/1987ApJ...312...22K.

[81] Julio F. Navarro, Carlos S. Frenk, and Simon D. M. White. A universal density profile from hierarchical clustering. *The Astrophysical Journal*, 490:493–508, /12/1 1997. URL http://adsabs.harvard.edu/abs/1997ApJ...490..493N.

[82] G. Golse and J. . Kneib. Pseudo elliptical lensing mass model: Application to the nfw mass distribution. *Astronomy and Astrophysics*, 390:821–827, /8/1 2002. URL http://adsabs.harvard.edu/abs/2002A%26A...390..821G.

[83] Adam S. Bolton, Scott Burles, L Koopmans, Tommaso Treu, Raphal Gavazzi, Leonidas A. Moustakas, Randall Wayth, and David J. Schlegel. The sloan lens acs survey. v. the full acs strong-lens sample. *The Astrophysical Journal*, 682:964–984, /8/1 2008. URL http://adsabs.harvard.edu/abs/2008ApJ...682..964B.

[84] D. Sluse, V. Chantry, P. Magain, F. Courbin, and G. Meylan. Cosmograil: the cosmological monitoring of gravitational lenses. x. modeling based on high-precision astrometry of a sample of 25 lensed quasars: consequences for ellipticity, shear, and astrometric anomalies. *Astronomy and Astrophysics*, 538:A99, /2/1 2012. URL http://adsabs.harvard.edu/abs/2012A%26A...538A..99S.

[85] Kenneth C. Wong, Charles R. Keeton, Kurtis A. Williams, Ivelina G. Momcheva, and Ann I. Zabludoff. The effect of environment on shear in strong gravitational lenses. *The Astrophysical Journal*, 726:84, /1/1 2011. URL http://adsabs.harvard.edu/abs/2011ApJ...726...84W.

[86] Neal Dalal. What are the environments of lens galaxies? page 12, /2/1 2005. URL http://adsabs.harvard.edu/abs/2005tyad.confE..12D.

[87] C. R. Keeton, C. S. Kochanek, and U. Seljak. Shear and ellipticity in gravitational lenses. *The Astrophysical Journal*, 482:604–620, /6/1 1997. URL `http://adsabs.harvard.edu/abs/1997ApJ...482..604K`.

[88] Gilbert P. Holder and Paul L. Schechter. External shear in quadruply imaged lens systems. *The Astrophysical Journal*, 589:688–692, /6/1 2003. URL `http://adsabs.harvard.edu/abs/2003ApJ...589..688H`.

# Appendix A

# Mathematica Code

This code is used to create synthetic lenses and their corresponding 3D plots.

This part calculates the coordinates of the cusps of the diamond caustic. This helps to find quads that make up the edges of the 3D surface since they emanate from sources on the diagonals of the caustic.

**right-upper for caustic of elongated(extended) opposite cusps. It uses the method of rotation by 2*abs(the angle the right cusp of the not rotated caustic makes with the x-axis),calculate peak in the first quadrant, then rotate back to find original right-upper peak.**

```
RUE[θ_, β_, γ_, ϵ_, b_] :=
  Flatten[{Cos[2 * .563974] * (MaxValue[{Cos[2 * .563974] * ((b (-1 + ϵ)
                  (-γ (1 + ϵ) Cos[2 β - 3 θ] + γ^2 (1 + ϵ) Cos[4 β - 3 θ] -
                    3 γ (1 + ϵ) Cos[2 β - θ] + 3 (γ^2 + ϵ) Cos[θ] - (-1 + γ^2) ϵ Cos[3 θ])) /
                (2 (-1 + γ^2) (1 - ϵ Cos[2 θ])^(3 / 2))) + Sin[2 * .563974] *
              (-(b (1 + ϵ) (-γ (-1 + ϵ) Sin[2 β - 3 θ] - γ^2 (-1 + ϵ) Sin[4 β - 3 θ] +
                    3 γ (-1 + ϵ) Sin[2 β - θ] + 3 (γ^2 - ϵ) Sin[θ] - (-1 + γ^2) ϵ Sin[3 θ])) /
                (2 (-1 + γ^2) (1 - ϵ Cos[2 θ])^(3 / 2))), 0 ≤ θ < 2 π}, {θ}]) -
      Sin[2 * .563974] * (-Sin[2 * .563974] * ((b (-1 + ϵ) (-γ (1 + ϵ) Cos[2 β - 3 θ] +
                  γ^2 (1 + ϵ) Cos[4 β - 3 θ] - 3 γ (1 + ϵ) Cos[2 β - θ] +
                  3 (γ^2 + ϵ) Cos[θ] - (-1 + γ^2) ϵ Cos[3 θ])) /
                (2 (-1 + γ^2) (1 - ϵ Cos[2 θ])^(3 / 2))) + Cos[2 * .563974] *
              (-(b (1 + ϵ) (-γ (-1 + ϵ) Sin[2 β - 3 θ] - γ^2 (-1 + ϵ) Sin[4 β - 3 θ] +
                    3 γ (-1 + ϵ) Sin[2 β - θ] + 3 (γ^2 - ϵ) Sin[θ] - (-1 + γ^2) ϵ Sin[3 θ])) /
                (2 (-1 + γ^2) (1 - ϵ Cos[2 θ])^(3 / 2))))) /. θ → ArgMax[
        {Cos[2 * .563974] * ((b (-1 + ϵ) (-γ (1 + ϵ) Cos[2 β - 3 θ] + γ^2 (1 + ϵ) Cos[4 β - 3 θ] -
                    3 γ (1 + ϵ) Cos[2 β - θ] + 3 (γ^2 + ϵ) Cos[θ] - (-1 + γ^2) ϵ Cos[3 θ])) /
                (2 (-1 + γ^2) (1 - ϵ Cos[2 θ])^(3 / 2))) + Sin[2 * .563974] *
              (-(b (1 + ϵ) (-γ (-1 + ϵ) Sin[2 β - 3 θ] - γ^2 (-1 + ϵ) Sin[4 β - 3 θ] +
                    3 γ (-1 + ϵ) Sin[2 β - θ] + 3 (γ^2 - ϵ) Sin[θ] - (-1 + γ^2) ϵ Sin[3 θ])) /
                (2 (-1 + γ^2) (1 - ϵ Cos[2 θ])^(3 / 2))), 0 ≤ θ < 2 π}, {θ}],
      Sin[2 * .563974] * (MaxValue[{Cos[2 * .563974] * ((b (-1 + ϵ)
                  (-γ (1 + ϵ) Cos[2 β - 3 θ] + γ^2 (1 + ϵ) Cos[4 β - 3 θ] -
                    3 γ (1 + ϵ) Cos[2 β - θ] + 3 (γ^2 + ϵ) Cos[θ] - (-1 + γ^2) ϵ Cos[3 θ])) /
                (2 (-1 + γ^2) (1 - ϵ Cos[2 θ])^(3 / 2))) + Sin[2 * .563974] *
              (-(b (1 + ϵ) (-γ (-1 + ϵ) Sin[2 β - 3 θ] - γ^2 (-1 + ϵ) Sin[4 β - 3 θ] +
                    3 γ (-1 + ϵ) Sin[2 β - θ] + 3 (γ^2 - ϵ) Sin[θ] - (-1 + γ^2) ϵ Sin[3 θ])) /
                (2 (-1 + γ^2) (1 - ϵ Cos[2 θ])^(3 / 2))), 0 ≤ θ < 2 π}, {θ}]) +
      Cos[2 * .563974] * (-Sin[2 * .563974] * ((b (-1 + ϵ) (-γ (1 + ϵ) Cos[2 β - 3 θ] +
                  γ^2 (1 + ϵ) Cos[4 β - 3 θ] - 3 γ (1 + ϵ) Cos[2 β - θ] +
                  3 (γ^2 + ϵ) Cos[θ] - (-1 + γ^2) ϵ Cos[3 θ])) /
                (2 (-1 + γ^2) (1 - ϵ Cos[2 θ])^(3 / 2))) + Cos[2 * .563974] *
              (-(b (1 + ϵ) (-γ (-1 + ϵ) Sin[2 β - 3 θ] - γ^2 (-1 + ϵ) Sin[4 β - 3 θ] +
                    3 γ (-1 + ϵ) Sin[2 β - θ] + 3 (γ^2 - ϵ) Sin[θ] - (-1 + γ^2) ϵ Sin[3 θ])) /
                (2 (-1 + γ^2) (1 - ϵ Cos[2 θ])^(3 / 2))))) /. θ → ArgMax[
        {Cos[2 * .563974] * ((b (-1 + ϵ) (-γ (1 + ϵ) Cos[2 β - 3 θ] + γ^2 (1 + ϵ) Cos[4 β - 3 θ] -
                    3 γ (1 + ϵ) Cos[2 β - θ] + 3 (γ^2 + ϵ) Cos[θ] - (-1 + γ^2) ϵ Cos[3 θ])) /
                (2 (-1 + γ^2) (1 - ϵ Cos[2 θ])^(3 / 2))) + Sin[2 * .563974] *
              (-(b (1 + ϵ) (-γ (-1 + ϵ) Sin[2 β - 3 θ] - γ^2 (-1 + ϵ) Sin[4 β - 3 θ] +
                    3 γ (-1 + ϵ) Sin[2 β - θ] + 3 (γ^2 - ϵ) Sin[θ] - (-1 + γ^2) ϵ Sin[3 θ])) /
                (2 (-1 + γ^2) (1 - ϵ Cos[2 θ])^(3 / 2))), 0 ≤ θ < 2 π}, {θ}]}];
```

**normal(i.e non-elongated) caustic right-upper (cusp in the first quadrant)**

```
RU[θ_, β_, γ_, ϵ_, b_] :=
  Flatten[{{(b (-1 + ϵ) (-γ (1 + ϵ) Cos[2 β - 3 θ] + γ^2 (1 + ϵ) Cos[4 β - 3 θ] -
            3 γ (1 + ϵ) Cos[2 β - θ] + 3 (γ^2 + ϵ) Cos[θ] - (-1 + γ^2) ϵ Cos[3 θ])) /
        (2 (-1 + γ^2) (1 - ϵ Cos[2 θ])^(3 / 2)) /. θ → ArgMax[
         {(- (b (1 + ϵ) (-γ (-1 + ϵ) Sin[2 β - 3 θ] - γ^2 (-1 + ϵ) Sin[4 β - 3 θ] +
                  3 γ (-1 + ϵ) Sin[2 β - θ] + 3 (γ^2 - ϵ) Sin[θ] - (-1 + γ^2) ϵ Sin[3 θ])) /
             (2 (-1 + γ^2) (1 - ϵ Cos[2 θ])^(3 / 2)), 0 ≤ θ < 2 π}, {θ}]),
      (MaxValue[{{(- (b (1 + ϵ) (-γ (-1 + ϵ) Sin[2 β - 3 θ] - γ^2 (-1 + ϵ) Sin[4 β - 3 θ] +
                  3 γ (-1 + ϵ) Sin[2 β - θ] + 3 (γ^2 - ϵ) Sin[θ] - (-1 + γ^2) ϵ Sin[3 θ])) /
             (2 (-1 + γ^2) (1 - ϵ Cos[2 θ])^(3 / 2)), 0 ≤ θ < 2 π}, {θ}])}];
```

**normal(i.e non-elongated) or elongated caustic right-lower peak (cusp in the fourth quadrant)**

```
RL[θ_, β_, γ_, ϵ_, b_] :=
  {(MaxValue[{(b (-1 + ϵ) (-γ (1 + ϵ) Cos[2 β - 3 θ] + γ^2 (1 + ϵ) Cos[4 β - 3 θ] -
            3 γ (1 + ϵ) Cos[2 β - θ] + 3 (γ^2 + ϵ) Cos[θ] - (-1 + γ^2) ϵ Cos[3 θ])) /
        (2 (-1 + γ^2) (1 - ϵ Cos[2 θ])^(3 / 2)), 0 ≤ θ < 2 π}, {θ}]),
    ((- (b (1 + ϵ) (-γ (-1 + ϵ) Sin[2 β - 3 θ] - γ^2 (-1 + ϵ) Sin[4 β - 3 θ] +
              3 γ (-1 + ϵ) Sin[2 β - θ] + 3 (γ^2 - ϵ) Sin[θ] - (-1 + γ^2) ϵ Sin[3 θ])) /
         (2 (-1 + γ^2) (1 - ϵ Cos[2 θ])^(3 / 2))) /. θ → ArgMax[
        {(b (-1 + ϵ) (-γ (1 + ϵ) Cos[2 β - 3 θ] + γ^2 (1 + ϵ) Cos[4 β - 3 θ] -
              3 γ (1 + ϵ) Cos[2 β - θ] + 3 (γ^2 + ϵ) Cos[θ] - (-1 + γ^2) ϵ Cos[3 θ])) /
          (2 (-1 + γ^2) (1 - ϵ Cos[2 θ])^(3 / 2)), 0 ≤ θ < 2 π}, {θ}])};
```

## arrival time for central source position

```
ArrivalT[θ_, β_, γ_, ϵ_, b_] := (b^2 (1 - ϵ Cos[2 θ])) / (-2 + 2 γ Cos[2 (β - θ)]);
```

## Image radial position for a given angle

```
rr[θ_, β_, γ_, ϵ_, b_] := b * Sqrt[1 - ϵ Cos[2 θ]] / (1 - γ Cos[2 (-β + θ)]);
```

```
--------------------------------------------------------------------------------
                                          ------------------------
```

```
Off[Part::partw];
Off[Infinity::indet];
Off[ListPlot::nonopt]; Off[Part::partw];
Off[Show::gcomb];
Off[Part::partd];
```

## Image and caustic diagram

```
Manipulate[AA =
  {θ /. Quiet[Solve[ϵ Sin[2 θ] == γ Sin[2 (θ - β)] * (1 - ϵ Cos[2 θ]) / (1 - γ Cos[2 (θ - β)]),
      θ, Reals]] /. C[1] → 1};
 rr[θ_] := b * Sqrt[1 - ϵ Cos[2 θ]] / (1 - γ Cos[2 (-β + θ)]);
 Show[ListPlot[{Flatten[{rr[AA[[All, 1]]] * Cos[AA[[All, 1]]],
      rr[AA[[All, 1]]] * Sin[AA[[All, 1]]]}]}, AxesOrigin → {0, 0}, AspectRatio → 1,
   PlotRange → {{-30, 30}, {-30, 30}}, PlotStyle -> PointSize[.02]],
  ListPlot[{Flatten[{rr[AA[[All, 2]]] * Cos[AA[[All, 2]]], rr[AA[[All, 2]]] *
       Sin[AA[[All, 2]]]}]}, PlotStyle → {Red, PointSize[.02]}], ParametricPlot[
   {(b (-1 + ϵ) (-γ (1 + ϵ) Cos[2 β - 3 θ] + γ^2 (1 + ϵ) Cos[4 β - 3 θ] - 3 γ (1 + ϵ) Cos[2 β - θ] +
         3 (γ^2 + ϵ) Cos[θ] - (-1 + γ^2) ϵ Cos[3 θ])) / (2 (-1 + γ^2) (1 - ϵ Cos[2 θ])^(3/2)),
    (b (γ (-1 + ϵ^2) (-1 + γ Cos[2 (β - θ)]) Sin[2 β - θ] + (1 + ϵ) (-γ^2 + ϵ - γ (-1 + ϵ) Cos[
          2 (β - θ)] + (-1 + γ^2) ϵ Cos[2 θ]) Sin[θ])) / ((-1 + γ^2) (1 - ϵ Cos[2 θ])^(3/2))},
   {θ, 0, 2 π}]], {β, 0.0, π / 2}, {γ, 0, .999}, {ϵ, 0.0, .999}, {b, 1, 20}]
```

# Comparison ( $\theta_{23}$ vs diagonal angle, for both elongated and standard caustic)

```
Quiet[Manipulate[{If[
    Abs[Quiet[ArcTan[Chop[RL[θ, β, γ, ϵ, b]][[1]], Chop[RL[θ, β, γ, ϵ, b]][[2, 1]]]] -
      Quiet[ArcTan[Chop[RU[θ, β, γ, ϵ, b]][[1]], Chop[RU[θ, β, γ, ϵ, b]][[2]]]]] == π,
    {Abs[Quiet[ArcTan[Chop[RL[θ, β, γ, ϵ, b]][[1]], Chop[RL[θ, β, γ, ϵ, b]][[2]]]] -
       Quiet[ArcTan[Chop[RUE[θ, β, γ, ϵ, b]][[1]],
         Chop[RUE[θ, β, γ, ϵ, b]][[2]]]]] * 180 / π,
     Quiet[Sqrt[Chop[RL[θ, β, γ, ϵ, b]][[1]]^2 + Chop[RL[θ, β, γ, ϵ, b]][[2]]^2]] /
      Quiet[Sqrt[Chop[RUE[θ, β, γ, ϵ, b]][[1]]^2 + Chop[RUE[θ, β, γ, ϵ, b]][[2]]^2]]},
    {If[Ang = Abs[Quiet[ArcTan[Chop[RL[θ, β, γ, ϵ, b]][[1]],
          Chop[RL[θ, β, γ, ϵ, b]][[2, 1]]]] - Quiet[ArcTan[
          Chop[RU[θ, β, γ, ϵ, b]][[1]], Chop[RU[θ, β, γ, ϵ, b]][[2]]]]] * 180 / π;
      Ang < 90, 180 - Ang, Ang], If[DiagRatio = Quiet[
        Sqrt[Chop[RU[θ, β, γ, ϵ, b]][[1]]^2 + Chop[RU[θ, β, γ, ϵ, b]][[2]]^2]] /
       Quiet[Sqrt[Chop[RL[θ, β, γ, ϵ, b]][[1]]^2 + Chop[RL[θ, β, γ, ϵ, b]][[2]]^2]];
      DiagRatio[[1]] < 1, (DiagRatio[[1]])^-1, DiagRatio[[1]]]},
   AA = {θ /. Quiet[Solve[ϵ Sin[2 θ] == γ Sin[2 (θ - β)] *
         (1 - ϵ Cos[2 θ]) / (1 - γ Cos[2 (θ - β)]), θ, Reals]] /. C[1] → 1};
   SecondA = AA[[All, 1]];
   FirstA = AA[[All, 2]];
   If[ArrivalT[AA[[All, 2]], β, γ, ϵ, b][[1]] >
     ArrivalT[AA[[All, 1]][[1]], β, γ, ϵ, b], SecondA = AA[[All, 2]];
    FirstA = AA[[All, 1]];];
   Flatten[{180 - Abs[(AA[[All, 2]] - AA[[All, 1]])] * 180 / π,
     rr[FirstA[[1]], β, γ, ϵ, b] / rr[SecondA[[1]], β, γ, ϵ, b]}]},
  {β, 0.0, π / 2}, {γ, 0, .2}, {ϵ, 0, .22}, {b, 1, 10}]]

Off[NMinimize::nnum]; Off[ReplaceAll::reps]; Off[Part::partw];
```

# Calculating 3D plot ( entire plot, edges,...)

assigning variables ( int1 counts # of source positions that images are calculated for, int is the interval along the x or y axis when calculating source position along caustic diagonal, ratio is the ratio of ymax to xmax along caustic diagonal)

```
β = .5; γ = 0.06; ϵ = 0.034944; b = 7; (*ratio=DP[[2]]/DP[[1]];
ys=xs*ratio;
xs0=0;
xsf=(DP[[1]]);
int=1.1;*)(*int1=IntegerPart[xsf/int]+1;*)int1 = 70 000;
```

calculating cusp peak to find end point of diagonal

```
RL[θ, β, γ, ϵ, b];
```

```
RU[θ, β, γ, ϵ, b];
```

```
RUE[θ, β, γ, ϵ, b];
```

```
DP = Flatten[RL[θ, .5, .06, .034944, 7]];
```

Assigning arrays

```
arrival = Array[arrivalT, {int1, 4}]; AngArrPos = Array[angArrPos, {int1, 4, 6}];
data = Array[data1, {int1, 5}]; Angles = Array[angles, {int1, 4}];
arrivImage = Array[imageID, {int1, 4, 2}];
positions = Array[posRan, {int1}]; Off[NSolve::ratnz]
```

## Calculating image positions

### calculating image positions for source positions along the diamond caustic's diagonals

```
(*positions=
  {x,y}/.Table[NSolve[{x-xs+b x (-1+ϵ)/Sqrt[-x^2 (-1+ϵ)+y^2 (1+ϵ)]-x γ Cos[2 β]-y γ Sin[2 β]==0,
      y-ys-b y (1+ϵ)/Sqrt[-x^2 (-1+ϵ)+y^2 (1+ϵ)]+y γ Cos[2 β]-x γ Sin[2 β]==0},
    {x,y},Reals],{xs,0,xsf,int}];*)
```

### calculating image positions for random source positions

```
RanSource = Table[{RandomReal[{-DP[[1]], DP[[1]]}],
    RandomReal[{-DP[[2]], DP[[2]]}]}, {i, 1, int1}];
```

main position calculation for random source

```
positions1[xs_, ys_] :=
 {x, y} /. NSolve[{x - xs + b x (-1 + ϵ)/Sqrt[-x^2 (-1 + ϵ) + y^2 (1 + ϵ)] - x γ Cos[2 β] - y γ Sin[2 β] == 0,
    y - ys - b y (1 + ϵ)/Sqrt[-x^2 (-1 + ϵ) + y^2 (1 + ϵ)] + y γ Cos[2 β] - x γ Sin[2 β] == 0}, {x, y}, Reals]
```

```
positions = ParallelMap[Quiet[positions1[#[[1]], #[[2]]]] &, RanSource];
(*//AbsoluteTiming*)
```

```
positions1 =
  Select[MapIndexed[{#, Length[#1], First[#2]} &, positions], #[[2]] == 4 &][[All, 1]];
```

## Choosing only 4-images system

```
Select[MapIndexed[{#, Length[#1], First[#2]} &, positions], #[[2]] == 4 &][[All, 3]];
RanSource1 = RanSource[[%]];
```

```
RanSource = RanSource1; positions = positions1; int1 = First[Dimensions[positions]];
```

```
Export[NotebookDirectory[] <> "positions.dat", positions];
```

```
(*Do[posRan[i]={x,y}/.NSolve[{x-xs+(b x (-1+ϵ))/Sqrt[-x^2 (-1+ϵ)+y^2 (1+ϵ)]-x γ Cos[2 β]-y γ Sin[2 β]==0,
      y-ys-(b y (1+ϵ))/Sqrt[-x^2 (-1+ϵ)+y^2 (1+ϵ)]+y γ Cos[2 β]-x γ Sin[2 β]==0}/.
    {β->.9,γ->0.4532,ϵ->0.2079,b->40,xs→RanSource[[i,1]],ys→RanSource[[i,2]]},
   {x,y},Reals],{i,1,300}]*)
```

```
arrival = Array[arrivalT, {int1, 4}]; AngArrPos = Array[angArrPos, {int1, 4, 6}];
data = Array[data1, {int1, 5}]; Angles = Array[angles, {int1, 4}];
arrivImage = Array[imageID, {int1, 4, 2}]; Off[NSolve::ratnz]
```

## calculating angles

```
For[i = 1, i ≤ int1, i++, For[l = 1, l ≤ 4, l++,
  If[positions[[i, All]][[l, 1]] > 0 && positions[[i, All]][[l, 2]] > 0, angles[i, l] =
    ArcTan[positions[[i, All]][[l, 2]] / positions[[i, All]][[l, 1]]] * 180 / π,
   If[positions[[i, All]][[l, 1]] < 0, angles[i, l] =
     ArcTan[positions[[i, All]][[l, 2]] / positions[[i, All]][[l, 1]]] * 180 / π + 180,
    angles[i, l] = ArcTan[positions[[i, All]][[l, 2]] / positions[[i, All]][[l, 1]]] *
       180 / π + 360]]]]
```

```
arrival = Array[arrivalT, {int1, 4}]; AngArrPos = Array[angArrPos, {int1, 4, 6}];
data = Array[data1, {int1, 5}]; Angles = Array[angles, {int1, 4}];
arrivImage = Array[imageID, {int1, 4, 2}]; Off[NSolve::ratnz]
```

```
Export[NotebookDirectory[] <> "Angles.dat", Angles];
```

## calculating arrival times

## Arrival time for random source

```
For[k = 1, k ≤ int1, k++, For[j = 1, j ≤ 4, j++,
  arrivalT[k, j] = (1/2 ((x - xs)^2 + (y - ys)^2) - b Sqrt[-x^2 (-1 + ϵ) + y^2 (1 + ϵ)] -
      1/2 (x^2 - y^2) γ Cos[2 β] - x y γ Sin[2 β]) /.
    {x → positions[[k, All]][[j, 1]], y -> positions[[k, All]][[j, 2]]} /.
   {xs → RanSource[[k, 1]], ys → RanSource[[k, 2]]}]]
```

## Arrival time for source along the caustic diagonal

```
(*For[k=1,k≤int1,k++,
 For[j=1,j≤ 4,j++,arrivalT[k,j]=(1/2 ((x-xs)^2+(y-ys)^2)-b Sqrt[-x^2 (-1+ϵ)+y^2 (1+ϵ)] -
        1/2 (x^2-y^2) γ Cos[2 β]-x y γ Sin[2 β])/.{x→positions[[k,All]][[j,1]],
      y->positions[[k,All]][[j,2]]}/.{xs→int*(k-1)}]]*)

arrival = Array[arrivalT, {int1, 4}];

Export[NotebookDirectory[] <> "arrival.dat", arrival];
```

## merging angles list with arrival time list

```
Do[Do[imageID[i, j, 1] = angles[i, j];
  imageID[i, j, 2] = arrivalT[i, j], {j, 1, 4}], {i, 1, int1}]

arrivImage = Array[imageID, {int1, 4, 2}];

Export[NotebookDirectory[] <> "arrivImage.dat", arrivImage];
```

merging angles list with arrival time , image positions and source positions lists

```
(*Do[Do[angArrPos[i,j,1]=angles[i,j];
  angArrPos[i,j,2]=arrivalT[i,j];
  angArrPos[i,j,3]=positions[[i,All]][[j,1]];
  angArrPos[i,j,4]=positions[[i,All]][[j,2]];
  angArrPos[i,j,5]=-.1*(i-1)/0.632499;
  angArrPos[i,j,6]=.1*(i-1),{j,1,4}],{i,1,201}]*)
```

## sorting angles merged with arrival time based on arrival time

```
sortedAng = Table[Sort[arrivImage[[i]], #1[[2]] < #2[[2]] &], {i, 1, int1}];

Export[NotebookDirectory[] <> "sortedAng.dat", sortedAng];
```

sorting angles merged with arrival time , image position and source position based on arrival time

```
(*sortedAng0=Table[Sort[AngArrPos[[i]],#1[[2]]<#2[[2]]&],{i,1,201}];*)
```

## relative angles for given image positions

## Relative angles for given image position where the source is along the caustic diagonal

```
(*For[i=1,i≤int1,i++,data1[i,1]=int*(i-1);
 data1[i,2]=int*(i-1)*ratio;
 data1[i,3]=Abs[sortedAng[[i,All]][[1,1]]-sortedAng[[i,All]][[2,1]]];
 data1[i,4]=Abs[sortedAng[[i,All]][[3,1]]-sortedAng[[i,All]][[4,1]]];
 data1[i,5]=Abs[sortedAng[[i,All]][[2,1]]-sortedAng[[i,All]][[3,1]]]]*)
```

## Relative angles for given image position for random source positions

```
For[i = 1, i ≤ int1, i++, data1[i, 1] = RanSource[[i, 1]];
 data1[i, 2] = RanSource[[i, 2]];
 data1[i, 3] = Abs[sortedAng[[i, All]][[1, 1]] - sortedAng[[i, All]][[2, 1]]];
 data1[i, 4] = Abs[sortedAng[[i, All]][[3, 1]] - sortedAng[[i, All]][[4, 1]]];
 data1[i, 5] = Abs[sortedAng[[i, All]][[2, 1]] - sortedAng[[i, All]][[3, 1]]]]
```

## relative angles defined to be less than 180 degrees

```
Do[Do[If[data1[i, j] > 180, data1[i, j] = 360 - data1[i, j]], {j, 3, 5}], {i, 0, int1}]
```

```
data = Array[data1, {int1, 5}];
```

```
Export[NotebookDirectory[] <> "data3D.dat", data];
```